

# DISSERTATION

## ELECTROCHEMICAL AND SPECTROSCOPIC IN SITU TECHNIQUES FOR THE INVESTIGATION OF THE PHOSPHATING OF ZINC COATED STEEL

ausgeführt zum Zwecke der Erlangung des akademischen Grades  
eines Doktors der technischen Wissenschaften unter der Leitung von

**Univ. Prof. Dr. Christoph Fabjan**

Institut für Chemische Technologien und Analytik (E 164)  
Abteilung Elektrochemie

eingereicht an der Technischen Universität Wien  
Fakultät für Technische Naturwissenschaften und Informatik


von

**Dipl.-Ing. Alexander Tomandl**

3354 Wolfsbach 108

Matrikelnummer: 9126512

Wien im Mai 2003



## KURZFASSUNG

In dieser Arbeit wurden spektroskopische und elektrochemische Methoden zur Untersuchung von Oberflächenbehandlungen in der Stahlindustrie entwickelt und angewandt. **ICP-Atomemissionsspektroskopie (ICP-AES)**, Ramanspektroskopie und die Quarzmikrowaage (QMW) kamen zum Einsatz, um die Reaktionskinetik der Phosphatierung als auch die Eigenschaften von Phosphatschichten zu untersuchen. Die **Phosphatierung** von verzinktem Stahl führt zur Ausbildung einer kristallinen Schicht aus Zinkphosphaten auf der Metalloberfläche und wird als Vorbehandlung zur Steigerung der Haftung von Lackschichten eingesetzt.

Um die im industriellen Einsatz notwendigen hohen Reaktionsgeschwindigkeiten zu erreichen, werden den Phosphatierbädern Oxidationsmittel als Beschleuniger zugesetzt, die durch ihre Reduktion eine Ersatzreaktion zur Wasserstoffbildung anbieten. Dadurch kommt es zu einer deutlichen Verringerung der gebildeten Gasblasen, welche ansonsten die Metalloberfläche blockieren. Als besonders leistungsfähige Beschleuniger stellten sich Wasserstoffperoxid und Nitrat heraus. Es konnte durch eine Kombination von ICP-AES mit der Quarzmikrowaage und Potentialtransienten gezeigt werden, dass die beschleunigende Wirkung vor allem in der Steigerung der Zinkauflösung im Phosphatierbad liegt, welche wiederum zu einer schnelleren Ausbildung der Phosphatschicht führt.

Für den Korrosionsschutz von lackiertem, verzinktem Stahl ist die Stabilität der Phosphatschicht gegenüber alkalischen Medien ausschlaggebend. Zur Erhöhung der Alkalistabilität werden modernen Phosphatierbädern Mangan und Nickel zugesetzt. Die Anwesenheit dieser Elemente verringert die Auflösungsrate in 0.1 M Natronlauge proportional zu ihrer Konzentration in der Schicht. Mit Hilfe von ICP-AES konnte die Auflösung der Elemente Zn, P, Mn und Ni quantitativ verfolgt werden. In situ Ramanspektroskopie zeigte die Bildung von Mn-hydroxid während des alkalischen Angriffs, wodurch die weitere Auflösung der Phosphatschicht deutlich reduziert wird. Der alkalische Angriff kann aufgrund der Ergebnisse als Ionenaustausch zwischen  $\text{PO}_4^{3-}$  und **OH<sup>-</sup>-Ionen** mit der Bildung eines Mischoxides aus Zn und Mn gesehen werden. Messungen mit der Quarzmikrowaage bestätigten das aus ICP-AES und Ramanspektroskopie abgeleitete Modell des Reaktionsmechanismus.

## ABSTRACT

In this work spectroscopic and electrochemical techniques were developed for the investigation of surface treatments used in steel industry. **ICP-atomic** emission spectroscopy (**ICP-AES**), Raman spectroscopy and the Quartz crystal **microbalance (QCM)** were applied to the investigation of the kinetics of phosphating as well as the properties of phosphate layers. Phosphating of zinc coated steel leads to the formation of a crystalline layer consisting of zinc phosphate and is employed to enhance paint adhesion and corrosion protection.

For the high reaction rates necessary in industrial production lines, oxidation agents are added to the phosphating bathes to accelerate the reaction. The oxidation agents provide an additional reduction reaction beside the hydrogen formation and therefore decrease the number of gas bubbles, which would block the zinc surface and reduce the rate of phosphating. With addition of  $\text{H}_2\text{O}_2$  or nitrates the rate of layer formation is distinctly increased. In a combined experiment of ICP-AES with QCM and potential transients, it was shown that the presence of these accelerators in the phosphating bath increases the rate of zinc dissolution and hence leads to a faster formation of the phosphate layer.

In under paint corrosion of painted, zinc coated steel phosphate layers are exposed to a highly alkaline environment. The stability of a phosphate layer against alkaline attack is therefore essential for its performance in corrosion protection. To enhance the alkaline stability Mn and Ni are added to modern phosphating bathes. The incorporation of these elements reduces the dissolution rate in 0.1 M NaOH proportional to their concentration in the phosphate layer. The dissolution of Zn, P, Mn and Ni was determined quantitatively with ICP-AES. Raman spectroscopy showed the formation of a Mn-hydroxide layer during alkaline attack, which protects the phosphate layer and reduces further dissolution. On basis of these results the reaction of phosphate layers with alkaline solution can be proposed as an ion-exchange of  $\text{PO}_4^{3-}$  and  $\text{OH}^-$  resulting in a mixed hydroxide consisting of Zn and Mn. The model of the reaction mechanism was confirmed by additional QCM experiments.

## TABLE OF CONTENTS

1	INTRODUCTION	1
2	PHOSPHATE CONVERSION COATINGS	2
2.1	<b>Definition and Application</b>	2
2.2	<b>Historical development [1]</b>	3
2.3	<b>Important steps of phosphating</b>	5
2.3.1	Degreasing	5
2.3.2	Activation	6
2.3.3	Phosphating	7
2.4	<b>Nature of the phosphate layer</b>	12
2.4.1	Crystal phases in phosphate layers	13
2.4.2	Influence of heavy metal ions	14
2.5	<b>Chemical stability of phosphate layer</b>	15
2.6	<b>Corrosion mechanism</b>	16
3	THEORETICAL BACKGROUND OF THE METHODS	20
3.1	<b>Raman spectroscopy</b>	20
3.1.1	Basics of vibrational spectroscopy	20
3.1.2	Quantum mechanical model	22
3.2	<b>Quartz Crystal Microbalance</b>	24
3.2.1	The piezoelectric effect	24
3.2.2	Quartz Crystals for QCM	24
3.2.3	Mass-frequency relationship	26
3.2.4	Deviations from the Sauerbrey equation	27
3.3	<b>ICP Atomic Emission Spectroscopy</b>	29
3.3.1	Atomic spectra	29
3.3.2	Excitation	30
3.4	<b>The methods in literature</b>	31
4	EXPERIMENTAL SECTION	33
4.1	<b>Metal substrates</b>	33

<b>4.2</b>	<b>Synthesis of phosphate layers</b>	<b>33</b>
4.2.1	Post treatment of phosphate layers	35
<b>4.3</b>	<b>Analysis and SEM micrographs</b>	<b>35</b>
<b>4.4</b>	<b>Painting and Corrosion tests</b>	<b>36</b>
<b>4.5</b>	<b>Electrochemical Experiments</b>	<b>36</b>
<b>4.6</b>	<b>Raman Spectroscopy</b>	<b>37</b>
<b>4.7</b>	<b>ICP-AES</b>	<b>40</b>
4.7.1	Spectrometer details	40
4.7.2	Flow Cell	42
4.7.3	Relationship between rate and intensity	43
4.7.4	Experimental procedure	44
<b>4.8</b>	<b>QCM</b>	<b>45</b>
<b>4.9</b>	<b>Calibration of residence time in ICP experiments</b>	<b>48</b>
<b>5</b>	<b>ALKALINE STABILITY OF PHOSPHATE LAYERS</b>	<b>49</b>
<b>5.1</b>	<b>Background</b>	<b>49</b>
<b>5.2</b>	<b>Analysis and morphology of the layers</b>	<b>49</b>
<b>5.3</b>	<b>Corrosion testings</b>	<b>54</b>
5.3.1	Salt Spray Test	54
5.3.2	Scab Corrosion Test	58
<b>5.4</b>	<b>ICP-AES</b>	<b>60</b>
5.4.1	General Features of the Leaching Transients	60
5.4.2	Kinetics of Alkaline Leaching of Phosphate Coatings on Zinc	61
5.4.3	Composition of the Residual Layers	64
5.4.4	Alkaline Leaching of Phosphate Layers on Cold Rolled Steel	67
5.4.5	Effect of Post treatment	70
5.4.6	Discussion of ICP-Results	71
<b>5.5</b>	<b>Raman spectroscopy</b>	<b>75</b>
5.5.1	General Features of the Raman Spectra	75
5.5.2	Kinetics of Alkaline Leaching of Phosphate Coatings	78
5.5.3	Some Aspects of Quantification	79
5.5.4	Identification of reaction products	82
5.5.5	Discussion	84
<b>5.6</b>	<b>QCM Study of Alkaline stability (QCM combined with ICP)</b>	<b>88</b>
5.6.1	Experimental	88
5.6.2	Results	88
5.6.3	Discussion - Quantitative Relationships	90
<b>5.7</b>	<b>Conclusions</b>	<b>93</b>

6	KINETICS OF PHOSPHATING	94
6.1	Background	94
6.2	Electrochemical Experiments	94
6.3	Kinetics of Phosphating with Quartz Crystal Microbalance	98
6.3.1	Experimental	98
6.3.2	Results and Discussion	99
6.4	Anodic Dissolution of Zinc in the Presence of Accelerators (QCM-ICP)	105
6.4.1	Experimental	105
6.4.2	Results and Discussion	106
6.5	Conclusion	114
7	SUMMARY	115
7.1	Alkaline stability	115
7.2	Kinetics of phosphating reaction	116
7.3	Outlook	118
8	LITERATURE	119

# 1 INTRODUCTION

Corrosion protection of modern steel often includes the application of coatings in metallic, inorganic and organic state. The subsequent application of different coatings is especially efficient in protection. Usual stages for ferrous metals are electroplating with zinc (metallic), phosphating (inorganic) and painting with two to four layers (organic).

The thin inorganic layers between metal substrate and paint, often called conversion layers, are applied to facilitate further coating and painting processes by improvement of formability and paint adhesion. Phosphate conversion is widely used on steel and zinc coated steel and is the most frequently applied surface treatment in the automotive industry. This process is used in industry for nearly 100 years and was subject to various improvements since its invention, leading to modern, easily applicable systems with fast reaction rates.

The major research effort in this area has been in characterising the corrosion and adhesion properties of the final product as a cursory glance at the technical literature demonstrates. Less interest was put on detailed mechanistic and kinetic studies, which are to a large extent limited by the available experimental technology. However, further improving of the surface treatment process and better understanding of the reaction kinetics and the protection mechanism is still of major interest in the steel industry.

In this work new spectroscopic and electrochemical methods for in-situ observation of the **surface** reactions will be developed. In particular a combination of three major techniques will allow to observe the nature of the surface films (*Raman spectroscopy*), to follow elemental concentration changes in applied electrolytes (*Atomic emission spectroscopy*) and to measure the changes in mass associated with substrate dissolution and film precipitation (*Quartz crystal microbalance*). Specific emphasis will be laid on the stability of phosphate layers against attack of alkaline solution as this is important for corrosion protection and on the role of accelerators in phosphating bathes on the anodic dissolution of the substrate metal.

By use of this techniques unprecedented information on the kinetics of the surface treatment and its role in corrosion protection should be obtained. Beyond that, the results should allow to propose simple models of the reaction mechanism during phosphating and of the modifications by corrosive attack.

## 2 PHOSPHATE CONVERSION COATINGS

### 2.1 DEFINITION AND APPLICATION

Conversion coatings are thin inorganic layers formed on metal surfaces by contact with liquid solutions of specific chemical composition. In the case of phosphating the process involves the treatment of the substrate metal with an acidic solution of primary metal phosphates (usually  $Zn_2(H_2PO_4)_2$ ) and leads to the formation of insoluble tertiary metal phosphates on the metal surface [1, 2, 3].

The phosphating process discussed in this work utilises aqueous solutions, which contain all the main constituents required for coating formation, i.e. the phosphate anion and at least some of the metal cations. The layers formed by this process usually consist of discrete crystals rather than a continuous film with coating weights in the range of 1 to 4  $g/m^2$ . This process has to be distinguished from the so called non-coating phosphating processes [1, 4], where usually alkali metal phosphate solutions at neutral or basic pH-values are applied. Amorphous, very thin layers are formed on the surfaces with coating weights around 0.1  $g/m^2$  up to 0.5  $g/m^2$ .

Phosphating is used in the metalworking industry world-wide to treat substrates like steel, galvanised steel, aluminium and magnesium [5]. Its major use today is the pretreatment before cathodic painting in the automotive industry. Car bodies are assembled prior to the treatment and undergo phosphating either in spraying or dipping or in a spray/dip combination [6]. The following painting process is greatly improved by the crystalline phosphate layer present on the surface.

Another application of phosphating is to facilitate drawing and forming of metal parts. The phosphate crystals may act as a lubricant themselves by breaking easily under pressure [1] or their excellent oil retaining qualities are used to lower friction during forming. The phosphate layer on the metal is thought to inhibit rupture of the oil film [1]. This type of application is the major use of "prephosphated" galvanised steel today, which is quite common in the automotive industry. Phosphating is applied directly in the galvanising lines of the steel mills by a spray process. Due to the degreasing of the car bodies after forming and drawing of the metal, the phosphate layer is removed from the



surface and another phosphating process has to be done prior to the subsequent painting process.

## 2.2 HISTORICAL DEVELOPMENT [1]

The industrial use of phosphating dates back to the year 1864, when de Bussy obtained a British patent for the treatment of hot iron with a mixture of coal dust and calcium dihydrogen phosphate. Ross proposed the treatment of steel based on immersion of the heated iron in boiling phosphoric acid to improve corrosion resistance. A number of similar patents appeared in the following years, but the process was largely ignored until a patent of T.W. Coslett came up in 1906. The process, which became known as Coslettising consisted of the treatment of steel in phosphoric acid near the boiling point for corrosion protection. To minimise the effect of the massive reaction taking place, Coslett added iron filings to the solutions. To enhance the rather poor corrosion resistance, a final rinse in chromic acid was introduced.

The process was greatly improved, when Coslett discovered the benefits of using zinc dihydrogen phosphate as a an addition to phosphoric acid. The use of phosphoric acid salts like manganese dihydrogen phosphate was claimed a little bit later by Richards in a British patent of 1911. Based on these works, Clark and Wyman Parker developed a phosphating process with zinc and manganese as additives to phosphoric acid. The process became known as "Parkerising" and reached large industrial use.

In the following years better controllable phosphating processes were developed. Around 1930, copper and nickel additives were introduced to speed up the reaction and permit the use of lower temperatures during treatment. The use of nitrates as accelerators also dates back to this period.

The introduction of an activation step by Jernstedt by applying an aqueous solution of **Ti-colloids** dramatically increased the rate of the phosphating reaction and the quality of the layers [7]. Up to now this type of activation is the most frequently used and greatly contributed to the reduction of treatment time from hours in the early beginnings to well below 10 s on modern spray phosphating lines.

Another fundamental change was the introduction of so called "low zinc phosphating" in the seventies [8]. The zinc concentration necessary in the bathes could be reduced down to 0.7-1.5 g/l by simultaneous increasing of the amount of phosphate

anions present in the solution. Layers with an improved barrier effect against corrosion were obtained.

Various efforts were done to further enhance corrosion resistance, leading to the modern trication phosphating process. The bathes, developed in the mid eighties, contain Mn and Ni cations beside Zn and are the most common systems nowadays [9] (trication refers to the three metal cations present in the solution).

Today environmental issues represent the major driving force for further development of phosphating technology. This includes the elimination of Ni and/or nitrite in the bathes. Nitrite is still a common accelerator in the phosphating process for the automotive industry. For the substitution of nickel, copper additions were introduced, which can be added to the phosphating solutions at much lower concentrations than nickel and therefore cause less problems in the waste water treatment. Phosphating processes free of Ni and nitrite were developed in the 90's [10], but did not fully meet the customer requirements and became only rarely applied.

To eliminate nitrite, products with new accelerating agents like hydroxylamine [3] or nitrobenzene sulfonic acid are available on the market. The major challenge for new products is the easy application on existing phosphating lines whether in automotive industry or on galvanising lines without large modifications.

The chromate post rinse, which usually followed phosphating was and will be abandoned by many users due to the suspected carcinogenic properties of Cr(VI). New post treatments based on Zr and Ti with possible polymer additions reached technological importance and show protective qualities comparable to the chromate rinse [11].

Another driving force for technological development is the necessity to treat different metals with the same phosphating bath. In the automotive industry **nowadays**, steel and/or galvanised steel are often assembled together with light metals and alloys such as magnesium and aluminium. The phosphating process therefore must work equally well on all these different surfaces.

## 2.3 IMPORTANT STEPS OF PHOSPHATING

### 2.3.1 DEGREASING

Degreasing of the metal prior to the phosphating treatment is a crucial step and critical for the optimum performance of the **phosphated** and finished painted metal [12, 13]. The effect of the activation step preceding the phosphating strongly depends on adequate cleanness and **wettability** of the metal surface.

Degreasing is not carried out on zinc galvanising lines equipped with an in-line phosphating facility. In an electrogalvanising line phosphating is applied right after the final water rinse following the electrolytic deposition section. Similarly, hot dip galvanised steel can be activated and phosphated without further **pre-treatment** right after solidification of the zinc layer and an optional skin pass section [14]. In contrast, on separate coil coating lines or in the painting mills of car manufacturers the coils resp. the car bodies may arrive with an undefined surface state, partly or fully oiled for corrosion protection or lubrication and covered with metal oxides.

A clean surface covered fully or partly with oxides is not harmful to the phosphating process [15], whereas remainders of oil have a strong detrimental effect for the whole post-treatment including phosphating and painting resulting in an insufficient paint adhesion and corrosion resistance in the worst case [16].

The primary function of degreasing is, as the name implies, the removal of oil and grease. It is well known, that degreasing has also a great effect on the nature of the metal surface, removing oxides and/or oxidising the base metal. Degreasing is typically performed using an alkaline solution at elevated temperatures. The major ingredient, the hydroxide ion, attacks and dissolves oil and grease by a saponification reaction. Depending on the **pH-value** of the cleaner, the metal surface is additionally attacked and pickled to some extent. This is especially true for zinc and aluminium **surfaces**. For steel this chemical effect is less evident.

Industrial cleaners are significantly more complex than a simple alkaline solution. Surfactants for good wettability, complexing agents to stabilise the metal ions, phosphates for dispersing insoluble particles and reducing water hardness, carbonates as alkaline reserve are typical ingredients of an industrial cleaner. The success of the cleaning step is

crucial for all further treatment steps and cannot be overemphasised in its importance for the performance of the whole **system**.

### 2.3.2 ACTIVATION

Activation is understood as the intended increase of the number of crystal nuclei on the surface of the treated metal. A higher number of crystals decreases the average size of the single crystals and the coating weight and leads to a denser phosphate layer with fewer pores [1].

During the activation step the surface is exposed to a slightly alkaline solution of **Ti-colloids**, which were first discovered by Jernstedt [7] as an activating agent for phosphating. The colloidal solutions are applied at ambient temperature by spraying or dipping. Typical size distribution of the particles is 70 % of the population between 60 and **130 nm**. The effect of activation is strongly influenced by the production procedure of the colloids. Usually a reaction between a **Ti-component** like **alpha-Ti-phosphate** and a phosphate component is started in solution or as a solid phase reaction of the powders.

The mechanism of activation was elucidated in the work of **Tegehall** [17, 18, 19]. According to this work the colloidal particles are physisorbed on the metal surface during the application of the dispersion. The adsorbed particles can easily be rinsed from the surface by water, which also eliminates the activating effect [20]. However, in the first contact with the phosphating solution an ion-exchange reaction between the sodium-ions of the adsorbed activation particles and the divalent cations of the phosphating bath (mainly zinc) takes place and establishes a chemical bonding of the particles to the surface, which now can act as nucleation centres for the formation of zinc phosphate crystals. Simple rinsing of an activated metal surface with a solution of divalent cations like Zn, **Mn**, Mg or Ni causes an ion exchange with the Na-ions. The activating effect after such a rinse is remained, in contrast to a pure water rinse.

Only little certain knowledge is available in literature about the exact physical and chemical nature of the colloids, because the direct measurement and observation of the particles in adsorbed state has proven difficult. The weak binding on the metal surface renders many surface analytical methods unsuitable. Nevertheless, the particles have been detected with certain techniques as ion microprobe analysis [21], AFM [20, 22] and **ToF-SIMS** [22]. The results of these works lead to the conclusion, that the adsorbed

particles are plate-shaped and offer a **crystallographic** plane for further epitaxial growth of the phosphate crystals.

Several products based on **Ti-colloids** for industrial use are available on the market as powders or in liquid form. Industrial phosphating nowadays is totally dependent on the activation step to deposit a beneficial zinc phosphate layer. It is preferable applied as separate stage immediately before phosphating, although combined cleaning and activation sections are also in use.

Due to their colloidal character, the dispersions are not stable and are prone to ageing even when they are not in use. The dissolved particles tend to coagulate, a reaction, which is very sensitive to the **pH-value**, temperature, water hardness and to the agitation of the solution [23]. Coagulation lowers the frequency of nucleation and thus the rate of film growth.

### 2.3.3 PHOSPHATING

#### **2.3.3.1 Overview of the mechanism**

The reaction steps of phosphating were widely studied and are well understood. Since the pioneering work of Machu [24, 25] phosphating is known as a mixed potential process with an anodic pickling reaction of the metal and a reduction of hydrogen or other oxidising agents. Accordingly the initial step of phosphating is the dissolution of the metal in the acidic bath, which increases the pH-value near the metal surface and causes the equilibrium of the phosphate solution to shift from dihydrogen phosphate anion to  $\text{PO}_4^{3-}$  -ions. By reaching a certain concentration depending on the solubility product of zinc phosphate ( $\text{p}K_L = 35.6$  [26, 27]) crystals will start to precipitate on the surface. Nucleation and crystal growth continue till the reaction stops by self-inhibition of the metal surface by the protecting phosphate layer.

### 2.3.3.2 Pickling of the metal surface

The active dissolution of the substrate metal is an essential step for phosphating. The reactivity of the metal surface plays an important role in the whole process. (Eq. 2-1). Zinc and steel are readily attacked by the phosphoric acid and are fairly easy to treat. Aluminium and steel coated with zinc by hot dip galvanising exhibit a thin oxide layer, which passivates the surface and renders metal dissolution more difficult or nearly impossible when using a pure phosphoric acid bath with zinc. For the treatment of these metals fluoride is added to the phosphating bathes in the form of HF, NaF or  $\text{H}_2\text{SiF}_6$ . Aluminium is readily attack by fluoride (Eq. 2-2) and is kept in solution as  $\text{AlF}_6^{-3}$  or precipitated in the bath as cryolithe.

$\text{Me} \rightarrow \text{Me}^{2+} + 2 \text{e} \text{ (Me = Zn, Fe)}$	2-1
$\text{Al}_2\text{O}_3 + 6 \text{HF} \rightarrow 2 \text{AlF}_6^{-} + 3 \text{H}_2\text{O}$	2-2

The removal of oxide layers and the roughening and cleaning of the surface is important for the nucleation of the phosphate crystals. The effect of alloying elements in steel on phosphating was investigated by Augustsson [28], who found a positive effect of some elements on the coating stability. Segregated metal oxides originating from the annealing step like Mn-oxide on the surface increase the reactivity of steel and lead to the incorporation of manganese in the phosphate layer yielding better stability. All acidic dissolution reactions consume  $\text{H}^+$ -ions and increase the probability of nucleation. The rapid dissolution of an oxide layer accelerates this process, especially when the oxides not fully cover the metal surface and favour the formation of a metal/metal oxide local element [15].

### 2.3.3.3 Reduction of H<sup>+</sup> and accelerators

While the metal is readily dissolved by the phosphating bath, hydrogen ions and the added accelerators are reduced in redox-reaction. The reduction of these species causes the necessary raise of the pH-value for nucleation.

From reactions (2-4 - 2-7) it can be seen, that the reduction of the various accelerating agents consumes usually more H<sup>+</sup>-ions per electron transferred than the simple formation of one hydrogen molecule would do (Reaction 2-3). Therefore the accelerators largely contribute to the metal dissolution and the increase of the pH-value, enhancing the reaction rate dramatically. It is important to note that the pH of the bath is usually just below the first endpoint in the titration curve of phosphoric acid so that the consumption of even a small amount of H<sup>+</sup>-ions can produce significant local pH-changes. The pH increase in the vicinity of the metal surface has been experimentally demonstrated using micro pH electrodes [29].

$2 \text{H}^+ + 2 \text{e}^- \rightarrow \text{H}_2$	2-3
$\text{NO}_3^- + 10 \text{H}^+ + 8 \text{e}^- \rightarrow \text{NH}_4^+ + 3 \text{H}_2\text{O}$	2-4
$\text{NO}_2^- + 2 \text{H}^+ + \text{e}^- \rightarrow \text{NO} + 3 \text{H}_2\text{O}$	2-5
$\text{NH}_2\text{OH} + 3 \text{H}^+ + 2 \text{e}^- \rightarrow \text{NH}_4^+ + \text{H}_2\text{O}$ or $2 \text{NH}_2\text{OH} \rightarrow \text{N}_2\text{O} + \text{H}_2\text{O} + 4 \text{H}^+ + 4 \text{e}^-$	2-6 [3]
$\text{H}_2\text{O}_2 + 2 \text{H}^+ + 2 \text{e}^- \rightarrow 2 \text{H}_2\text{O}$	2-7

Other oxidising agents, which have been tested and applied for phosphating, are nitrobenzene sulfonic acid [30], chlorates and bromates [1] and nitroguanidine [31]

In the absence of an accelerator, H<sup>+</sup>-ions are the only oxidants in the solution. They form hydrogen bubbles, which can block the surface and disturb the phosphating process. This inhibiting effect is greatly suppressed by accelerators due to the supply of another suitable reduction reaction.

From an electrochemical point of view, accelerators can be seen as cathodic depolarisers, which increase the total cathodic current on the treated metal. In presence of an oxidising agent in the phosphating bath the open circuit potential is shifted to more

cathodic values during the metal dissolution in comparison with an acidic attack without accelerators.

#### 2.3.3.4 Nucleation and crystal growth

The consumption of  $H^+$ -ions by various reduction reactions leads to an increase in the pH-value in the metal/solution-interface and to a shift in the acidic equilibrium according to Eqs. 2-8. The concentration of the phosphate ion is raised until it reaches the value determined by the solubility product of tertiary zinc phosphate leading to precipitation (Eq. 2-9).

$H_3PO_4 \leftrightarrow H_2PO_4^- + H^+$	2-8
$H_2PO_4^- \leftrightarrow HPO_4^{2-} + H^+$	
$HPO_4^{2-} \leftrightarrow PO_4^{-3} + H^+$	
$3 Zn^{2+} + 2 H_2PO_4^- + 4 H_2 \rightarrow Zn_3(PO_4)_2 \times 4H_2O$	2-9

The phosphate crystal start to cover the surface until the coverage sufficiently slows down the rate of metal dissolution, so that the necessary pH-increase for precipitation can no longer be maintained. The reaction comes to an end, although redissolution of the phosphate crystal can take place during long time exposure in the phosphating bath.

Phosphate crystals show epitaxial growth on the surface. Epitaxy is known as the phenomenon, when a guest crystal grows on the surface of a **polycrystalline** material with the same crystal orientation as the host phase. It is favoured, when the lattice parameters of guest and host are close to another and when the **supersaturation** of the solution is not too high [1]. For the growth of hopeite on a zinc substrate the difference of guest and host crystal planes is only 0.002 nm, which provides good conditions for epitaxial growth. During phosphating the primary crystals grow epitaxially with the initial surface, while secondary crystals nucleate on the surface of other crystal as the reaction goes on.

The thermodynamic requirements for crystal deposition are best met on so called active centres. On a metal surface conditioned for phosphating such centres usually are grain boundaries or the adsorbed activation particles. The number of crystals depends on



the number of such active centres initially present on the surface. This number can be influenced by the activation product used and the preconditioning, especially cleaning. An inverse relationship between crystal size and crystal number is observed, since a small number of large crystals and large number of small crystals give rise to the same coverage on the surface. The coating weight is usually higher when the surface is covered by large crystals.

The following scheme (Figure 1) sums up the described steps of phosphating.

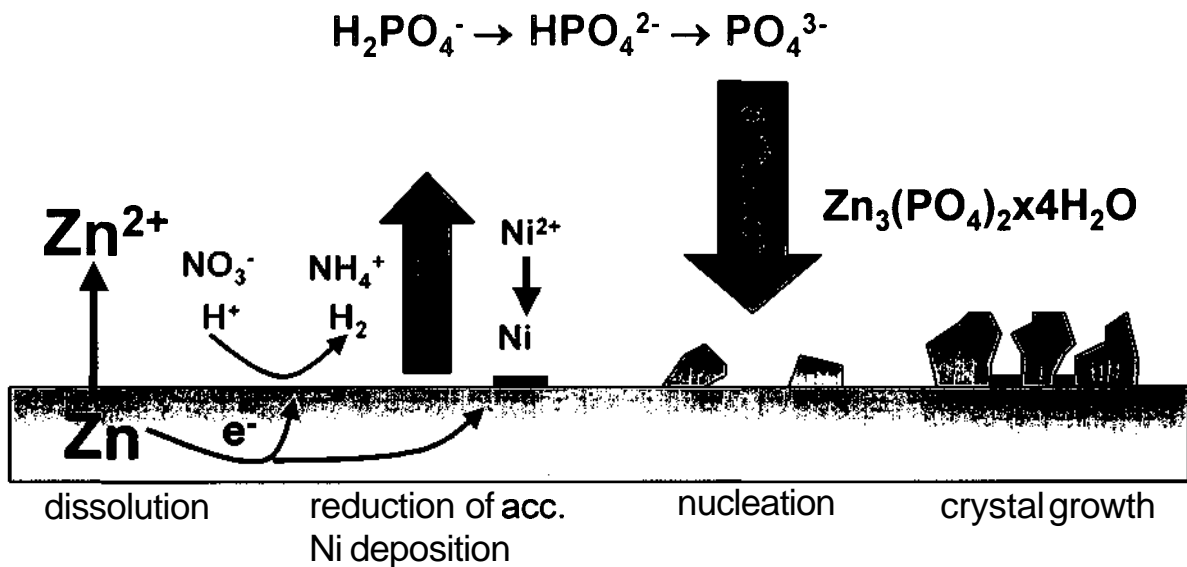


Figure 1: Scheme of phosphating reaction on zinc with the basic steps indicated by **Zn-dissolution**, reduction of accelerators and deposition of Ni, pH increase in the metal/solution interface and shift of phosphoric acid equilibrium, increase of phosphate-anion concentration near the metal surface and finally nucleation of zinc phosphate.

### 2.3.3.5 Post-treatment

To optimise corrosion protection metals can be treated by rinsing with special solutions after phosphating. Historically, the chromic acid rinse was the treatment of choice to increase the barrier effect against corrosion. In literature mainly two effects are thought to be responsible for the enhancement of corrosion resistance. First, the porosity (=the portion of metal not covered with the phosphate layer) is decreased by deposition of chromates on the bare metal between the crystals [30]. Other authors assume a modification of the layer by ion exchange of Zn and Cr in the upper surface of the crystals [15, 32, 33]. Thus the phosphate layer becomes more stable against alkaline media and corrosive attack. The removal of easily dissolving or unfinished parts of the phosphate

layer by a chromic acid rinse was also reported [34]. This leads to minor dissolution of crystal during cataphoretic painting and hence a better paint adherence.

**However**, due to problems with ecological noxiousness and toxicity of Cr(VI), alternative treatment substance gain more and more importance in industry. These substances may contain other metal cations with or without the addition of an organic compound as monomer or polymer. Popular examples are products containing **fluoro-**complexes of Zr and Ti together with **polyacrylates**, silanes or another organic compound. Equally good or slightly worse results can also be obtained with solutions containing only Cr(III) (**chromitation**), avoiding the presence of Cr(VI), but utilising the advantages of chromium in the layer.

## 2.4 NATURE OF THE PHOSPHATE LAYER

The phosphate layer consists of an array of discrete crystals in the form of needles, flakes or tiles. They are usually around 1 to 10  $\mu\text{m}$  in diameter, with a coating weight in the order of 1 to 6  $\text{g}/\text{m}^2$  (Figure 2).

The basic function of the layer is to promote the adhesion of paint and increase the corrosion resistance of the painted product. Without paint, the corrosion resistance of phosphated zinc coated steel is only slightly higher than of the pure metal. The better adhesion of the paint is accomplished by the surface roughness of the phosphate layer, where organic coatings may anchor in lock and key type of mechanism.

Whereas **exposure** of the substrate metal between the phosphate crystals is detrimental to the corrosion resistance, some remaining porosity is essential for the cataphoretic paint process [35], which depends on current flow during deposition. The paint starts to deposit in the pores and then extends towards the exterior crystal surface.

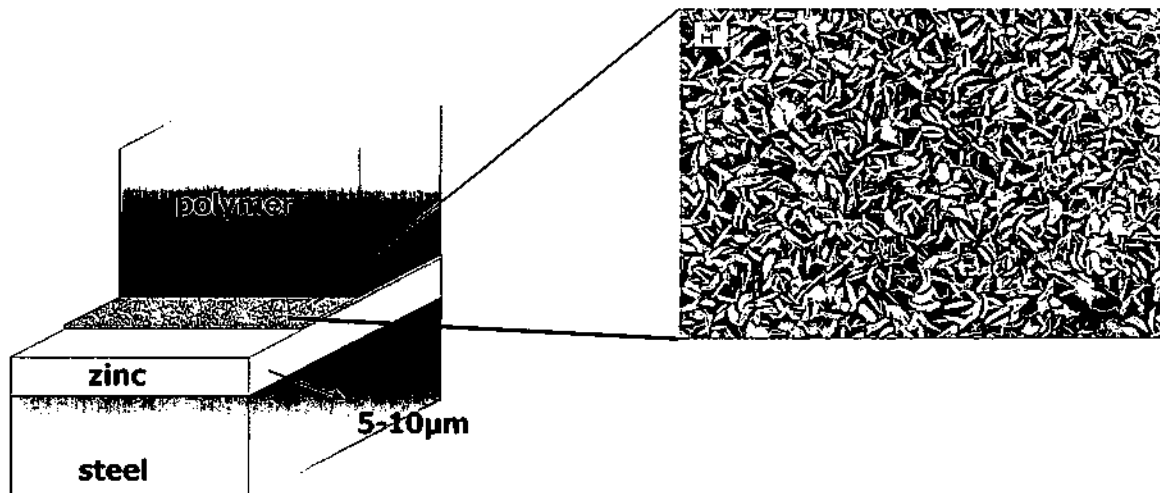


Figure 2: Phosphate layer as the very interface between metal and polymer coating. SEM picture on the right - discrete phosphate crystals and the high micro roughness are clearly visible.

#### 2.4.1 CRYSTAL PHASES IN PHOSPHATE LAYERS

The composition of the phosphate layer is determined by the bath composition and by the nature of the substrate metal. On zinc coated steel the product of phosphating with a trication bath is hopeite ( $\text{Zn}_3(\text{PO}_4)_2 \times 4 \text{H}_2\text{O}$ ) throughout the whole layer. On steel a mixture of hopeite and phosphophyllite ( $\text{Zn}_2\text{Fe}(\text{PO}_4)_2 \times 4 \text{H}_2\text{O}$ ) is found. Since the Fe in the layer comes from the pickling of the metal, phosphophyllite accumulates in the vicinity of the metal surface. The crystal structure of hopeite was determined by Hill and Jones [36] and is shown in Figure 3. In presence of Mn and Ni-ion in the bath, an incorporation of these ions into the crystal lattice of hopeite and phosphophyllite takes place. The replacement of **Zn-atoms** changes lattice parameters and the physical and chemical properties of the phosphate crystals, like dehydration behaviour and stability in alkaline solutions.

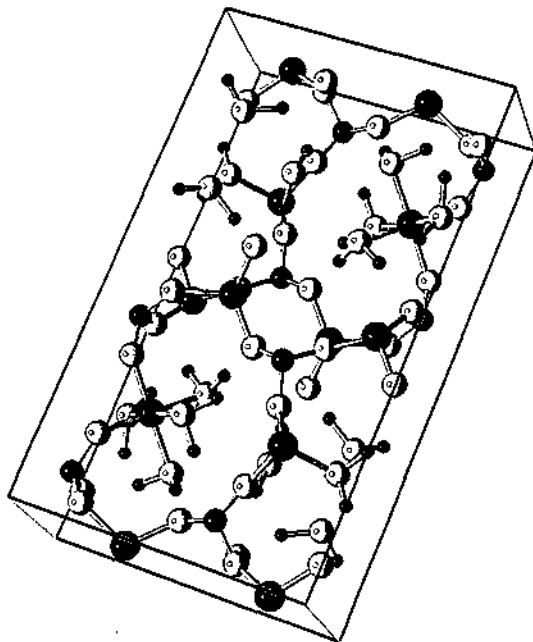


Figure 3: Crystal structure of hopeite. Crystallographic data according to Hill and Jones [36] was imported and drawn with the program Balls and Sticks [37]

•Zn OO OP ●H

## 2.4.2 INFLUENCE OF HEAVY METAL IONS

Modern phosphating processes contain heavy metal ions like Mn, Ni and Cu apart from Zn in the bath. Manganese incorporates into the crystal lattice of hopeite on the octahedral and tetrahedral sites, while Ni replaces Zn only in the octahedral sites [38]. The ratio of Mn and Ni in the crystals is therefore higher than in the bath composition. The incorporation of  $Cu^{2+}$ -ions into the lattice was not proved and can be excluded. The incorporation of atoms other than zinc into hopeite has some important consequences on the properties of the phosphate crystals.

Crystals containing Mn show an increased stability in alkaline solution and higher temperatures of dehydration [38, 39]. These improvements are also observed on Ni-containing crystals, but to a smaller extent, since the incorporation rate of Ni is lower compared to Mn. Merely the decreasing effect on the thermal expansion coefficient of the crystals is around 10% higher with Ni.

Both Mn and Ni cause a refinement of the crystal size and a change of the habitus, leading to lower coating weight than resulting from pure Zn-phosphating bathes [40, 41, 42]. Ni and Mn in the phosphate layer generally cause an improved paint adhesion and corrosion resistance. On zinc substrates, Ni deposits as metal on the surface during the

phosphating reaction [43], which accelerates the overall phosphating rate by an additional cathodic reaction and ensures that zinc metal surface between the phosphate crystals is protected by metallic nickel. Copper is especially added as replacement for Ni and can be applied at much lower concentrations in the bath to unfold its effect. On steel and zinc Cu will cementate [43] and close the pores between the crystals similarly to Ni. An improved corrosion resistance is observed because of the cementation, although paint adhesion can suffer from the presence of metallic copper, in particular on a zinc surface.

## 2.5 CHEMICAL STABILITY OF PHOSPHATE LAYER

The stability of phosphate layers in acidic solution is quite low [44, 45]. Moreover, no perceptible differences were observed on crystals containing Mn and/or Ni, equally the stability of hopeite and phosphophyllite in acidic solution is negligible. The mechanism of dissolution in acids is different from those in alkaline and generally leads to a complete removal of the layer, leaving no remainders behind [45].

However, during its lifetime a phosphate layer usually is exposed to solutions of high pH-values rather than low ones. Alkaline degreasing steps and cataphoretic painting expose the phosphate layer to highly alkaline solution already in the production line. Atmospheric corrosion of painted metals locally induces high pH-values under the paint, which causes dissolution of the phosphate interface and delamination subsequently. Therefore the stability of phosphate layers in alkaline media is directly related to their protective behaviour against corrosion (see next chapter 2.6)

As mentioned above, Mn and Ni have a positive effect on the alkaline stability of hopeite, as well as phosphophyllite is more stable than hopeite. Highly alkaline solutions leach out the phosphate leaving behind a hydroxide layer consisting of Zn and the other metal cations, like Mn, which is thought to stabilise the hydroxide layer [46]. Remainders containing zinc were only found in solutions with lower agitation, because the pH-values in the metal/interface is lower and the formation of  $Zn(OH)_2$  is favoured. For well stirred solutions the reaction proceeds on with active dissolution of the zinc hydroxide to zincate [45].

## 2.6 CORROSION MECHANISM

Phosphate conversion coatings are commonly used on zinc coated steel, particularly in association with cathodoretic electropainting in the automotive industry. To this end, the specific corrosion behaviour of zinc coated steel covered with a polymer layer is of great interest. A number of works specifically focussed on the corrosion mechanism of painted steel. The publications cover **parametrical** studies by standardised corrosion tests, together with surface analytical methods and identification of the corrosion products [32, 47, 48, 49], as well as sophisticated localised electrochemical methods like the scanning Kelvin probe and the scanning vibrating electrode technique [50, 51, 52] to elucidate the complex phenomenon of under paint corrosion.

The multicomponent interactions between paint, the zinc coating, steel and the environment render this type of corrosion far more complex than the well understood reactions occurring on pure metal surfaces [53]. Particularly on car bodies we talk about two types of corrosion, namely perforation and cosmetic corrosion. Corrosion of painted and zinc coated steel that initiates from the interior of a car body is known as perforation. It often occurs at locations that are difficult to clean, phosphate and paint, such as lapped parts and hem flanges. Cosmetic corrosion is the type that occurs on the exterior surface and generally starts at damaged areas in the paint. The interactions of the environment, the zinc and the steel will cause the build up of corrosion products and the paint to delaminate.

Usually the protective performance of the finished steel is assessed by standardised corrosion tests of industrial relevance. A painted sample is damaged in a reproducible way (e.g. scratched with a knife) and exposed to a corrosive environment, which should nearly correspond to real conditions, but at an accelerated rate. Therefore the corrosive environment is often not kept in a certain state, but changed periodically with time. The VDA scab corrosion test (detailed description in the experimental section 4.3) is an example of such tests, which gained high importance in the steel and automotive industry in Europe. Although such tests are of great usefulness for quality control and product development, they often do not enable elucidation of the specific reactions taking place during the corrosive attack. The samples are not accessible to surface analytical or localised electrochemical methods during the test, if at all only under a high experimental effort.

The delamination mechanism of paint during the atmospheric corrosion of zinc coated steel may be divided into two broad categories depending upon whether the rate is determined by the cathodic or the anodic part of the corrosion reactions. The anodic reaction herein is represented by the active dissolution of the metal. It is usual on zinc surfaces, particularly when coupled to steel.

Anodic undermining due to zinc dissolution was observed to be the predominant factor controlling the delamination, at least in the initial stages of the attack [47, 48]. Localized electrochemical methods like the Scanning Kelvin Probe revealed anodic activity of zinc, when bare steel surface is exposed to the corrosive environment, usually by a scratch through the paint and the zinc coating [54]. However, the delamination mechanism may work differently, when the scratch only reaches down to the zinc surface.

In case of exposed steel this area is **cathodically** protected by zinc dissolution. The dissolved zinc ions precipitate as corrosion products on the steel surface and cover it. Additionally the build up of corrosion products in the very interface between the damaged and the intact area causes the paint to delaminate simply by mechanical expansion force.

The cathodic delamination mechanism is common for the cosmetic corrosion of painted steel, and under certain circumstances, galvanised steel [51, 55, 56]. In this mechanism, oxygen reduction occurs under the paint giving rise to a significant increase in the pH in the interfacial region between the paint and the metal substrate. pH values greater than 14 have been measured under certain circumstances [57, 58]. The exact mechanisms of disbonding during cathodic delamination are poorly understood. One important factor is thought to be the alkali catalysed dissolution of the interfacial conversion layer and / or degradation of the polymer [59]. The localisation of the cathode and the anode during paint creep from a scratch was investigated by surface analytical methods (ESCA) and by means of the Kelvin probe [54]. With the help of identification of the corrosion products, the prevailing type of corrosion in the surface region of interest can be discovered. From the **potential-pH** diagram (Figure 4) the various stable zinc corrosion products in presence of chloride ions can easily be seen. In the alkaline environment of the cathodic area ZnO is the stable species, whereas  $ZnCl_2 \cdot xZn(OH)_2$  is found in the acidic areas of the anode [60]. The type of different products also reflects the diffusion of ions in the corrosive electrolyte due to maintenance of the ionic balance. The presence of sodium ions indicates the cathodic region, because of the **hydroxyl-ion** produced. Anions, like chloride, diffuse away from this region and establish the ionic balance in the anodic region.

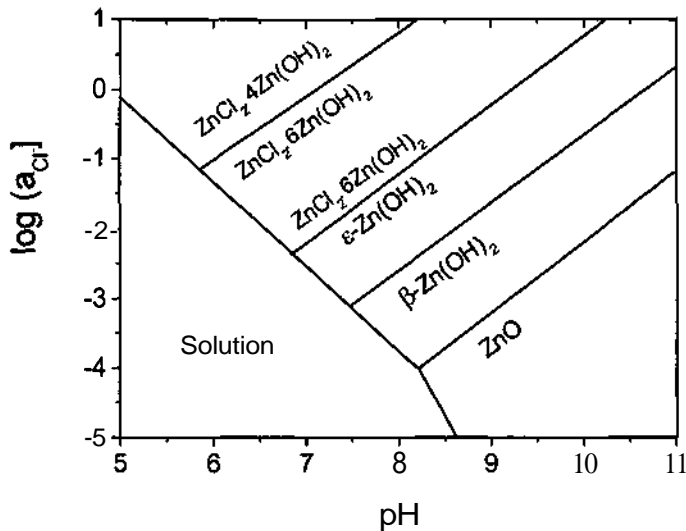


Figure 4: Equilibrium diagram for corrosion products of zinc in a chloride environment. After Feitknecht, cited in Zhang [53]

According to various papers the delamination of painted and zinc coated steel starts by anodic undermining due to zinc dissolution [47, 54, 61]. The steel surface will act as the cathode in this initial phase. As the attack goes on, corrosion products cover the bare steel surface and minimise its ability for maintaining the cathodic reaction. The overall rate of delamination is distinctly decreased after the initial phase. In the following stage the diffusion of humidity and oxygen through the paint becomes an important factor. Additional to the defect area, a second cathode builds up at the metal/paint interface just at the transition from intact to delaminated paint area. A small cathode now runs in front of the anode, where the metal/paint interface is undermined due to active zinc dissolution. The cathodic reaction weakens the bonding between metal and paint by attacking the interfacial layer, which would be a phosphate layer in most cases. The weakening exposes fresh zinc surface again available for anodic dissolution. The reaction of the phosphate layer with the alkaline environment in the cathodic region may result in significant modifications of the phosphate crystals, with complete leaching of the phosphate layer [45]. If the reaction is complete, the conversion layer may be destroyed leading to immediate disbonding of the polymer layer. However, if the phosphate layer is not destroyed, the reaction may actually delay the progression of cathodic delamination by neutralising the hydroxide ions thereby maintaining a less aggressive environment under the paint. Due to its amphoteric character, zinc may also be readily dissolved by the highly alkaline environment in the cathodic area.



Whereas on steel the delamination mechanism is purely cathodic, on zinc coated steel the mechanism is a complex combination of cathodic delamination and anodic undermining. Both types occur simultaneously at different rates. Figure 5 sums up the described corrosion phenomena in a schematic drawing.

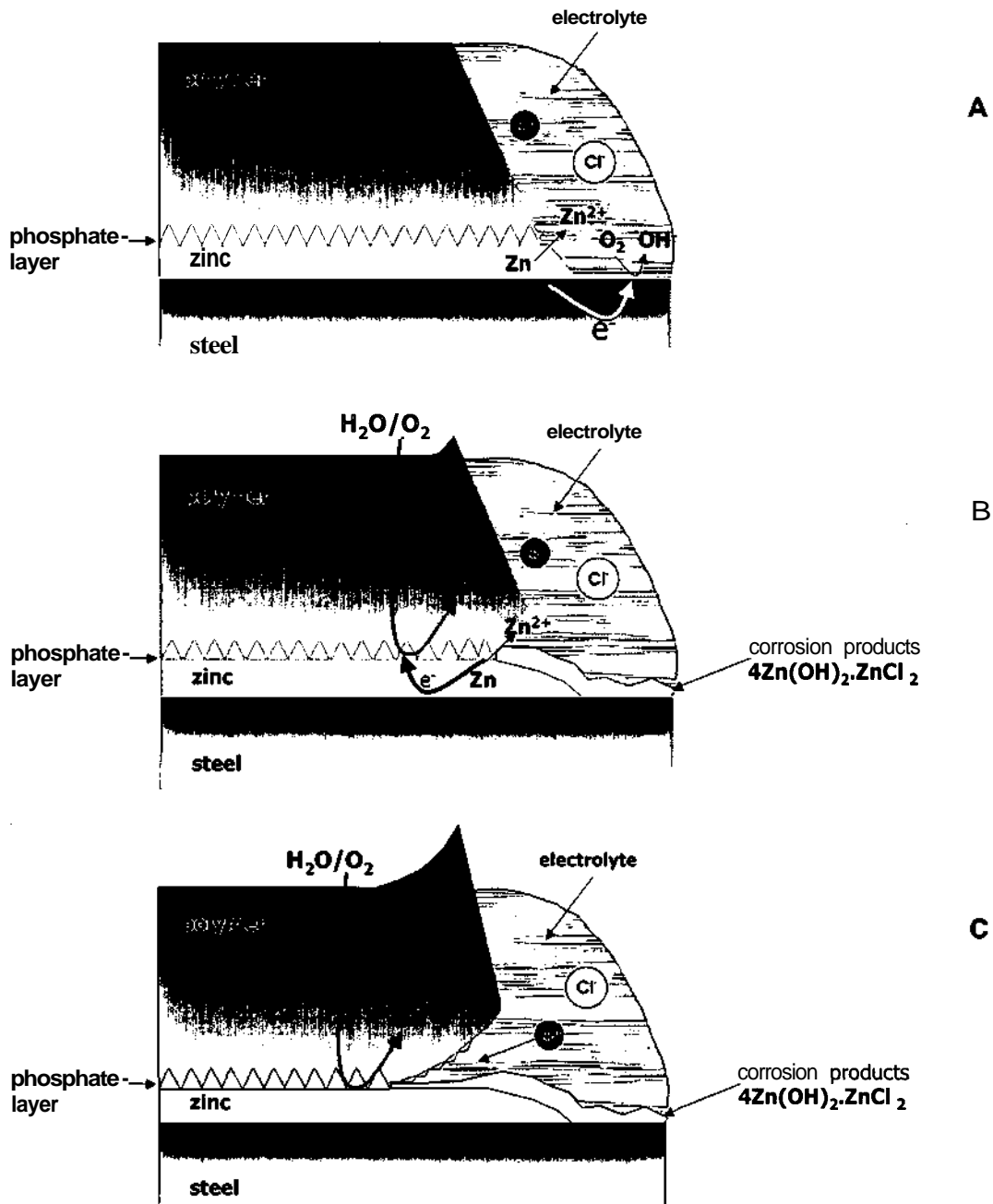


Figure 5: Schematic view of under paint corrosion on zinc coated and phosphated steel. For detailed description see text. (a) initial phase (b) build-up of corrosion products (c) propagation of paint delamination

## 3 THEORETICAL BACKGROUND OF THE METHODS

The fundamentals and theoretical backgrounds of the three major methods applied in this work will be described shortly in this section. The detailed experimental procedure and the instruments used are treated in the next chapter.

### 3.1 RAMAN SPECTROSCOPY

#### 3.1.1 BASICS OF VIBRATIONAL SPECTROSCOPY

The two major types of vibrational spectroscopy are infrared (IR) and Raman spectroscopy [62]. Spectral bands are observed, because of photon absorption or emission due to changes in the energy state in the molecules of the investigated species. Both in infrared and in Raman spectroscopy this energy changes are changes in the vibrational modes in molecules. In a simple picture of molecular vibrations, the molecules are thought to consist of atoms with a certain mass, which are connected by elastic bonds. As a result, they can perform periodic motions, which define their vibrational spectra. From the spectra, we yield molecular bonding information, due to the fact, that under an ideal classical view the energy of the vibration of two atoms depends on their mass as described by Hooke's law. However, vibrational spectra of complex molecules or crystals mainly are formed by a number of vibrations of different intensity, which are coupled together. Identification of a vibrational band is therefore usually done best by comparing with reference spectra.

Although the physical background of the spectral bands is the same in infrared and Raman spectroscopy, the mechanism of the excitation of the molecular vibrations is accomplished in different ways. Moreover, molecular vibrations may be excited in one method and not excited in the other. In terms of quantum mechanics one speaks of allowed and forbidden transitions. As a result the IR spectrum of a certain substance usually differs from its Raman spectrum.

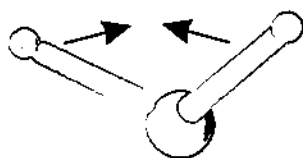
In IR spectroscopy the molecular vibrations are excited by infrared light and the absorption of the light at different wavelengths is detected. Raman spectroscopy on the

other hand depends upon the measurement of wavelength and intensity of inelastically scattered light from molecules. It involves excitation with light that is not absorbed by the sample. Most of the exciting light passes directly through the system or is elastically scattered, that means, it is scattered without a change in photon energy (Rayleigh scattering) Some photons exchange energy with the sample and are inelastically scattered, with a change in wavelength reflecting the loss or gain of energy. This is the Raman effect of light interaction with matter, which was predicted by Smekal and first discovered by Raman [63].

The Raman scattered light occurs at wavelengths that are shifted from the exciting light by the energies of the molecular vibrations. This Raman shift expressed in wave number [ $\text{cm}^{-1}$ ] represents the Raman spectrum and can be easily compared with IR spectra. The probability of Raman scattering depends on certain selection rules, but under most circumstances is quite small (fraction of 1 to  $10^8$  photons).

Simply spoken the selection rules determine the possible vibrational modes, which can be excited. In IR spectroscopy an allowed vibration requires that the dipole momentum of the molecule changes during this vibration. For Raman spectroscopy a change in the polarisability is the necessary condition. Therefore, as an example, a pure symmetrical vibration, which does not change the dipole momentum of the molecule, but its polarisability is only detected in Raman spectroscopy.

Figure 6 depicts the selection rules for IR and Raman active vibrations by means of vibrational modes of the water and the phosphate molecule. IR and Raman spectroscopy are no competing methods, but together provide complementary information, because the selection rules are different.

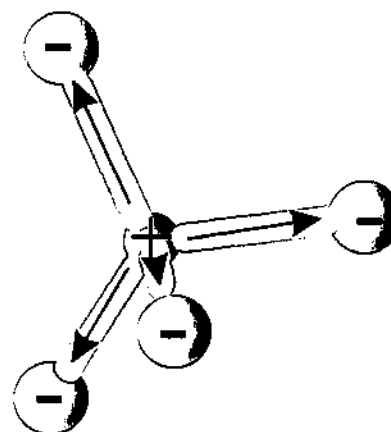


**A**

Figure 6: Molecular vibrations of the water molecule (a) and the phosphate anion (b).

(a) Deformation vibration of  $\text{H}_2\text{O}$ -molecule, change of dipole momentum - strong IR activity

(b) Symmetrical stretching vibration of the  $\text{PO}_4^{3-}$ -anion, no change of the dipole momentum, but change of polarisability - strong Raman activity



**B**

### 3.1.2 QUANTUM MECHANICAL MODEL

The scattering process in Raman spectroscopy can be viewed as a simple quantum mechanical model as depicted in Figure 7.

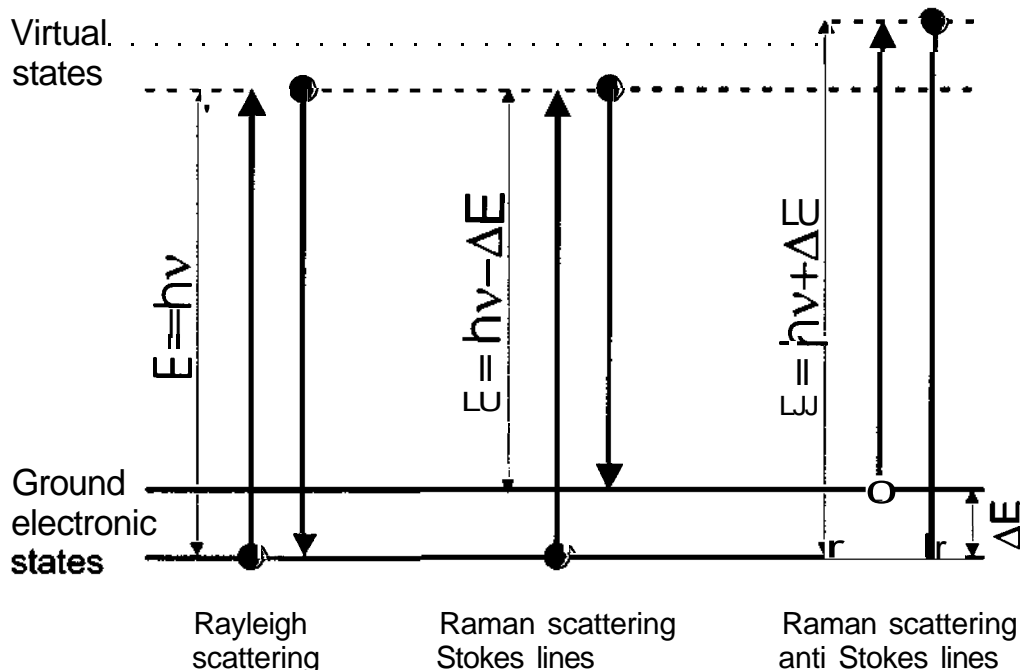


Figure 7: Schematic view of Rayleigh and Raman scattering. Excitation ( $h\nu$ ) to a **nonstationary** virtual state is followed by Rayleigh scattering with no change in energy ( $E = h\nu$ ), or Raman scattering with lower photon energy (Stokes lines) or with higher photon energy (anti Stokes lines). According to Colthup [63].

In quantum mechanics the incident photon can be viewed as raising a molecule to a "virtual state", which is a non-stationary state of the system. De-excitation to the original state can happen without loss of energy (Rayleigh scattering) or to a final state other than the original state (Raman scattering). Vibrational bands are divided into Stokes and anti-Stokes lines. The energy of the scattered light is lower than the incident radiation (that means higher wavelength) for the Stokes lines and is higher for the anti-Stokes lines (Figure 8). The energy increase or decrease from the excitation is related to the vibrational energy spacing in the ground state of the molecule and therefore the wavelength of the Stokes and anti-Stokes lines are a direct measure of the vibrational energy.

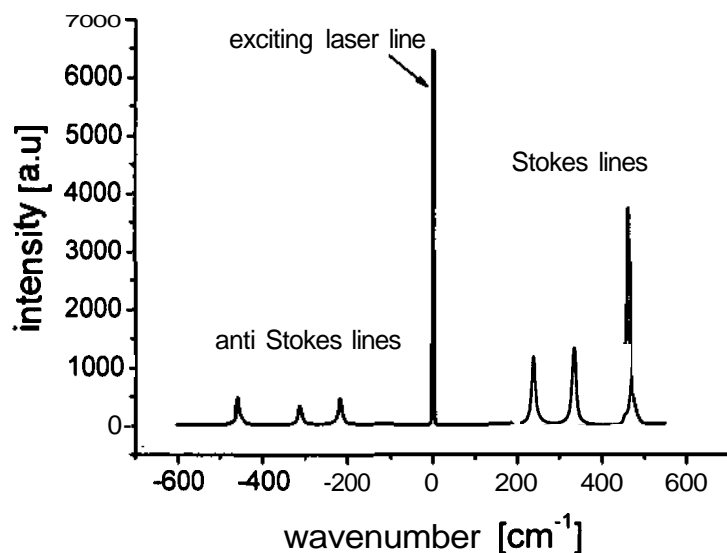


Figure 8: Raman spectrum of  $\text{CCl}_4$  (recorded with the instrument used in this work - see experimental section chapter 4.6) - Stokes and anti Stokes lines are seen. HeNe-laser, recording time 5 s, objective 10x

The appearance of anti-Stokes lines needs molecules, which are already in an elevated energy state and hence are of lower intensity, particularly at room temperature. It is the branch of the Stokes lines, which is usually studied.

Raman spectroscopy is usually carried with excitation and detection in the visible region of the spectrum, it can be employed in cells with glass windows and aqueous solutions, both of which are strong absorbers in IR experiments. Since the probability of Raman scattering is quite small, experiments must involve intense monochromatic light sources. A monochromatic light source is essential, because the observed Raman shifts are rather small on the order of 100 to 3000  $\text{cm}^{-1}$ . Typical sources are lasers in the visible region, like the HeNe laser (632 nm) or the NdYAG-laser (532 nm). When the Raman spectrometer is additionally equipped with a microscope, the laser light can be focussed via the microscopic objective onto the samples. This gives excellent lateral and depth resolution for surface analysis [64].

## 3.2 QUARTZ CRYSTAL MICROBALANCE

### 3.2.1 THE PIEZOELECTRIC EFFECT

Quartz is the crystalline form of  $\text{SiO}_2$ . Its specific **non-centrosymmetric** structure gives rise to a number of physical properties, one of which is the piezoelectric effect. In crystals, which show piezoelectricity, pressure on a section of the crystals results in a shift in charge distribution. This can be detected as a change in the electric field between the faces of the crystal section and is referred to as the direct piezoelectric effect.

The converse piezoelectric effect is the phenomenon, whereby a crystal becomes strained, when electrically polarised due to the physical displacement of the atoms. It is the phenomenon, which is utilised in the quartz crystal microbalance (QCM).

In general, piezoelectricity exists in materials that crystallise in a non-centrosymmetric space group. A single crystal of an acentric material will possess a polar axis due to dipoles associated with the arrangement of atoms in the crystalline lattice. The charge generated in such a crystal under mechanical stress is a manifestation of a change in the net dipole moment.

### 3.2.2 QUARTZ CRYSTALS FOR QCM

Quartz crystals used as piezoids in practical applications today are mostly synthetic ones produced in the hydrothermal route [65]. Piezoelectric resonators are prepared by cutting the desired parts from large single crystals of alpha-quartz at a certain angle with respect to the crystalline axes. The AT cut, which is most commonly used for QCM applications, is fabricated by slicing through a quartz rod at an angle of  $35^\circ$  with respect to the **crystallographic** z axis. (Figure 9) The reason for its popularity is its nearly zero temperature dependence on the resonance frequency near room temperature.

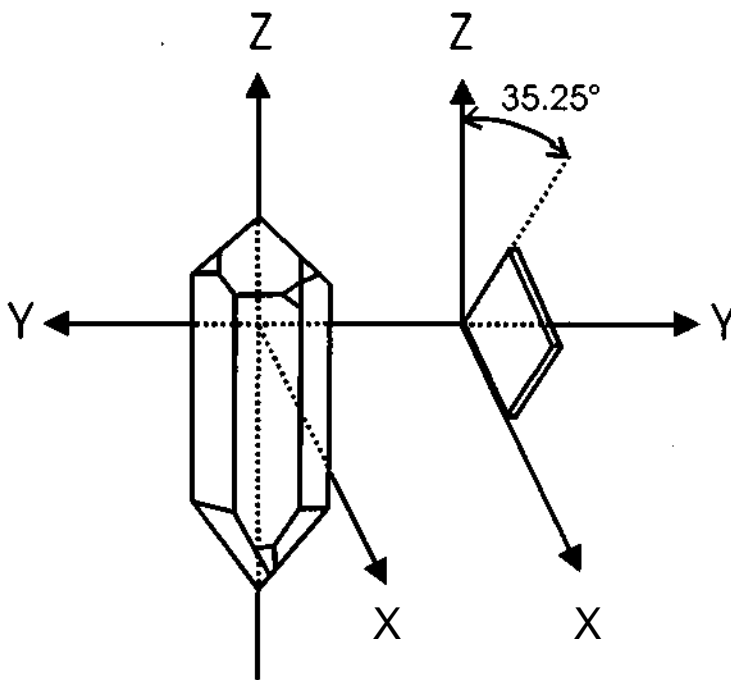


Figure 9: Quartz crystal and orientation of AT cut.

Piezoids used in the QCM are usually disc shaped. In order to apply the required electric field to the crystal, it is necessary to supply conductive layers to opposite faces of the disc, whereby leads to a suitable field generator (oscillator) can be attached. This is commonly done by evaporating metals such as gold or platinum on the faces to form electrodes. Most of the vibration occurs, where the electrodes overlap - this is the piezoelectrically active area [66]. Crystal symmetry dictates that the strain induced in a piezoelectric material, by an applied potential of given polarity, will be equal or opposite in direction to that resulting from the opposite polarity. Thus an alternating potential across the crystal, with electric field lines normal to the disk surface, results in vibrational motion of the quartz crystal. Since the piezoid is a solid body, the vibration caused by an oscillating electric field can occur in identifiable directions and at resonance frequencies dependent on the mass, thickness and shape of the piezoid and the orientation of the field relative to the optical axis, i.e. cut. For AT cut quartz crystal the vibration direction called mode is the shear deformation (Figure 10).

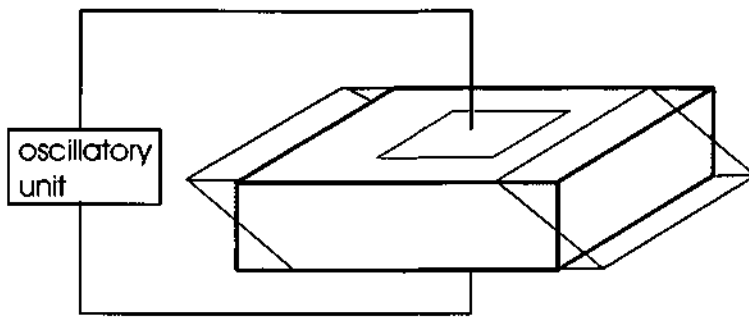


Figure 10: Deformation of quartz crystal due to converse piezoelectric effect. Red lines indicate shear deformation of AT cut crystal.

### 3.2.3 MASS-FREQUENCY RELATIONSHIP

It has been stated above that mass changes at the quartz surface (resp. the conductive electrode layers) may be obtained from the change in the resonant frequency of the QCM. However, several conditions must prevail to allow for the quantitative correlation of frequency changes with mass changes.

Factors, which affect the resonance frequency and deviations from this frequency, include: [67]

- physical properties of the quartz disc (thickness, density and shear modulus)
- density and viscosity of the phases adjacent to the piezoid
- ambient temperature and pressure difference across the disc
- mass of attached electrode or of adsorbate and depositions on attached electrodes

The first quantitative treatment that provided a relationship between mass changes and frequency changes was developed by Sauerbrey [68], whose work lead to an equation, taking only attached electrode mass into account and maintaining all other parameters constant (3-1).

$\Delta f = - \left( \frac{2f_0^2}{A\sqrt{\rho_q\mu_q}} \right) \Delta m$	3-1
---	-----



In Eq. 3-1  $f_0$  is the resonant frequency of the QCM resonator prior to the addition or removal of mass (in units of Hz) and  $\Delta f$  is the frequency shift from the resonance value.  $\Delta m$  is the mass change causing the frequency shift. The piezoelectrically active surface area (area of conductive layers) is represented by  $A$ , while  $\rho_q$  is the density and  $\mu_q$  is the shear modulus of the quartz. The equation is perhaps more frequently written as:

$\Delta f = -C_f \Delta m$	3-2
----------------------------	-----

Here  $C_f$  is a constant containing all invariable parameters of the quartz properties in Eq. 3-1. It expresses the mass sensitivity and has the unit  $\text{Hz cm}^2 \text{g}^{-1}$ . It is seen clearly, that the higher the fundamental resonance frequency of the **crystal**, the better the mass sensitivity. However, high frequency resonators are necessarily very thin and fragile and difficult to handle.

### 3.2.4 DEVIATIONS FROM THE SAUERBREY EQUATION

#### ***Contributions to the apparent mass***

When the QCM is used in electrolytes and layers are deposited or removed from the electrode areas, various factors beside the apparent mass change have an influence on the resonance frequency. Thus deviations from the theoretical presumptions in the Sauerbrey equation may occur.

The most evident change is observed in the attenuating of the vibration of the quartz crystal when in contact with a liquid. Kanazawa and Gordon [69] quantified the effect of a layer of solution closest to the crystal surface. Generally, the electrolyte dampens the vibration of the quartz, because of an energy loss due to the formation of a shear wave inside a thin liquid layer near the quartz surface. The magnitude of this effect is determined by the viscosity of the electrolyte, which in turn depends on the temperature.

However, there is also a temperature dependence of the resonant frequency, which depends on the design and manufacturing procedure of the crystal. This intrinsic dependence is caused by changes of the density and the shear modulus with

temperature, which were already shown as important parameters in the Sauerbrey equation (Eq. 3-1).

Another condition for fulfilling the Sauerbrey equation is a rigid adhesion of the deposited film to the **piezoelectrically** active area of the quartz crystal. Loosely precipitated material or undesirable adsorption of species again falsify the apparent mass as it is determined by the frequency change.

A film of material being deposited on a QCM contributes directly to mass change of the piezoid. When the growing film is not smooth, the liquid trapped within the depressions contributes to the apparent mass change [70]. As depicted in Figure 11, the included liquid in the dips and depressions of the surface will be dragged by the shear wave and will consequently be measured as attached mass similar to a rigid solid film on the surface. This influence can be taken into account theoretically [71], when the average size of the hollows ( $\epsilon$ ) is known and the amount of trapped liquid can be determined.

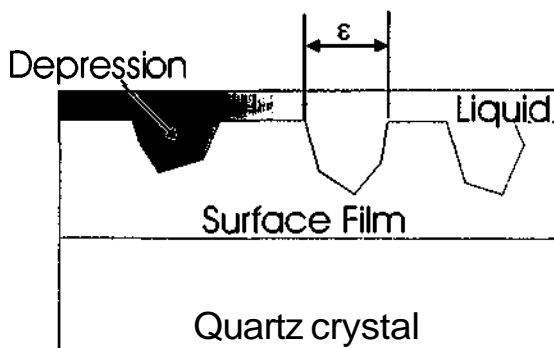


Figure 11: Surface depressions and roughness entrap liquid, which contributes to apparent mass change in QCM experiments.

Finally, it is well known that the mass sensitivity of the QCM is not constant across the active area. Rather, the mass sensitivity is given by a Gaussian function with a maximum at the centre of the quartz disk and a minimum near to its edge [66]. Therefore another consideration relating to the quantitative correlation of frequency and mass is the uniformity of the deposited film.

### 3.3 ICP ATOMIC EMISSION SPECTROSCOPY

#### 3.3.1 ATOMIC SPECTRA

If polychromatic light is sent through a gas in atomic state, the appearance of characteristic absorbed spectral lines is observed. The wavelengths of the lines are specific for a certain element. Similar to the absorption, emission of light at specific wavelengths can be evoked, when atoms are brought into an excited state. The basis for the observation of characteristic spectral lines by excited atoms lies in the electronic structure of the atoms and can only be explained by quantum mechanics. When energy is imposed on atoms (e.g. in thermal, optical or electrical form), the electrons can be elevated from the low energy orbitals to outer orbitals with higher energy. The atom then is not in the basic state anymore, but in an excited electronic state. Once in excited state the atom quickly decays back to lower energy levels. Average duration is around  $10^{-8}$  s. When the electrons jump back to the lower energy level, their energy is emitted as light, exactly one photon for one electron jump. For energy conservation the energy of the photon must be the same as the difference of the energy levels. Since electrons exist in certain orbitals at certain energy levels, only certain discrete values of such energy differences and thus only specific frequencies of the emitted light are possible. The quantum mechanical picture of this process is shown for two spectral lines of the **Na-atom** (Figure 12).

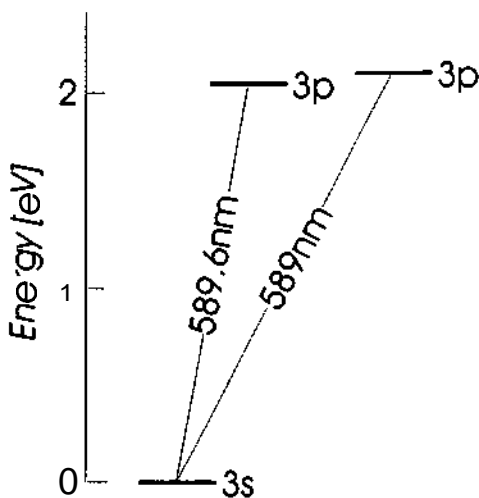


Figure 12: Energy scheme of two spectral lines shown for the sodium atom. Wavelength of the electronic transition is also shown. This excitation is used for the sodium lamp.

The energy differences between original and elevated state are determined by the distance of the electron from the nucleus. Spectral lines coming from electron jumps in the outer orbitals therefore have a lower frequency (in the visible region) than lines caused by jumps out of the inner orbitals near the nucleus (in x-ray region). Depending on the wavelength of the emitted light, optical spectra (in **UV/VIS**) and x-ray spectra are distinguished. Atomic emission spectroscopy usually works with the lines in the ultraviolet and visible region of the spectrum.

### 3.3.2 EXCITATION

Atomic (optical) emission spectroscopy (AES or OES) uses quantitative measurement of the optical emission from excited atoms to determine **analyte** concentration. For analytical applications the analyte has to be atomised in a reproducible and complete manner without too much matrix effects. Solutions are usually aspirated and nebulised, before they get atomised by a flame, discharge or plasma. One popular and powerful excitation method for AES is the Inductively Coupled Plasma (**ICP**).

Plasma is understood as a gaseous mixture of cations and electrons in high concentration, which conducts electric current. An ICP is a very high temperature (7000-8000 K) excitation source that efficiently vaporises, ionises and excites atoms. After nebulisation of the solution to be analysed it is entrained in a flow of support gas, which is typically argon as the real plasma source. The plasma torch (Figure 13) consists of concentric quartz tubes, whereby the inner contains the sample as aerosol and the Ar support gas. The outer tube is flowed with another gas stream, which is needed for cooling down the inside quartz tube. A radiofrequency generator produces an oscillating magnetic field in the induction coils wrapped around the outer tubes. The oscillating magnetic field in turn sets up an oscillating current in the ions and electrons of the support gas (argon). By collision with the ionised argon atoms, the analyte gets atomised and excited as well. The developing plasma has a toroidal shape with no contact to the tubes. This creates a simple background spectrum with low matrix effects and a high signal to noise ratio. Additional important advantages of the ICP technique are its sensitivity to most metallic elements as well as many non-metals and the possible aspiration of almost any liquid even with very high salt concentration. The later point is very important for the study of industrial surface treatments.

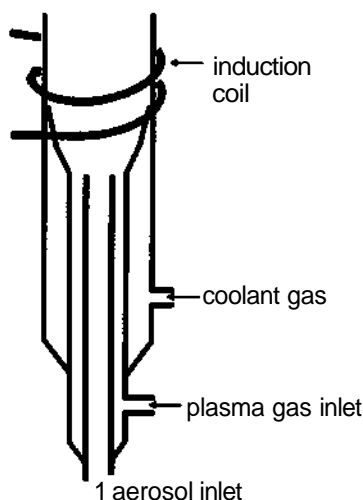


Figure 13: Schematic picture of typical ICP plasma torch.

### 3.4 THE METHODS IN LITERATURE

Numerous studies involving in-situ Raman spectroscopy coupled with electrochemistry have appeared in the literature with considerable impact on questions related to catalysis, corrosion and electrochemistry. For instance, the technique has proven particularly interesting for the investigation of oxide scale pickling [72] to cite one example within the context of surface treatment.

In this work Raman spectroscopy was used to observe the attack of alkaline media on the phosphate layers on zinc-coated steel with the object of estimating reaction rates for different layers and to identify the final products of the attack. The major research effort in this area has been in characterising the corrosion and adhesion properties of the final painted product [47,48] (See chapter 2.6 p. 16).

A short glance at literature shows, that no in-situ Raman studies have been performed concerning the chemical stability of phosphate layers in alkaline media. This is surprising as Raman is very sensitive to phosphate, and the spectra are highly characteristic of the exact nature of the phosphate species including the crystalline form and the level of hydration. Hopeite,  $\text{Zn}_3(\text{PO}_4)_2 \cdot 4\text{H}_2\text{O}$  which is one of the more common phosphate species on zinc surfaces, has a strong symmetrical stretching vibrations at  $996 \text{ cm}^{-1}$  [73]. Raman spectroscopy is therefore especially suited to complement other techniques like the QCM and the ICP-AES, which do not directly yield information concerning the molecular composition of the conversion coating.

However, Raman spectroscopy was applied to characterise the final phosphate layers by Sato et al. [74]. Sommer and Leidheiser were the first to use Raman spectroscopy for characterising the dissolution behaviour of zinc phosphate removed from coatings after long time exposure in various alkali metal hydroxides [75]. Less attention has been paid to understanding the mechanism of the improvement in chemical stability by the added metal cations on the kinetic and mechanistic side.

In situ **ICP-AES** is a very powerful solution analytical technique. It directly measures the partial elemental dissolution reactions either under spontaneous reaction conditions or with electrochemical polarization. A major advantage of this technique is that it can measure a larger number of elements simultaneously. In combination with electrochemical or QCM experiments it can help to elucidate ambiguous results. Particularly the equipment used in this work was already successfully applied to the investigation of the anodic dissolution of stainless steel by Ogle [76].

The quartz crystal microbalance (QCM) is a very sensitive gravimetric method. It permits to follow mass changes during the treatment of a metal surface on the nanogram scale. A huge amount of electrochemically related studies were carried out with the QCM. For example, the passivation of Fe-Cr alloys was studied with the QCM by Schmutz & Landolt [77], Seo et al. [78] investigated the corrosion of thin iron films and inhibitors for iron and copper corrosion were examined by Telegdi et al [79] to cite some works related to steel and corrosion. The kinetics of the phosphating reaction was already investigated in the studies of Ogle [80] and Wolpers et al. [81].

As stand alone experiment the QCM is limited to the fact, that only a measurement of the total mass change can be performed, without the possibility to distinguish mass loss and mass gain at the same time. Most surface treatments involve simultaneous dissolution and precipitation. Further, the nature of the surface film formed during the treatment may be incompatible with the assumptions of the Sauerbrey equation relating frequency to mass. To this end, when combined with the **ICP-flow** analysis, ambiguous mass transients can easily interpreted with the additional information of the measured dissolution rate and the frequency-mass relationship can be confirmed, when the mass change is only determined by metal dissolution. The joint use of ICP-AES and QCM was employed for the investigation of the chromatation reaction [82]. A real combination of the QCM and the **ICP** technique was done for anodic polarisation studies on zinc [83].

## 4 EXPERIMENTAL SECTION

For the study of the chemical stability of phosphate layers (results see chapter 5) technical samples were prepared on a laboratory scale for investigation with in situ Raman spectroscopy and ICP-AES. Raman spectroscopy was only applied to the investigation of alkaline stability of the phosphate layers produced on technical **substrates**, whereas ICP-AES was both used for these experiments and for kinetic investigations, which were additionally conducted with the QCM.

### 4.1 METAL SUBSTRATES

The metal substrate primarily used in this work was electrogalvanised sheet steel produced by Voestalpine, typical of the quality used in the automotive industry. The total sheet thickness was 1.0 mm with a 7.5  $\mu\text{m}$  zinc coating electrodeposited by a sulphate electrolyte process. Cold rolled steel samples used in this work were also 1.0 mm thick and typical of the products used in the automotive industry. The phosphate layers were synthesised directly onto these surfaces in an as received condition, as described in the following section.

### 4.2 SYNTHESIS OF PHOSPHATE LAYERS

The laboratory phosphate layer synthesis consisted of three different steps - alkaline degreasing, activation and phosphating. Standard commercial products were used for the degreasing and activation steps. Degreasing was carried out in a spray chamber with an aqueous solution of 10 g/l **Ridoline™ 1372** (Henkel KGaA) at 40 °C for **15 s**. In order to examine the role of the metal cations four different phosphating solutions were prepared using analytical grade chemicals (Merck). Table 1 shows the composition of the bathes, the free acid [1] was adjusted to 2 in the case of electrogalvanised samples by adding sodium carbonate. The activation products Fixodine 50CF and Fixodine 950 (trademarks by Henkel) were used in varying concentrations to get comparable coating

weights of appr. 2  $\text{g/m}^2$ , which was found high enough to carry out the in-situ Raman experiments. As mentioned in the introduction (chapter 2.4.2), manganese and nickel refine the crystal size and hence decrease the coating weight. So in presence of these cations an activation product leading to a higher coating weight was applied.

SOLUTION	$\text{H}_3\text{PO}_4$ (85%)	ZnO [g/l]	NaF [g/l]	$\text{Mn}(\text{NO})_3 \cdot 4\text{H}_2\text{O}$ [g/l]	$\text{Ni}(\text{NO})_3 \cdot 6\text{H}_2\text{O}$ [g/l]	$\text{NaNO}_3$ [g/l]	Activation product
<i>Zinc coated steel</i>							
<i>Monocation Zn</i>	11	1.25	0.8	-	-	12	Fixodine 50CF (5g/l)
<i>Bication Zn/Mn</i>	11	1.25	0.8	4.6	-	8.9	Fixodine 950 (5g/l)
<i>Bication Zn/Ni</i>	11	1.25	0.8	-	5	9	Fixodine 950 (5g/l)
<i>Trication Zn/Mn/Ni</i>	11	1.25	0.8	4.6	5	6	Fixodine 950 (1g/l)
<i>Cold rolled steel</i>	$\text{H}_3\text{PO}_4$ (85%)	ZnO [g/l]	NaF [g/l]	$\text{MnCO}_3$ [g/l]	$\text{NiCO}_3$ [g/l]	$\text{NH}_2\text{OH}$ [g/l]	
<i>Monocation Zn</i>	11	1.25	2.5	-	-	1.5	Fixodine 50CF (1g/l)
<i>Trication Zn/Mn/Ni</i>	11	1.25	2.5	2	2	1.5	Fixodine 50CF (1g/l)

Table 1: Composition of the phosphating bathes used on zinc coated steel and cold rolled steel and type of activation used for the treatment.

The activation itself was carried out by dipping samples of 10x20 cm in size into a well stirred and freshly prepared solution of the activation product for 10 s at room temperature. Then the samples were immediately transferred to a laboratory scale spray chamber, where the phosphating was done at 55 °C for 25 s. After the reaction the sample sheets were rinsed with water, dried in a hot air stream and stored in a desiccator.

The bathes used for zinc coated steel do not work on cold rolled steel for steel would be simply passivated by the high amount of nitrate and the indispensable pickling reaction will not occur to the required extent. The lower part of Table 1 gives the bath formulation for the synthesis of phosphate layers on cold rolled steel samples.

In the treatment of cold rolled steel, the free acid was adjusted to 1.0, hydroxylamine ( $\text{NH}_2\text{OH}$ ) was used in place of the  $\text{NO}_3^-$  as an accelerator,  $\text{Mn}^{2+}$  and  $\text{Ni}^{2+}$  were added as carbonates and the F<sup>-</sup> concentration was 1.5 g/l. Degreasing was carried out as described above. Activation was performed by dipping the sample into a 1 g/l Fixodine 50CF solution for 10 s at room temperature. Phosphating was performed by spraying for 30 s at 50°C, similar to the zinc coated samples.



#### 4.2.1 POST TREATMENT OF PHOSPHATE LAYERS

To test the efficiency of post treatment for phosphate layers the following samples were prepared for investigation with Raman spectroscopy and **ICP-AES**. A monocation Zn solution was used (weakest alkaline stability - see results chapter 5) to obtain better distinguishable results about the influence of the post treatment. Samples were prepared with the usual conditions (see above). Table 2 lists the used post treatment, one of which is commercially available.

VARIANT	DESCRIPTION	REMARKS
Deoxylyte 54NC	pH=4	containing Zr, product by Henkel
Chromate post rinse	10g/l CrO <sub>3</sub> , pH=4	self-made

Table 2: Variants of post treatment

The **pH-value** of the solutions was adjusted with NaOH. All samples were prepared by dipping into the solution for 30 s at 30°C, then rinsing with deionised water and drying in a hot air stream.

#### 4.3 ANALYSIS AND SEM MICROGRAPHS

The analysis of the phosphate layers was conducted on 10x10 cm sample sheets by dissolving the layer in a 5 % CrO<sub>3</sub> aqueous solution at room temperature in case of zinc coated steel and at 70 °C in case of cold rolled steel. Wet chemical analysis of the solution was done with atomic emission spectroscopy and standard photometric techniques. The coating weight was determined by weight loss measurements.

SEM (scanning electron microscope) pictures and EDX analysis were made on a LEO 1530 field emission electron microscope.

## 4.4 PAINTING AND CORROSION TESTS

Standard corrosion tests were carried out on painted and phosphated samples. Painting was done by cathodic electrodeposition of an industrial lead-free ED-paint. The duration of deposition time was 2 min, curing was done at 180 °C for 25 min. The coating thickness of the paint was 25 µm. The painted samples (10x15 cm in size) were then artificially damaged by a cut (5 cm length). Principally there are two types of cuts for corrosion tests. The Van Laar cut only damages the paint layer and exposes the zinc and the Clemen cut also scratches through the zinc and exposes the steel underneath.

The damaged samples were exposed to standard corrosion tests like the salt spray environment. The spray solution consists of 5 % NaCl at 35 °C according to DIN 50021SS. The second test was the VDA-scab corrosion test (VDA 621-145, 10 weeks). Damaging on samples for this test was not only done by a scratch, but also by stone chipping (VDA 621-427) prior and after the exposure. After the exposure and rinsing of the residual salt the delaminated paint in the scratch region was removed with a sharp knife. Since the delamination is typically not uniform, the width was measured in a distance of every 5 mm and the average value was taken. On the stone chipped area the sample is rated from 0 (0 % paint removed) to 10 (100 % paint removed) by comparing with standard pictures.

## 4.5 ELECTROCHEMICAL EXPERIMENTS

### ***Open circuit potential during phosphating***

The open circuit potential (OCP) during phosphating was measured in a small electrochemical laboratory cell, in which the electrolyte could be heated thermostatically by a water bath. The OCP was measured versus an Hg/HgSO<sub>4</sub>-electrode (0.699 V vs. NHE) modified with phosphoric acid, which was prepared for the purpose of these experiments for long time exposure in hot phosphating solutions. Small strips of technical samples (2x10 cm) were used. The edges were painted with a clear coat in order to rule out electrochemical activity of the bare steel exposed.

### **Cyclic Voltammetry**

Cyclic voltammetry was carried out in an electrochemical flat cell with vertical mounting of the sample. Experiments were conducted at ambient temperature in a stagnant electrolyte (0.3 M boric acid at pH 9.0). The surface of the exposed sample part was 1 cm<sup>2</sup>. The detailed experimental conditions are described in the results section (chapter 6.2).

## 4.6 RAMAN SPECTROSCOPY

A block diagram of the Raman spectroscopy system is shown in Figure 14. The Raman spectrometer will be used to measure the composition of the conversion layer during chemical attack. Surface compounds can be characterised very well by Raman spectroscopy and the water of the electrolyte does not disturb the measurement.

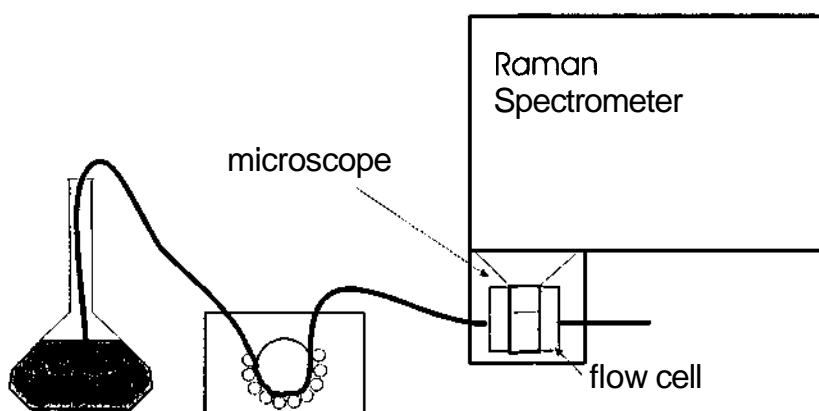


Figure 14: Block diagram of the in situ Raman experiments

All Raman data were obtained with a Dilor "LabRAM" confocal Raman microscope with a He-Ne laser excitation at 633 nm. This spectrometer allowed together with its CCD-detector and an 1800/mm grating to collect spectra in a range of appr. 1000 units in wave number (cm<sup>-1</sup>) simultaneously at a resolving power of 0.9 cm<sup>-1</sup>. The laser power incident on the sample surface was ~2.4 mW. For the in-situ measurements in the flow cell a 50x objective (Olympus) with a numerical aperture (NA) of 0.5 and a working distance of 8 mm was used. The confocal pinhole diameter was 1000 μm, and the slit width was adjusted to 400 μm.

The flow cell was mounted on the motorised x-y table of the Raman microscope. Focusing of the laser light was done by moving the table mechanically in the z-direction. The electrolyte (0.1 M NaOH, deaerated with  $N_2$ ) was pumped through the cell with a peristaltic pump at a rate of 10 ml/min.

A simple flow cell for easy use of technical samples was constructed from Teflon as illustrated in Figure 15. The upper part of the cell accomplishes the electrolyte flow and is provided with the cell window. This part is mounted with screws onto the lower part, where the sample is fixed. Samples up to 5x5 cm in size can be used with this cell. However, turbulent flow conditions at the inlet into the sample compartment lead to non uniform attack of the surface, which may influence the open circuit potential by quicker dissolution of the layer and earlier exposing of the substrate metal. For the work described here small samples of 2.5x2.5 cm size were mounted into the flow cell with a special adhesive tape leaving free a circular area with 2 cm diameter on the sample exposed to the electrolyte. Pickling experiments with dilute hydrochloric on zinc coated steel acid exhibited a uniform dissolution on the sample surface exposed to the electrolyte (area:  $3.14 \pm 0.08 \text{ cm}^2$ ).

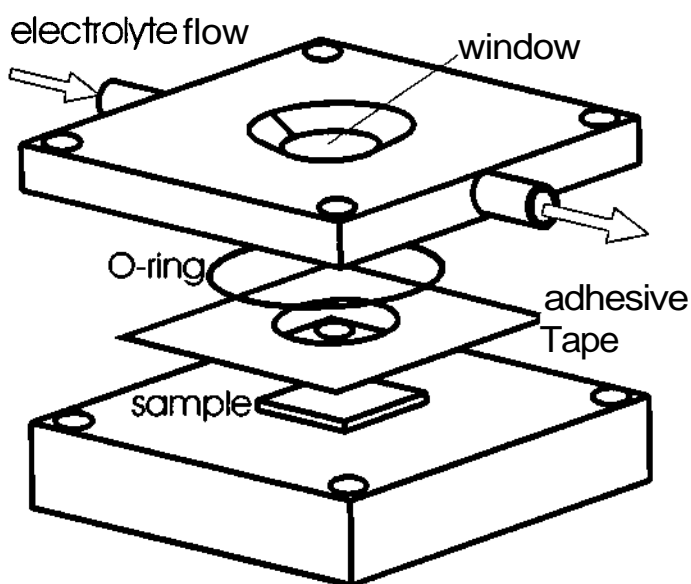


Figure 15: Drawing of the flow cell used for in-situ Raman spectroscopy on technical samples

The diameter of the circular sample compartment was 4 cm giving a volume of appr. 1.8 ml with the sample mounted in the cell. The thickness of the electrolyte layer above the sample surface was 1 mm. Under those conditions the velocity of the solution

was 20 cm/min in the centre of the cell at a turnover time of around 11 s in the whole compartment at a flow rate of 10 ml/min. The centre of the sample compartment is covered with a 1 mm thick window made of flat glass giving a transparent area of 20 mm in diameter.

A capillary introduced into the cell via a small hole in the side of the upper part allowed the measurement of the open circuit potential (OCP) versus an **Ag/AgCl-electrode** (0.197 V vs. NHE) during the reaction. The electric contact to the sample was accomplished by inserting a small copper wire under the **sample**, which is connected to the potentiostat.

For in-situ experiments a suitable sample spot was adjusted in the dry state of the cell to be sure the chosen spot exhibited no fluorescence, which would render the detection of the Raman spectra impossible. With the electrolyte in the cell, a new adjustment of the laser focus had to be done due to the high refraction of the laser light at the phase boundaries air-glass and glass-electrolyte [84]. Subsequent spectra could be recorded with the spectrometer software. For in situ experiments on phosphate layers a collection time of 45 s was chosen, which was found to yield reasonable intensities of the Raman signal for further quantification.

## 4.7 ICP-AES

### 4.7.1 SPECTROMETER DETAILS

A simplified block diagram of the atomic emission spectroelectrochemistry system is shown in Figure 16. The diagram is not to scale.

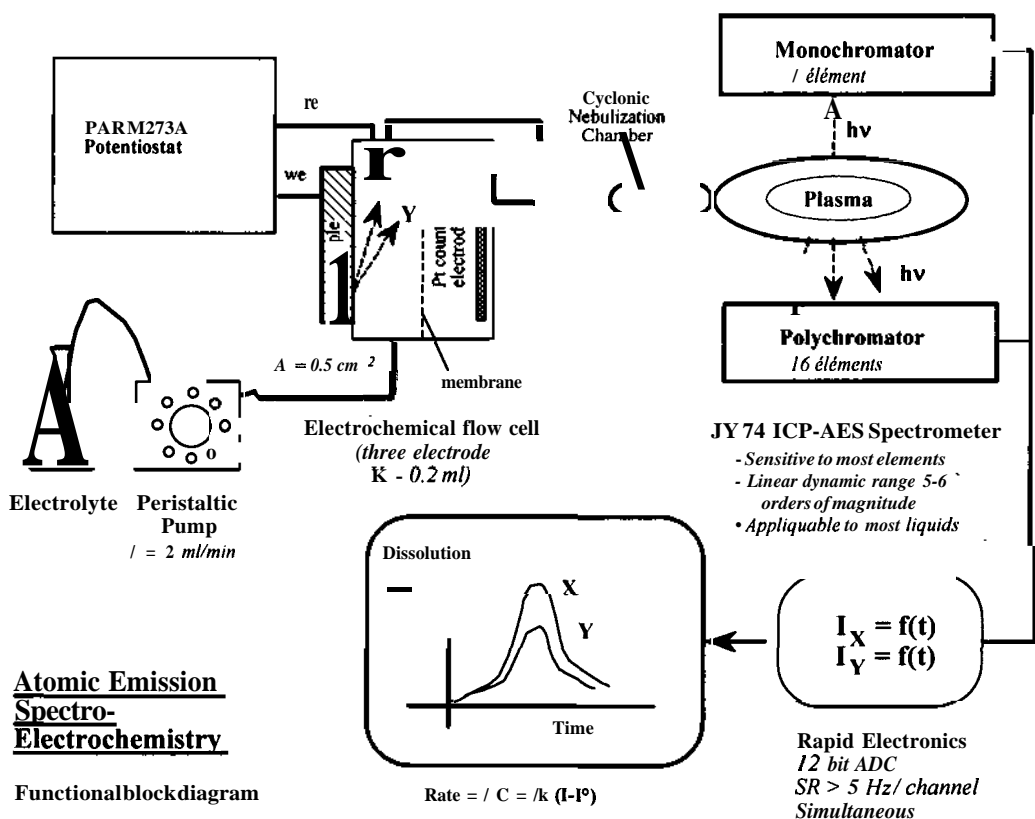


Figure 16: Schematic view of the ICP system

The ICP spectrometer is used to measure the composition of the electrolyte downstream from the dissolution cell permitting a qualitative identification of the soluble reaction products and a quantitative determination of the simultaneous dissolution rates of the products. A commercial ICP atomic emission spectrometer from Jobin Yvon, Inc (JY 74) was used in this work. The plasma source consists of a 40 MHz, 1 kW inductively coupled Ar plasma, into which the electrolyte sample is continuously aspirated. The spectrometer consists of a polychromator for the simultaneous detection of 17

predetermined elements, and a monochromator for the detection of an additional element of choice. A cyclonic aspiration chamber, chosen for its rapid response time, and a concentric glass nebuliser, chosen for its good performance with electrolytes of high salt **concentration**, were used in this work.

The major modules of the spectrometer, which the sample runs through, are: (1) the nebulisation / aspiration system into which the liquid sample is transformed into a fog of very small droplets, a fraction of which are aspirated into the (2) inductively coupled plasma. The high temperature of the plasma ( $\approx 8000$  K) leads to a rapid desolvation of dissolved species, which are usually reduced to the atomic state. The spectral emission of the resulting atoms in the plasma then passes into (3) the optical detection system consisting of (a) a polychromator with an array of photomultipliers preset for a specific wavelength, and (b) a monochromator with a single photomultiplier for an adjustable wavelength. The signal produced by the photomultipliers is monitored as a function of time.

The commercial spectrometer was modified for the purposes of this work by the addition of a rapid data acquisition system, which monitors the entire array of photomultipliers and displays the signals in real time, and permits software control of the photomultiplier voltage. With this system, the photomultiplier voltages are sampled at a rate of 0.1 kHz with a 12 bit **A/D** converter, and the results are averaged over an arbitrary integration period, which in this work, was normally 0.5 s or 1 s.

## 4.7.2 FLOW CELL

A two compartment, three electrode flow cell was constructed from Teflon as illustrated in Figure 17. The cell was patented in 1992 [85]. The surface of the working electrode ( $0.52 \text{ cm}^2$ ) is in contact with the flowing electrolyte (2 - 12 ml/min) in a small volume compartment ( $\ll 0.2 \text{ ml}$ ), separated from a counter electrode compartment by a porous membrane allowing passage of ionic currents while preventing bulk mixing of the two electrolytes. For the work described here, a usual reference electrode was placed in the counter electrode compartment.

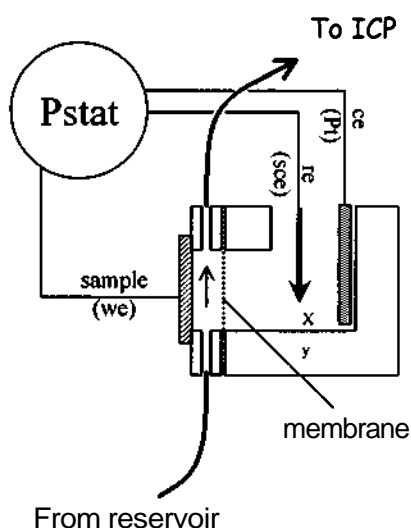


Figure 17: Schematic picture of flow cell for ICP experiments

The geometrical surface area exposed to the electrolyte was measured by dissolving a 5  $\mu\text{m}$  zinc coating from an electrogalvanised steel sample and measuring the area of the exposed steel. The value was found to be  $0.53 \pm 0.02 \text{ cm}^2$ .

A hollow copper plaque could be pressed onto the backside of the sample. Temperature control was performed by circulating water from a thermostatically controlled water bath through this plaque. Exact calibration measurements as described by Ogle [76] have shown, that approximately  $5 \text{ }^\circ\text{C}$  to  $6 \text{ }^\circ\text{C}$  are lost in the cell. This is the difference between the temperature of the water bath and the actual temperature of the sample.

An EG&G PAR273A potentiostat, programmed from the front panel was used for control of all electrochemical experiments. The analog signals from the potentiostat were



recorded with the same data acquisition card and software as used for the ICP. In this way the potential and current of the potentiostat were monitored simultaneously with the ICP-signals. This insures that the spectroscopic and electrochemical data are on the same time scale.

#### 4.7.3 RELATIONSHIP BETWEEN RATE AND INTENSITY

The calibration procedure was exactly described in a previous publication [76]. The basic principle of analytical ICP atomic emission spectrometry is that the emission intensity ( $I_\lambda$ ) of a given element, **M**, in the plasma at a wavelength  $X$  specific to **M**, is proportional to the concentration of that element ( $C_M$ ) in the electrolyte stream. Assuming that only the element **M** emits radiation at wavelength,  $X$ , the standard quantitative relationship is :

$$C_M = k (I_\lambda - I_\lambda^\circ) \quad 4-1$$

where  $k$  is the constant of proportionality and  $I_\lambda^\circ$  is the background intensity. Note that the concentration  $C$ , will be expressed in  $\mu\text{g}/\text{cm}^3$  (or ppm) as is customary in analytical applications of ICP spectroscopy. With appropriate choice of  $X$  this proportionality is normally valid over four to six orders of magnitude, limited at low concentrations by the fluctuations of  $I_\lambda^\circ$  due to background emission from the plasma and scattered radiation, and at high concentrations by self-absorption [86]. At intermediate concentrations, where  $I_\lambda \gg I_\lambda^\circ$ , the noise level is determined by fluctuations in the nebulisation system and is a constant percentage of the analytical signal.

Under steady state conditions, the elemental dissolution rate of component **M** of the sample working electrode within the flow cell, ( $R_M(t)$  expressed in  $\mu\text{g}/\text{s}$ ), is equal to its concentration downstream from the cell multiplied by the flow rate of the electrolyte ( $f$  expressed in  $\text{cm}^3/\text{s}$ ).

$$R_M(t) = f C_M(t) = k f (I_\lambda(t) - I_\lambda^\circ) \quad 4-2$$

#### 4.7.4 EXPERIMENTAL PROCEDURE

The elemental concentration of P, Zn, Mn, and Ni was determined from the emission intensity at 178.225 nm (P), 213.856 nm (Zn), 257.610 nm (Mn), 216.555 nm (Ni). In addition, Fe, Al, and Ti were followed but not detected in these experiments unless otherwise noted. The open circuit potential of the phosphated sample was measured relative to a saturated calomel electrode (0.2418 V vs. SHE) placed in the external compartment of the cell as shown in Figure 17. This compartment was separated from the main cell by a porous membrane that allows passage of ionic currents, but no bulk mixing of the two electrolytes.

##### ***Chemical stability of phosphate layers in 0.1 M NaOH***

The experiments were performed with a flow rate of 2.5 ml/min. Two types of leaching experiments were performed in this study. First, the reactivity of the phosphate layer with a 0.1 M NaOH solution was measured. The exposure to the alkaline solution continued until phosphate and zinc leaching had decreased to undetectable levels. Following the alkaline exposure, the surface was exposed to 0.01 M HCl so as to dissolve any residual species from the phosphate layer. This acidic treatment also attacked the zinc substrate.

Initially the sample was placed into the empty cell, with the 0.1 M NaOH electrolyte flow bypassing the cell. This permits a precise measurement of background emission signal for the electrolyte. To begin the exposure the valves were adjusted so that the electrolyte flow passed through the cell. Next, the alkaline solution was substituted for deionised water to remove any NaOH from the cell compartment and the tubes to the spectrometer. After this 0.01 M HCl was pumped through the cell to dissolve the residuals of the layer and detect remaining species. At the end of the experiment, the valves were returned to the bypass position so as to measure the background signal and the emission intensity of one or more standard solutions. Calibration of the emission intensity during the exposure was performed by comparison with the emission intensity of a standard solution, usually 5 ppm of the element in question.

### ***Anodic dissolution of zinc (combined with QCM)***

These experiments were done in combination with the QCM. Only Zn dissolution in phosphoric acid with oxidising agents (detailed composition in the results section chapter 6.4) was detected with the spectrometer. The flow rate was adjusted to 2.5 ml/min. Calibration was done in the solution of interest containing zinc at 5 ppm like in the alkaline stability experiments.

## **4.8 QCM**

For this studies the QCA 922 (quartz crystal analyser) of Princeton Applied Research was used as oscillatory device. The 9 MHz quartz crystal electrodes were purchased from PAR (see Figure 18). They consisted of a quartz wafer with a  $0.196 \text{ cm}^2$  Pt electrode on each side. Electric contact was accomplished with leads of stainless steel, which were fixed to the Pt layer by small helical springs.

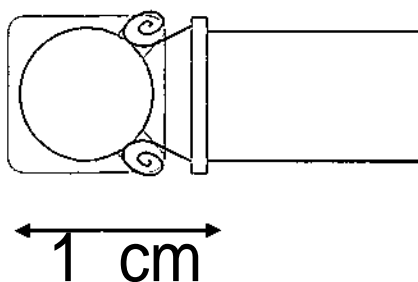


Figure 18: Picture of a quartz electrode. Pt layer (grey area)

On the **Pt-layer** zinc was electrodeposited under the conditions stated in Table 3. Before deposition the **quartzes** were rinsed in deionised water, ethanole and dried under an Ar stream. To reuse the quartz the zinc layer could be removed with dilute **HNO<sub>3</sub>** and coated again.

Electrolyte	Current	time	calculated thickness
1.6 mol/l ZnCl <sub>2</sub> 4.5 mol/l KCl	100 mA	16 s	4 pm

Table 3: Conditions for electro-deposition of Zn on the platinum coated quartzes for the QCM.

Three different types of experiments were carried out with the QCM. As a stand alone experiment the QCM was used to follow mass changes during the phosphating. Combined with **ICP-AES** the anodic dissolution of the zinc layer was measured in solution with different accelerating agents. The alkaline stability of phosphate layers on the zinc coated quartzes was determined by the combination of the QCM (mass changes) and the ICP-AES (analysis of downstream solution).

For the phosphating kinetics and the accelerator experiments in combination with the ICP-AES the zinc coated quartzes were used as received after deposition and a deionised water rinse. To carry out the leaching experiments the zinc layer on the quartzes was phosphated in the same way as the technical samples by simply dipping into the bathes as described in 4.2 p. 33.

The principal experimental setup is shown in Figure 19, with a detailed picture of the used flow cell. The electrolyte was pumped using a peristaltic pump at flow rates from **2-4 ml/min**. For the connection to the **ICP**, this flow cell was used instead of the one for technical samples and built into the ICP setup. Unlike in the cell for technical samples, the **QCM-cell** does not allow exact temperature control **anymore**, so the experiments were conducted at room temperature, when combined to the ICP.

The cell itself (Figure 19b) consists of two compartments, which are divided by a conductive membrane. The electrolyte only flows through the quartz compartment with exposure of one side of the quartz plate to the electrolyte. O-rings on both sides provide leak proof conditions. The compartment with the reference and the counter electrode contains the same electrolyte. Calculation of the **surface** mass from the frequency data

was easily done by using the Sauerbrey-equation (Eq. 3-1) and the theoretical value for the mass sensitivity of the quartzes used in this work ( $17.98 \times 10^7 \text{ Hz cm}^2 \cdot \text{g}^{-1}$ ).

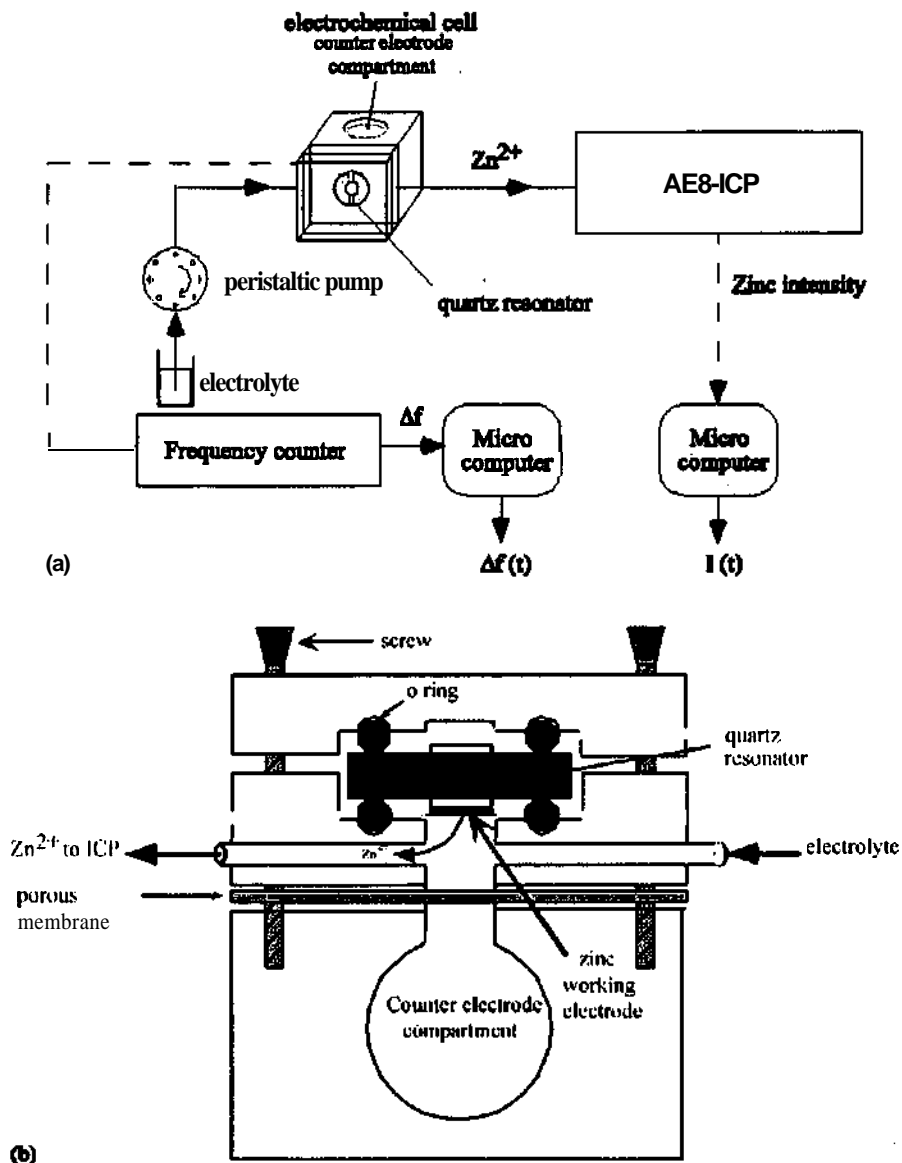


Figure 19: Schematic diagram of the coupled QCM and ICP-AES experiment and drawing of the flow cell for the quartz crystal microbalance.

## 4.9 CALIBRATION OF RESIDENCE TIME IN ICP EXPERIMENTS

In the ICP experiments the electrolyte requires a certain time, when it flows from the cell, where the reaction of interest takes place to the detection unit. During this time mixing of the electrolyte and distribution of the species to be analysed may happen. For exact time profiles this time lag must be determined in separate experiments. In this work the transient of copper dissolution in hydrochloric acid after an anodic pulse was taken to determine this parameter.

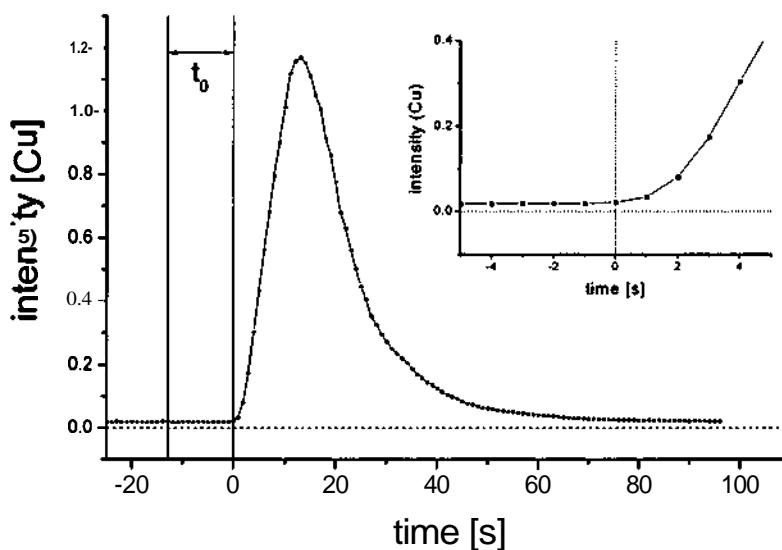


Figure 20: Intensity transients of Cu dissolution after anodic pulse of 1 mA for 1 s. Lag time to can be seen.

Figure 20 shows the experiment for the combination of the QCM and the ICP on a copper coated quartz. The same experiment was conducted with the setup for technical samples. Lag time was 11 s for ICP only and 13 s for the combined setup. With the knowledge of this time period it is possible to bring the OC potential transients, which are obtained instantaneously, and the leaching transients on the same time scale. This offset will be considered in the presentation of all ICP data in this work.

The transients of the pulse experiment all show a course, which follows the log normal distribution (Gaussian curve with a logarithmic x-axis). This curve is typical for this type of flow experiments [76] and can be explained by the distribution of the ions due to diffusion in the tube from the cell to the ICP.

## 5 ALKALINE STABILITY OF PHOSPHATE LAYERS

### 5.1 BACKGROUND

As already pointed out in chapter 2.6 phosphate layers are exposed to a highly alkaline environment during under paint corrosion. The reactivity at the metal/paint **interface** with an alkaline medium is therefore an important property of a conversion layer. It is generally accepted that the composition of the phosphate layer has a strong influence on its chemical stability. For zinc, secondary elements such as  $\text{Ni}^{2+}$  and  $\text{Mn}^{2+}$  are used to increase the alkaline stability. The only phase formed on the zinc **surface** is **hopeite**, whereas on steel the primary phase is **phosphophyllite**, which contains Fe. It has been shown to be more resistive than hopeite containing only  $\text{Zn}^{2+}$ . Nevertheless, there are few published fundamental studies concerning the alkaline stability of the phosphate layer. This may be partly explained by the fact that rate measurements for this type of process are particularly difficult. The reaction is not electrochemical in nature so that neither current nor potential can be used as reliable measures of the extent of reaction. Further, gravimetric techniques are ambiguous because weight losses and **weight** gains occur simultaneously during the reaction. Therefore, there is a clear interest in applying more sophisticated techniques of in-situ analysis to this problem.

### 5.2 ANALYSIS AND MORPHOLOGY OF THE LAYERS

Table 4 gives the chemical and gravimetric analysis of the phosphate conversion layers on zinc coated steel and cold rolled steel. The analysis was performed by etching the phosphate coating with a 5%  $\text{CrO}_3$  solution for 5 min (zinc coated steel at room temperature and cold rolled steel at 70°C). The phosphate coating weight was determined by the mass loss during this etching period. The elemental composition of the layers was determined by analysis of the etch solutions with **ICP atomic emission spectrometry** and photometry using standard techniques. X-ray diffraction revealed only hopeite for all layers on zinc coated steel as expected for this type of sample. On cold rolled steel, hopeite and phosphophyllite were detected.

SAMPLE TYPE	PHOSPHATE LAYER ANALYSIS					
	Coating weight [g/m <sup>2</sup> ]	Zn	Mn	Ni		Phosphate
Electrogalvanised steel	Coating weight [g/m <sup>2</sup> ]	Zn	Mn	Ni		Phosphate
<i>Monocation Zn</i>	2.09	43.1	-	-	-	42.1
<i>Bication Zn/Mn</i>	2.13	38.0	5.2		-	41.8
<i>Bication Zn/Ni</i>	2.29	42.6	-	1.7	-	42.1
<i>Trication Zn/Mn/Ni</i>	2.02	39.1	4.7	1.1	-	37.7
Cold rolled steel	Coating weight [g/m <sup>2</sup> ]	Zn	Mn	Ni	Fe	Phosphate
<i>Monocation Zn</i>	2.98	38.3	-	-	4.9	41.2
<i>Trication Zn/Mn/Ni</i>	1.48	34.5	6.1	1.1	2.7	42.1

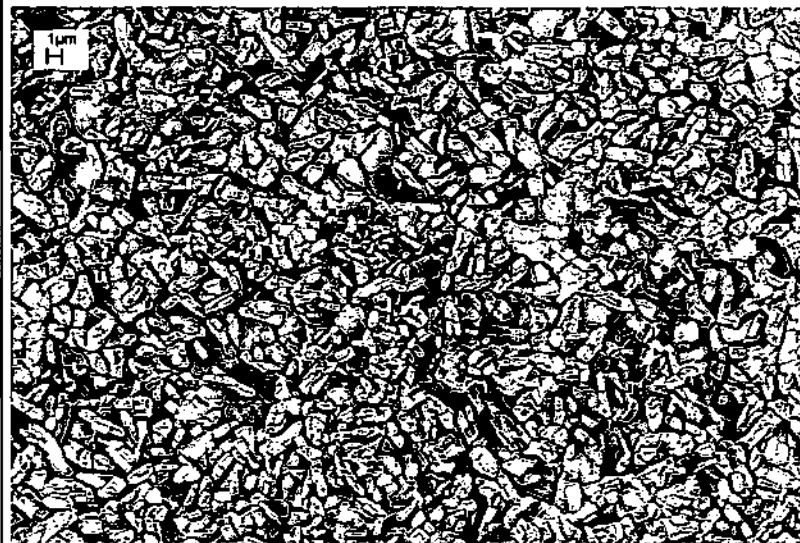
Table 4: Composition of the phosphate layers synthesized as described in chapter 4.2 p. 33.

By changing the product of activation it was possible to obtain similar coating weights on all layers, even if Mn and Ni are present, which would otherwise cause a decrease in coating weight (see chapter 2.4.2 p14). Mn was found in a concentration of 5 % in the **crystals**, Ni of 1.5 %. Figure 21 shows the obtained SEM-pictures of the four phosphate layers. A clear influence of Mn and Ni on crystal morphology was observed, indicated by the cubic habitus of the crystals in the Zn/Mn-phosphate layer and the plate shaped habitus in the **Zn/Ni-phosphate** layer. The habitus on the trication layer (Figure 21 D) can be interpreted as a mixture of the different influences of Mn and Ni on the morphology as seen on Figure 21 B and Figure 21 C. Average crystal size was around 2  $\mu\text{m}$  on all samples.

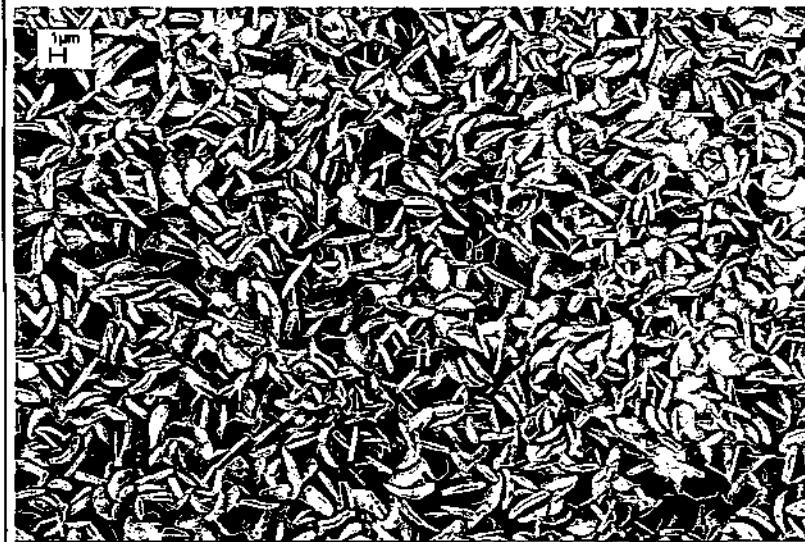




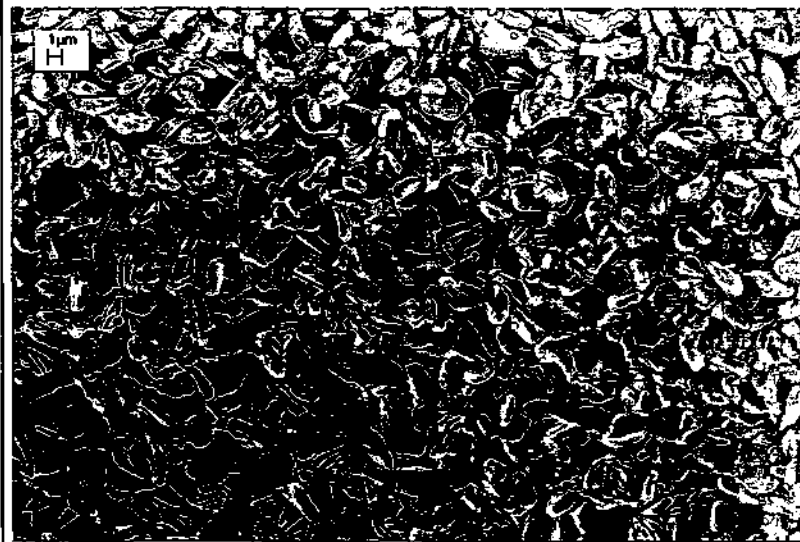
A - monocation Zn



B - bication Zn/Mn



C - bication Zn/Ni



D - trication Zn/Mn/Ni

Figure 21: SEM-pictures of the investigated phosphate layers as received.

These samples were used both for in situ Raman spectroscopy and for the ICP-AES. To look for changes in the morphology SEM-pictures and EDX analysis were also taken after the exposure to the alkaline media.

Figure 22 shows the SEM pictures of the samples after 225 s of attack by the electrolyte (0.1 M NaOH) in the Raman flow cell. Traces of attack can be seen on all samples, but no conclusion about the remaining phosphate concentration in the layer can be made by just investigating the morphology.

This is especially clear for the bication Zn/Ni sample (Figure 22C), which retained nearly the original crystal morphology after the attack, but showed a clear decrease in the P:Zn ratio (measured by EDX) compared to the unattacked surface. Table 5 shows the decrease of the P:Zn intensity ratio as measured by EDX on the attacked samples compared to the original layers. The values roughly reflect the alkaline stability of the samples as determined by ICP-AES and by Raman spectroscopy (see 5.4 and 5.5)

SAMPLETYPE	PERCENTUAL DECREASE OF P:ZN RATIO
<i>Monocation Zn</i>	92
<i>Bication Zn/Mn</i>	49
<i>Bication Zn/Ni</i>	82
<i>Trication Zn/Mn/Ni</i>	55

Table 5: Percental decrease of the P:Zn ratio on the attacked samples compared to the original layers. Values were calculated by integrating the EDX peaks using the Zn La line and the P Ka line.



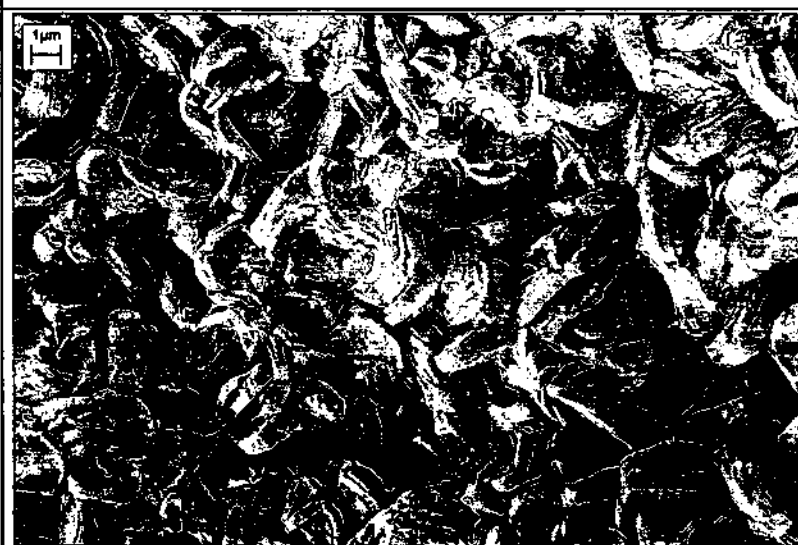
monocation Zn



bication Zn/Mn



bication Zn/Ni



trication Zn/Mn/Ni

Figure 22: SEM-pictures of the phosphate layers after 225 s attack of 0.1 M NaOH electrolyte in Raman flow cell. White spots are due to discharging effects, since samples were not gold coated.

## 5.3 CORROSION TESTINGS

### 5.3.1 SALT SPRAY TEST

Salt spray test was carried out on painted samples as an example to prove the alkaline attack of the phosphate layer during corrosion in a primarily neutral media. The zinc coated and phosphated samples (trication phosphating) were ED-painted and artificially damaged by a 5 cm Van Laar cut (see 4.4 p. 36). The sample was exposed in the salt spray chamber for 120 h. The spray solution consists of 5% NaCl at 35°C according to DIN 50021SS. After the exposure and rinsing of the residual salt the delaminated paint was removed with a sharp knife. The delamination was not uniform, but appeared in semicircles (blisters) with about 5 to 10 mm distance from each other. (Figure 23) This is typical for zinc-coated steel substrates. The scratch itself was covered with white corrosion products.

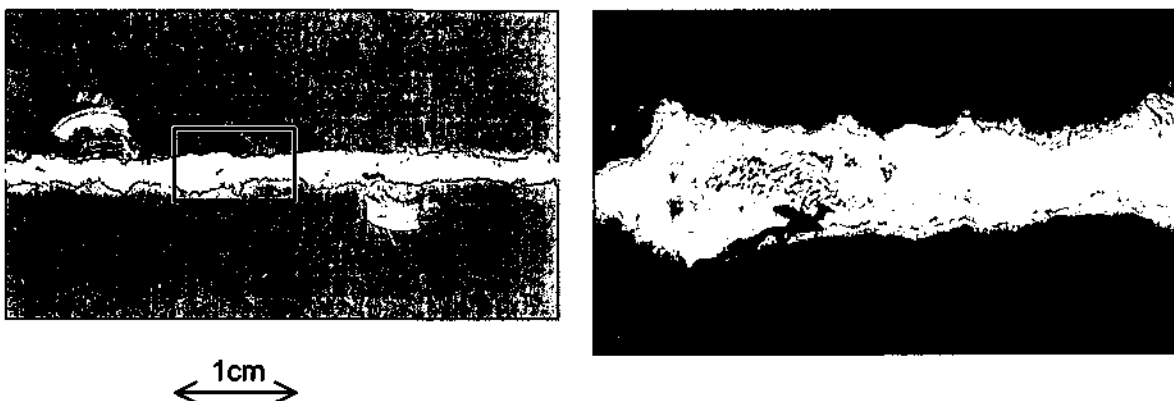


Figure 23: Part of the sample after the salt spray test. Two blisters with already removed paint can be seen. The scratch is totally covered with white zinc corrosion product. Enlarged view of area marked by black rectangle shown on the right side.

Two different regions could be seen on the scratch in various distances (5 to 20 mm) characterised as a clear white area and brown spots. Figure 23 shows a part of the **scratch**, where both regions can be seen. The according Raman spectra of these spots can be seen in Figure 24A and Figure 24B. The product on the brown coloured part shows peaks at 330, 437, 570 and a broad band at  $1100\text{ cm}^{-1}$ . This could be identified as ZnO [60]. The brownish colour of the spots is most probably caused by the presence of Mn in the phosphate layer. The spectrum of the white part shows peaks at 386, 738, 1070, 1370 and  $1550\text{ cm}^{-1}$ , typical bands for zinc hydroxycarbonate.

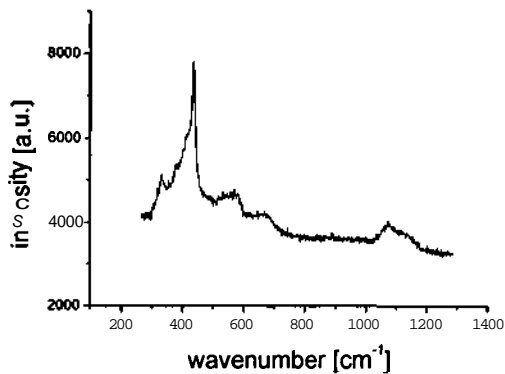


Figure 24A: Raman spectrum of the brown coloured part in the scratch region of painted sample after salt spray test. Identified as zinc oxide (ZnO).

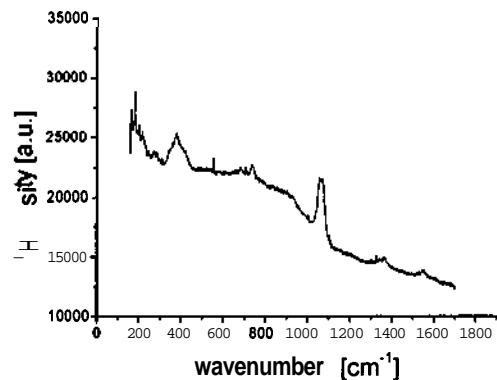


Figure 24B: Raman spectrum of the white coloured part. Identified as zinchydroxy carbonate ( $2\text{ZnCO}_3 \cdot 3\text{Zn}(\text{OH})_2$ )

Figure 25 shows SEM micrographs of the blister region after removing the paint. No typical phosphate crystals are visible, and the EDX-spectrum (Figure 26A) shows no phosphorus signal, but a distinct chlorine signal. The Raman spectrum (Figure 26B) shows peaks at 210, 250, 397, 731, 910, 3460 and at 3488  $\text{cm}^{-1}$  and was identified as the spectrum of  $4\text{Zn}(\text{OH})_2 \cdot \text{ZnCl}_2$ . This compound was found all over the blister. No trace of hopeite or phosphorus was detected.

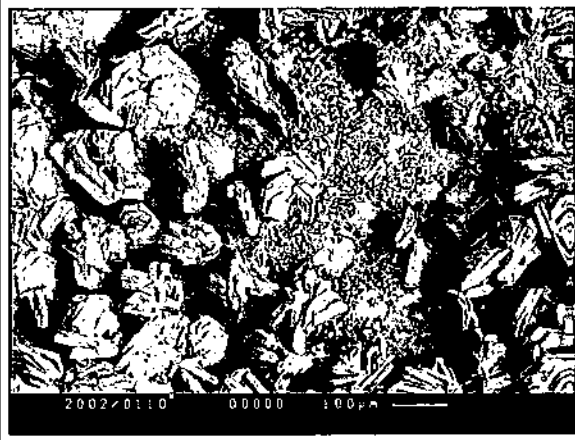
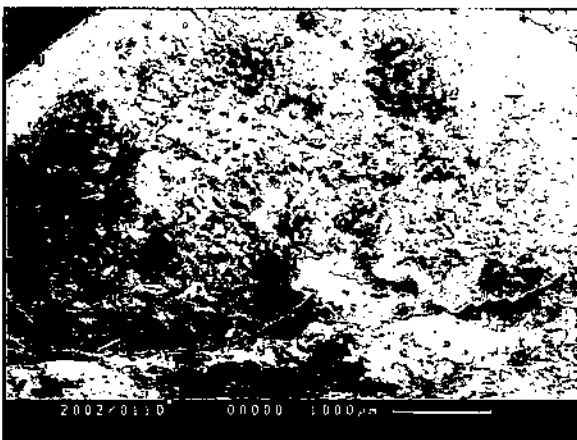


Figure 25: SEM picture of blister area. Enlargement of the region marked by black rectangle shown right.

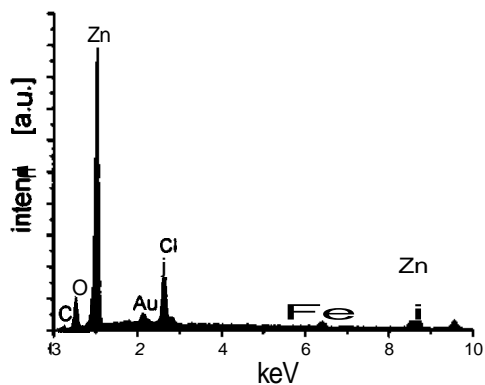


Figure 26A: EDX-spectrum of the crystals in the blister. Spectra are similar all over the delaminated area in the blister.

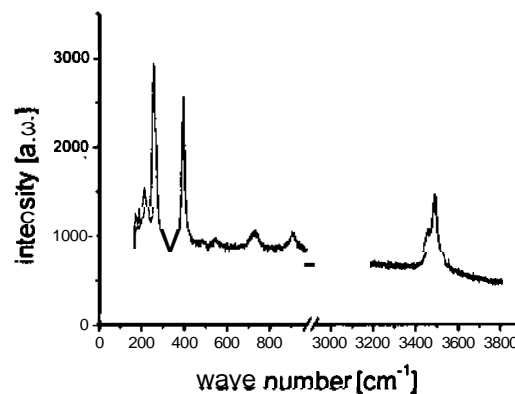


Figure 26B: Raman spectrum of corrosion products in the blister.  $4\text{Zn}(\text{OH})_2 \cdot \text{ZnCl}_2$  was found all over the delaminated area in the blister.

The paint, which was removed from the sample, was examined on the side faced to the substrate and phosphate layer respectively. Figure 27A and Figure 27B show two regions which could be visually distinguished. First we find again crystals, which were identified as  $4\text{Zn}(\text{OH})_2 \cdot \text{ZnCl}_2$  in the EDX (Figure 28B). These crystals were obviously removed from the sample during the cut with the knife and apparently stuck to the paint. Another part showed an EDX-spectrum (Figure 28A) with a clear phosphorus signal, but it does not show the typical crystal structure of hopeite crystals. Both spectra also show elements from the components of the paint (Ti and Si). No distinct signal was detected in the Raman spectra.

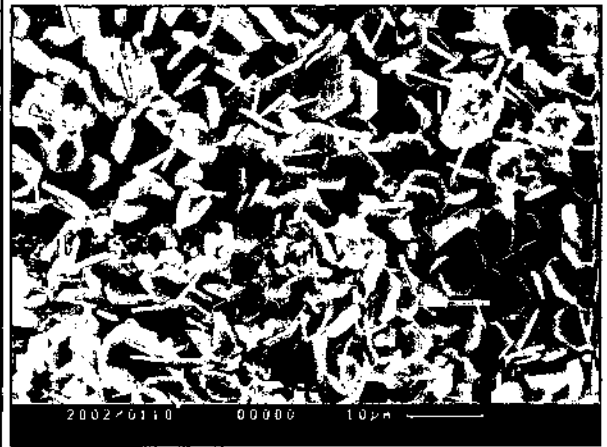
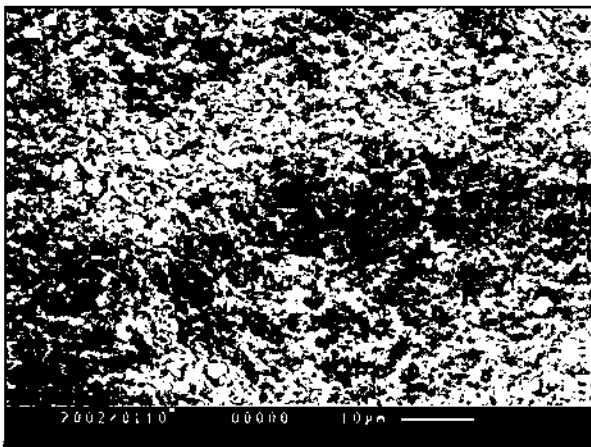
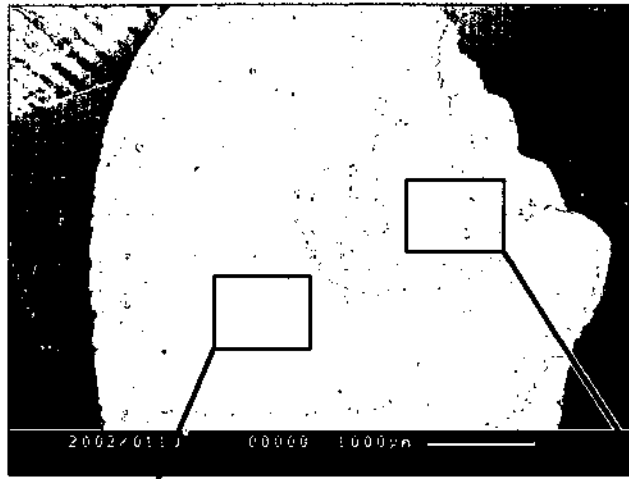


Figure 27A: Crystals visible on a certain part of the backside of the delaminated paint. For EDX spectrum see Figure 28A (phosphate present)

Figure 27B: Part of the backside indicated by black rectangle. For EDX spectrum see Figure 28 (zinc hydroxy chloride)

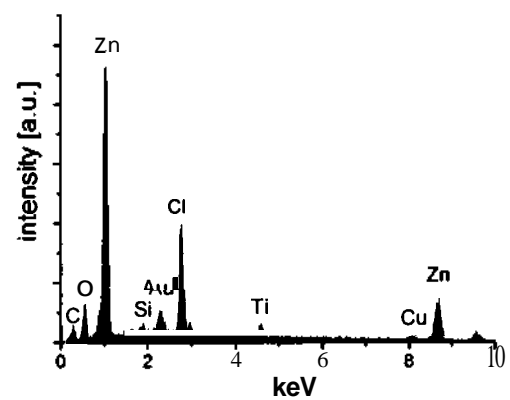
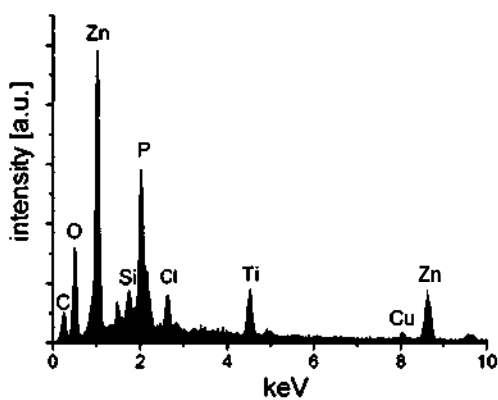


Figure 28A: Analysis of the backside (side of phosphate layer) of removed paint on a blister.

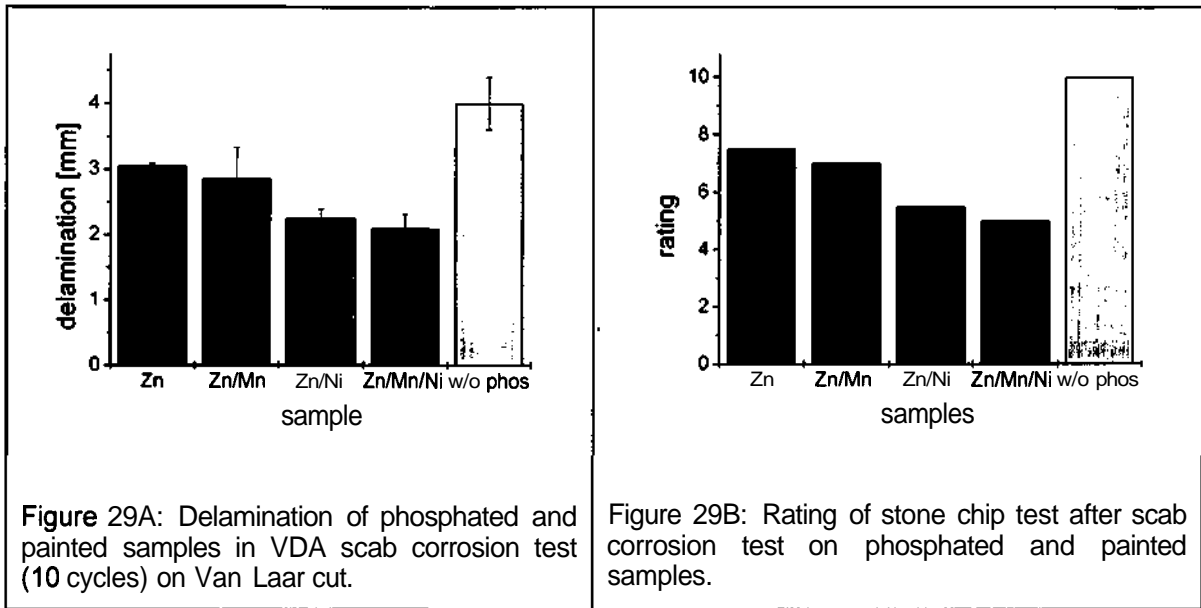
Figure 28B: Analysis of the backside of the removed paint on a blister (SEM picture Figure 27B)

The experiment shows that the phosphate layer is completely removed from the sample even in neutral corrosive media. The rising of the **pH-value** due to cathodic reduction of oxygen seems to be sufficient to dissolve the phosphate crystals and allow paint delamination. The essential delamination happens between the phosphate layer and the zinc substrate, which is confirmed by the phosphate remainders found on the backside of the removed paint. The scratch was covered with oxides, whereas the region under the paint blisters exhibited  $4\text{Zn}(\text{OH})_2 \cdot x\text{ZnCl}_2$ , the most common corrosion product in chloride-contaminated environment. However, this corrosion product is typical for anodic conditions [60] and is the stable modification in acidic environment. Nevertheless, the delamination starts at a small cathodic front, which runs ahead of the anodic region. In this cathodic area the highly alkaline environment causes partial dissolution of the phosphate crystals and therefore facilitates further delamination of the paint in the anodic process.

### 5.3.2 SCAB CORROSION TEST

Samples were painted with a lead-free ED-paint and tested according to VDA 621-145 in a scab corrosion test. Figure 29A shows delamination of Van Laar cut and Figure 29B shows the rating of the stone chipped area (VDA 621-427) after 10 cycles. The positive effect of a phosphate layer on the rate of under paint corrosion is clearly seen. The presence of nickel in the layer increases the corrosion resistance. Although the other experiments (see following section) show that Manganese raises the alkaline stability, its influence in this corrosion test is rather small. The covering of the free zinc pores in the phosphate layer by nickel deposition therefore seems to be the predominant factor in the performance of a phosphate layer in this type of long time corrosion test.





**Posttreated samples**

Compared to an untreated monocation Zn-phosphate sample, chromated and Deoxylyte 54 rinsed samples showed only a very slight decrease in the delamination width (-0.2 mm) after 10 weeks of VDA scab corrosion test. Due to the non-uniform delamination front and the difficulties in the evaluation of the corroded area this cannot be seen as a significant improvement. There is no clear effect in enhancing the corrosion resistance when a phosphated layer is rinsed with solutions for post-treatment. It has to be noted, that this was only shown for a scab corrosion test on painted samples. Results may be quite different in a test with constant humidity (like the salt spray test) or in non-painted condition. However, these tests are usually of no relevance in the field of application of phosphated metal products.

## 5.4 ICP-AES

### 5.4.1 GENERAL FEATURES OF THE LEACHING TRANSIENTS

Figure 30 shows typical leaching transients obtained when the trication phosphate layer is exposed to 0.1 M NaOH at ambient temperature in aerated (left) and  $O_2$ -free (right) solution. The rate of P and Zn leaching are shown as a function of time during the exposure to the aggressive electrolyte. Atomic emission spectroscopy only gives the elemental composition, but it can be assumed that the elements are dissolved in their common ionic states (P as  $PO_4^{3-}$ , Zn as  $Zn^{2+}$ ). The open circuit potential, E vs. SHE in the reference compartment is also shown. Contact with the electrolyte begins at the vertical dashed line (here positioned at  $t=0$ ). Prior to  $t=0$  the surface was dry in the empty cell and the pure electrolyte was aspirated into the plasma by a bypass tube.

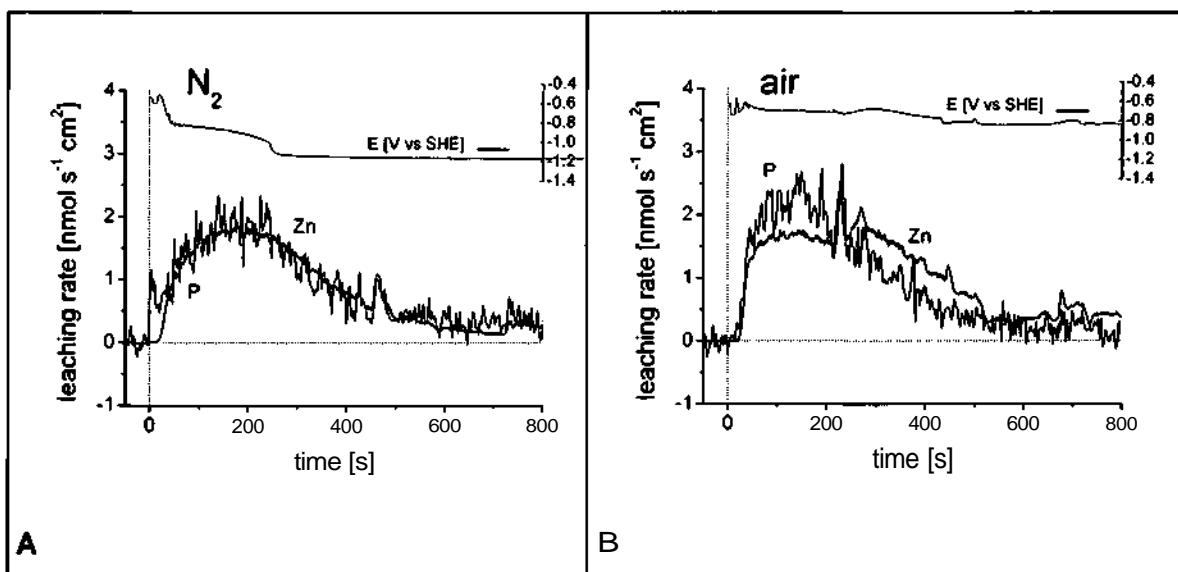


Figure 30: Leaching profile for a trication layer on electrogalvanized steel in 0.1 M NaOH at ambient temperature. (Right)  $N_2$ ; (Left) Air. Prior to  $t=0$  the flow cell was empty and the test electrolyte flowed through the cell bypass.

These results demonstrate that  $PO_4^{3-}$  and  $Zn^{2+}$  dissolution occur simultaneously during the early stages of the alkaline attack. After approximately 600 s, the  $PO_4^{3-}$  dissolution rate drops to undetectable levels while the  $Zn^{2+}$  dissolution rate drops down to a steady state value. The steady state zinc dissolution rate is significantly higher in aerated solution (Figure 30A) as compared to oxygen-free conditions (Figure 30B) and therefore is probably due to the corrosion of the Zn substrate.

The open circuit potential was measured simultaneously with the leaching rate transients and is shown on the secondary axis to the right. For all experiments in this work carried out in **O<sub>2</sub>-free solution**, the initial open circuit potential was around -0.65 V vs. SHE, and dropped off progressively during the exposure to the alkaline solution. During the early stages of this experiment, the potential drops off slowly until approximately -0.9 to -1.0 V vs. SHE is obtained. At that point, there is an abrupt drop in the potential to about -1.25 V vs. SHE, consistent with the **Zn/Zn(OH)<sub>4</sub><sup>2-</sup>** couple.

The rate of phosphate leaching is observed to be about 20 % higher in the presence of air. This is seen in the absolute value of the rate. By contrast, the OC potential is held at a values of -0.8 V vs. SHE during the whole experiment and does not show the drop down to the zincate potential. This suggests a mainly oxidised surface during exposure to the alkaline solution. Repeated experiments showed, that the time of the potential shift under deaerated conditions can vary in a range of 100 s. In aerated conditions the step was also observed after more than 1500 s. This demonstrates that the time of the abrupt change in the potential cannot be used as a reliable measurement of the phosphate concentration on the surface and layer stability.

#### 5.4.2 KINETICS OF ALKALINE LEACHING OF PHOSPHATE COATINGS ON ZINC

Figure 31 shows the leaching transients measured during alkaline dissolution of the investigated phosphate layers with changing composition.

In the case of the monocation sample (Figure 31A) the rates of **Zn<sup>2+</sup>** and **PO<sub>4</sub><sup>3-</sup>** dissolution rise rapidly to steady state values and remain relatively constant for about 100 seconds. During this steady state period, P dissolution is slightly higher than **Zn<sup>2+</sup>** dissolution. The rate of **Zn<sup>2+</sup>** and **PO<sub>4</sub><sup>3-</sup>** leaching decrease progressively, but **PO<sub>4</sub><sup>3-</sup>** leaching decreases more rapidly than **Zn<sup>3+</sup>** resulting in a change in the dissolution **stoichiometry** in the later stages of the reaction. Integration of the respective peak areas gives a total Zn / P atomic ratio of 1.36, as compared with the theoretical value of 1.5. The low value for the Zn / P ratio is probably due to the presence of zinc hydroxide on the surface after complete leaching of the phosphate ion. Both the P and Zn signals decrease to the background level at the end of the reaction.

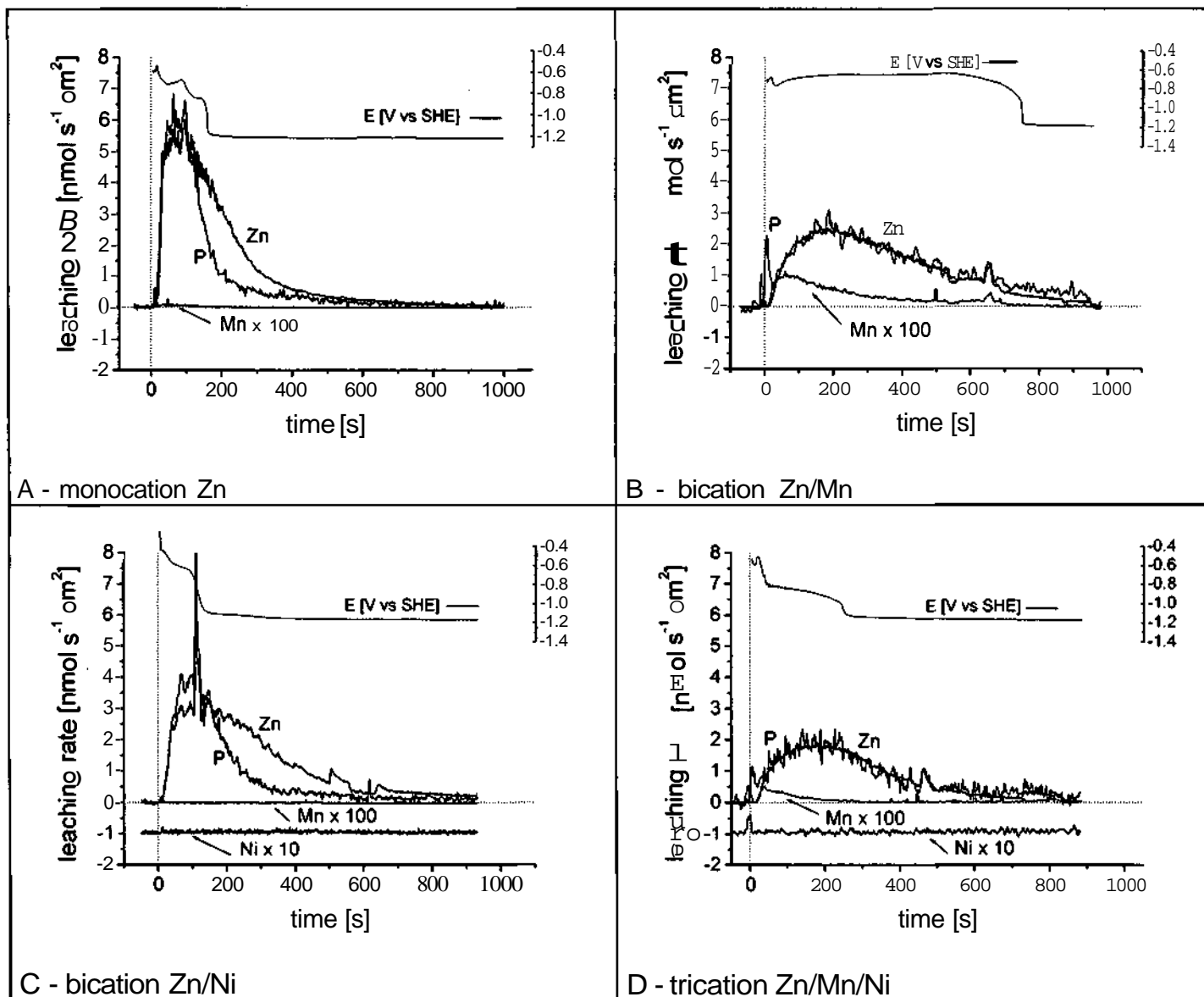


Figure 31: Leaching profiles for phosphate layers on electrogalvanised steel in 0.1 M NaOH at ambient temperature. Note that the Mn signal has been multiplied by 100 for clarity. Ni signal is shown with an offset for better presentation. The dashed lines mark  $t=0$  and  $\text{Rate}=0$ .

A dissolution transient for a bication Zn/Mn phosphate layer is shown in Figure 31B. In this case, the stoichiometry between  $\text{Zn}^{2+}$  and  $\text{PO}_4^{3-}$  remains constant (within experimental error) throughout the profile. The Mn dissolution rate has been multiplied by 100 so as to appear on the same scale as the  $\text{Zn}^{2+}$  and  $\text{PO}_4^{3-}$  dissolution rates. Some Mn dissolution is observed, but according to the chemical analysis of the layer (Table 4), only a small fraction ( $\approx 0.7\%$ ) of the total Mn appears to be soluble in the alkaline electrolyte. The majority of the Mn is observed during post dissolution in HCl solution, as described in the next section. The rate of phosphate and zinc dissolution of the Zn/Mn bication layer has been reduced by a factor of almost 3 with respect to the monocation layer. The final potential is again around  $-1.20\text{ V}$  vs. SHE consistent with the zincate equilibrium in this electrolyte.

Figure 31C shows the dissolution profile obtained for the Zn/Ni bication sample. No Ni dissolution is observed during the alkaline portion of this experiment. The dissolution rate of P is only about 25 % lower than that observed for the monocation Zn layer. The effect in increasing the stability is therefore much smaller than in the presence of Mn. This may reflect the fact that  $\text{Ni}^{2+}$  is incorporated into the phosphate crystals to a smaller extent than  $\text{Mn}^{2+}$ . The course of the open circuit potential was rather unique on the Zn/Ni samples. The zinc/zincate potential was reached already after 100 s and the drop was not as abrupt as on the other samples, but occurred with a smoother transition. The reason for this behaviour will be discussed in chapter 5.4.6 p. 74.

The dissolution curve for the trication layer is shown in Figure 31D. The behaviour is very similar to the bication Zn/Mn and demonstrates that the chemical stability of the phosphate crystals is primarily determined by the  $\text{Mn}^{2+}$ -ion. One interesting difference however is in the open circuit potential. Although the two layers show similar leaching behaviour for all elements, the open circuit potential drops to lower values immediately upon contact with the alkaline solution, and reaches the zincate potential well before the rate of phosphate dissolution begins to decrease.

### 5.4.3 COMPOSITION OF THE RESIDUAL LAYERS

After the measurement of the leaching profile in 0.1 M NaOH, residual P, Ni, and Mn were measured by exposing the surface to 0.01 M HCl. The resulting series of dissolution profiles and peak integrals are given in Figure 32 and Table 6 respectively. Residual Zn could not be measured because of the dissolution of the metallic zinc coating by the acid solution. No significant phosphate dissolution higher than 3 % was detected in any of the profiles, which demonstrates that the hydroxide/phosphate exchange occurs with nearly 100 % efficiency. The Mn quantities determined by chemical analysis (Table 4) were about 20 % higher on average than the values given in Table 6. This discrepancy is probably due to systematic error due to the estimation of the effective surface area in these experiments. A large dispersion is indicated probably due to the significantly smaller surface area in the ICP experiments. The Ni quantities are even only the half of the original layer quantity. In the analysis of phosphate layer done by etching in chromic acid small amounts of the metallic nickel present on the zinc surface may be dissolved and analysed together with the Ni-ions incorporated in the phosphate crystals. However, in the leaching experiments in 0.01 M HCl the metallic nickel is not attacked and analysed. This may explain the higher discrepancy compared to manganese.

Sample type	Leached Quantity 0.01 M HCl % of original quantity		
	Mn	Ni	P
<i>monocation Zn</i>	-	-	1.8
<i>bication Zn - Mn</i>	80.1	-	2.7
<i>bication Zn - Ni</i>	-	49.5	3.1
<i>Trication</i>	79.1	50.0	3.1

Table 6: Composition of phosphate layers on **electrogalvanised** steel as determined by integration of leaching transients in 0.01 M HCl. Zn was not measurable in the acid fraction because of substrate dissolution. The percental quantity of the original layer composition as determined by chemical analysis is shown (see Table 4)

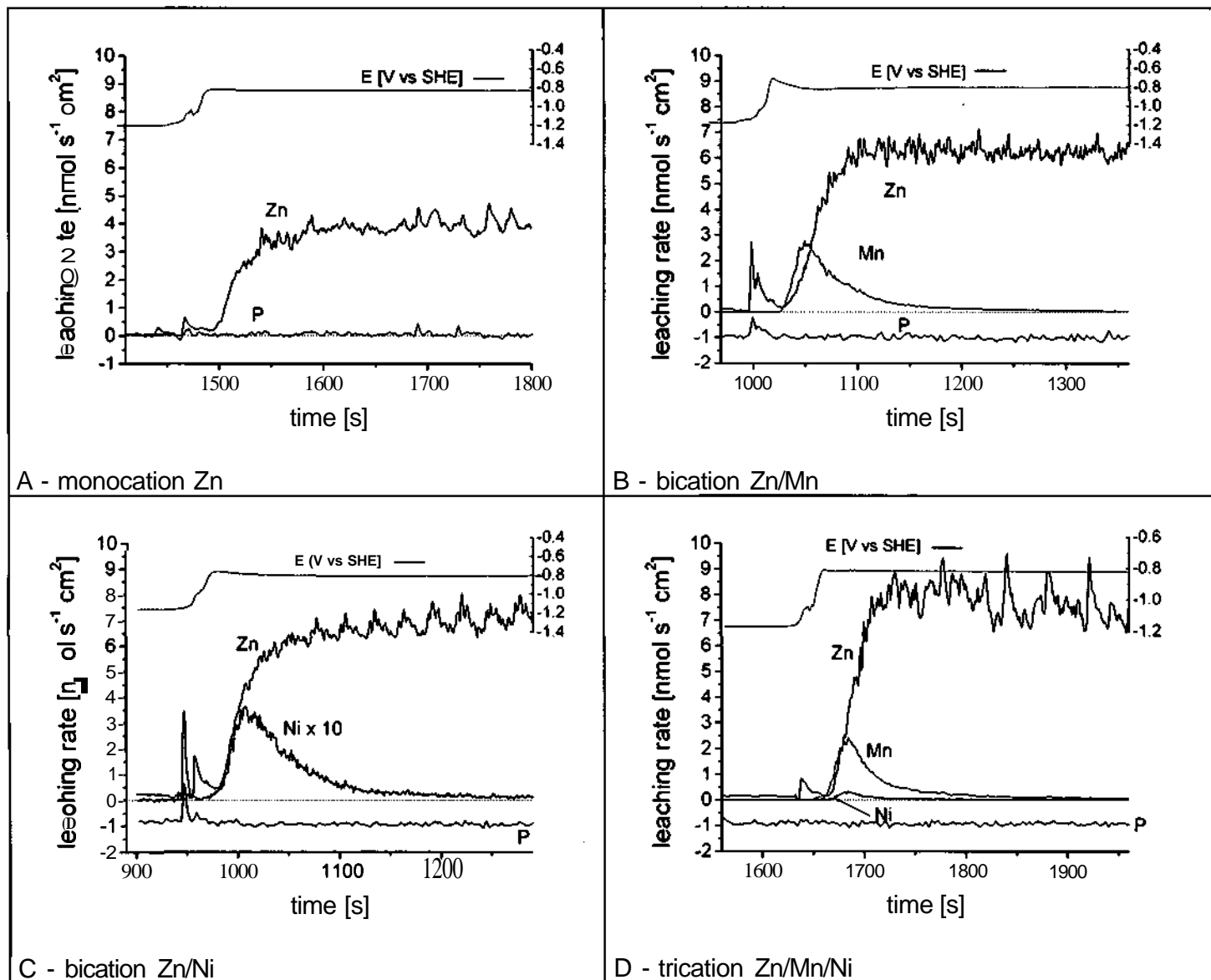


Figure 32: Post dissolution of the residual layers in 0.01 M HCl. The P-signal is showed with an offset of -1 for clarity in the presentation for (B), (C) and (D).

The first appearance of **HCl** in the sample compartment of the cell is indicated by an increase of the open circuit potential (Figure 32), which reaches the typical values for zinc dissolution in acidic environment after a certain time. Yttrium was also added to the HCl electrolyte as an internal standard to prove this behaviour. This is important because, prior to this experiment, the cell is filled with NaOH electrolyte. The open circuit potential begins to rise at the same time as the Y signal increases, however, the dissolution of the zinc substrate and the surface layer is delayed for approximately 30 s. This period is probably due to the time required to neutralize the 0.1 M NaOH solution with 0.01 M HCl.

There is a remarkable higher Zn dissolution rate in the acidic environment on phosphate layers containing Ni (Figure 32 C & D). The reason for this lies in the galvanic coupling action of the zinc and the nobler nickel, which is also present in metallic state on the surface.

In Figure 32, some small peaks are observed before the onset of the open circuit potential and the other elemental signals. These artefacts were common in this type of experiment and are explained by the procedure for changing electrolytes. At the end of the NaOH experiment the capillary was removed from the alkaline electrolyte, maintained in the air for approximately five seconds, and then placed in the 0.01 M HCl solution. In this way, the two electrolytes are separated in the capillary by an air bubble. The bubble will prevent mixing of the two **electrolytes**, but will tend to push through any stagnant electrolyte on the capillary walls. This cleaning effect in the tube leads to peaks such as seen here.



#### 5.4.4 ALKALINE LEACHING OF PHOSPHATE LAYERS ON COLD ROLLED STEEL

The results presented in the previous section demonstrate that Mn and Ni do remain on the surface in a residual film after the alkaline attack. The presence of residual Zn coming from the phosphate coating could not be detected because of the high dissolution rate of the zinc substrate in the acid. To determine whether or not residual zinc remains on the surface, a similar analysis of phosphate layers on cold rolled steel was performed. The alkaline leaching transients of the phosphate layer on cold rolled steel followed by the acid dissolution of the residual layer are shown in Figure 33. The alkaline dissolution profiles of these layers closely resemble those obtained for the galvanized steel in Figure 31. This is true even for the phosphate layer formed from a monocation bath suggesting that  $\text{Fe}^{2+}$  serves a similar role as  $\text{Mn}^{2+}$  or  $\text{Ni}^{2+}$  when incorporated into the phosphate crystal lattice.

The 0.01 M HCl experiments (Figure 33 left) demonstrate that a residual film is obtained on the surface following the alkaline treatments. Zn is detected in the acid experiment at a level of approximately 10 % of the total zinc (Table 7). The quantity of Mn leached in these experiments was much higher (189 %) than the original quantity. This can only be explained by a systematic error in the chemical analysis of the phosphate layer or a non-uniform distribution of coating weight on the sample. The higher values of the other elements (Zn, Ni, P) also suggest a wrong presumption of the real coating weight and composition in case of the trication layer on cold rolled steel.

Sample type	Leached Quantity 0.01 M HCl % of original quantity			
	Zn	Mn	Ni	P
<i>monocation Zn</i>	10.8	-	-	1.1
<i>Trication</i>	17.2	189	95	8.6

Table 7: Composition of residual phosphate layers on cold rolled steel as determined by integration of leaching transients in 0.01 M HCl. The percental quantity of the original layer composition as determined by chemical analysis is shown (see Table 4)

Finally, the rate of steel corrosion appears to be increased by more than a factor of 10 for the trication layers as compared to the monocation layer. The steady state open circuit potential was -0.52 V vs. SHE for the trication layers as compared to -0.64 V for the monocation layers. One possible explanation for these differences would be the presence of metallic nickel on the metal substrate increasing the likelihood of galvanic corrosion in the acid medium. A similar effect was already observed on electrogalvanised steel (Figure 32).

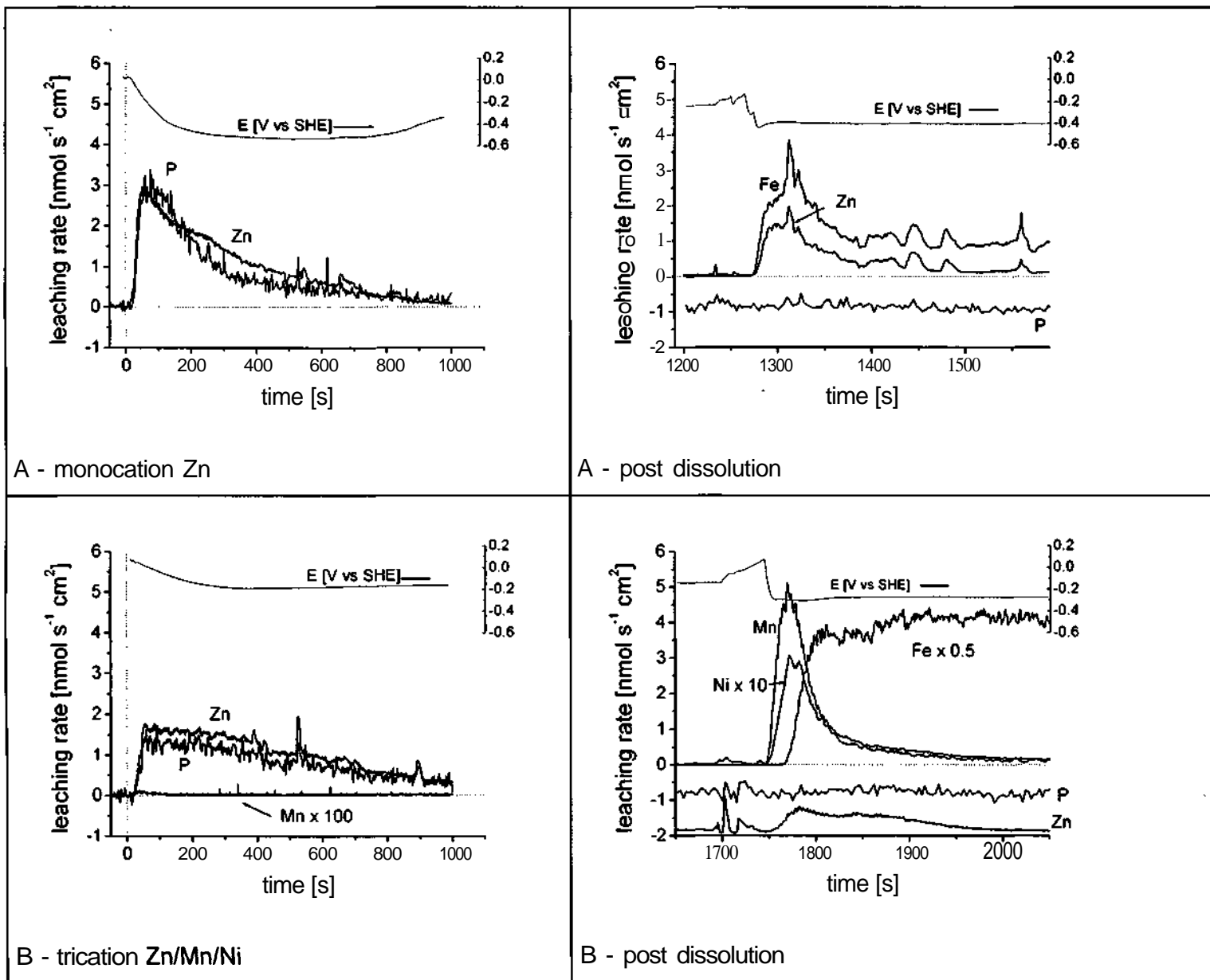


Figure 33: Leaching profiles (0.1 M NaOH) and post dissolution (0.01 M HCl) analysis for phosphate layers on cold rolled steel. (A) Monocation Zn layer; (B) Trication Zn/Mn/Ni layer. Note that certain elements are shown with offset below the rate = 0 axis for clarity.

## 5.4.5 EFFECT OF POST TREATMENT

Figure 34 shows the leaching profiles for a monocation phosphate layer rinsed with chromate solution or Deoxylyte 54NC. A slight improvement in the alkaline stability was observed. This is indicated by a decreased value of the maximum leaching rate. Both the Zn and the P dissolution were slowed down by appr. 17 % in average for both post treatments compared to untreated monocation Zn layer (Figure 31A). Some chromium in the layer was removed by the sodium hydroxide solution (Figure 34 A). The course of the open circuit potential is not remarkable different from a layer without a post treatment.

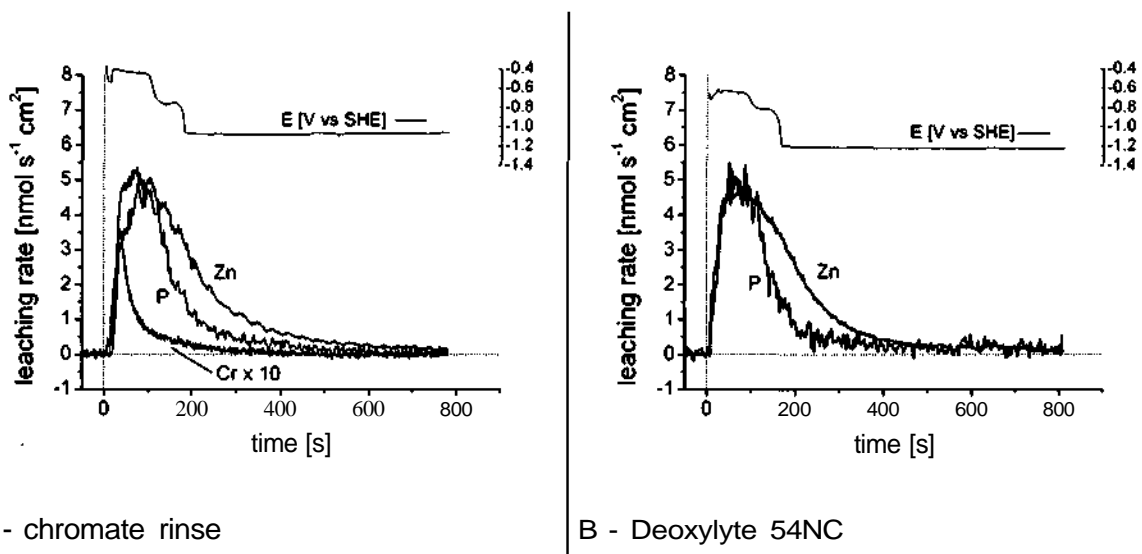


Figure 34: : Leaching profiles for phosphate layers on electrogalvanised steel in 0.1 M NaOH at ambient temperature. Monocation Zn layer with post rinses (a) chromate, (b) Deoxylyte 54NC. Note that the Cr signal has been multiplied by 10 to appear on the same scale. The dashed lines mark  $t=0$  and  $\text{Rate}=0$ .

## 5.4.6 DISCUSSION OF ICP-RESULTS

### *Analysis of Results - Rate Variation with Composition*

Figure 35 summarises the rate data for phosphate leaching as a function of the metal ion composition for the electrogalvanised samples and the cold rolled steel samples. The rate is observed to decrease in proportion to the fraction of Mn, Ni and Fe respectively incorporated into the layer. For most samples, the quantity of Ni is well below the quantity of Mn, so the inclusion of Ni in the sum is not obvious. However, the fact that the rate was reduced proportionally indicates that Ni and Mn both contribute to the alkaline resistance of the layer.

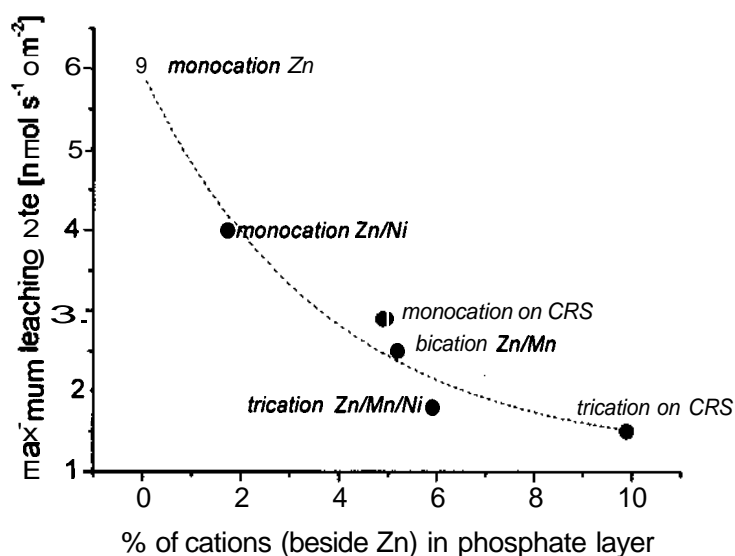


Figure 35: Phosphate leaching rate as a function of secondary metal ion composition presented as weight fraction. Four samples on electrogalvanised steel and two samples on cold rolled steel (CRS) are presented. For analysis see Table 4. The dashed curve is for a visual guide.

The phosphate layers on the cold rolled steel samples are also shown on this curve. This points are interesting in that they allow to increase the secondary metal ion content beyond what is possible for the phosphate layers on zinc coated steel. The good agreement between the monocation steel sample and the other phosphate layers indicates that presence of  $\text{Fe}^{2+}$  in the phosphate layer acts in a similar manner to  $\text{Mn}^{2+}$  or  $\text{Ni}^{2+}$  in reducing the rate of alkaline attack. The  $\text{Fe}^{2+}$  comes from the acid attack of the steel substrate and thus it is difficult to produce a true monocation phosphate layer on steel. The trication phosphate layers on steel allow to go to much higher percentage values for cations than was possible with the zinc surface.

### ***Mechanistic Considerations***

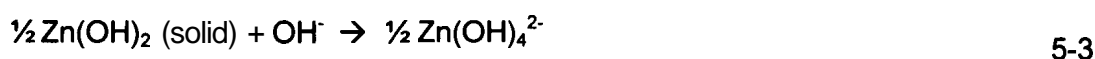
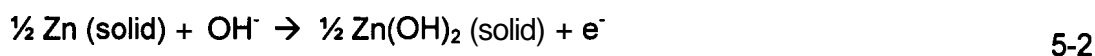
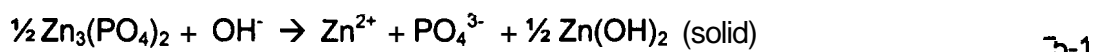
The results presented here demonstrate that **time** resolved dissolution using the ICP method is a powerful tool for measuring the stability of conversion layers with an aggressive electrolyte. With this method it was demonstrated that the elemental composition of the phosphate layer plays an important role in determining the alkaline stability of the layer. In **particular**, it was found that the addition of  $\text{Mn}^{2+}$  and/or  $\text{Ni}^{2+}$  to a zinc phosphate layer results in a significant decrease in the leaching rate of the phosphate layer. The decrease is proportional to the percentage of the substitution cations incorporated into the layer.

The fact that the Mn and Ni remain on the surface after the alkaline leaching experiment strongly suggests a chemical origin for the increased stability of the conversion layer. Morphological changes are apparent between the different conversion coatings, and we cannot completely rule out the idea that the morphology of the crystal is a determining factor, however no clear correlation with these differences was observed. Therefore, within the framework of the chemical hypothesis, it is of interest to discuss possible reaction mechanisms for the alkaline attack of the phosphate layer.

### ***Reaction model***

In all cases an initial dissolution **stoichiometry** of Zn to P close to 1:1 was measured, despite the fact that the ratio of Zn / P ratio should be 1.5 according to the stoichiometry of the phosphate layer. This result suggests that the first step of phosphate dissolution involves the incorporation of a single hydroxide ion into the phosphate layer, with the resulting loss of a single  $\text{Zn}^{2+}$  and  $\text{PO}_4^{3-}$ , as shown in reaction 5-1 on page 73. The result would be a residual layer of  $\text{Zn}(\text{OH})_2$ . To explain the kinetic results, it may be assumed that this layer dissolves more slowly. In addition, the electrochemical potential transients suggest that zinc hydroxide can be formed by the simultaneous oxidation of the zinc coupled with oxygen reduction or hydrogen formation.

Therefore, for the monocation phosphate layer, it is reasonable to write the leaching reactions as follows:



Within the framework of this model, it is reasonable to assume that the substitution of  $\text{Mn}^{2+}$  into the phosphate layer, gives rise to a mixed hydroxide film. The resulting Mn hydroxide is less soluble than Zn hydroxide, and the film may protect the underlying crystals, slowing down the reaction considerably. This model will be further elaborated in the following section (chapter 5.5) dealing with in situ Raman spectroscopy.

The basic phosphate crystalline structure is that of hopeite,  $\text{Zn}_3(\text{PO}_4)_2 \cdot 4\text{H}_2\text{O}$ . When present in the phosphating solution,  $\text{Ni}^{2+}$  and  $\text{Mn}^{2+}$  will replace  $\text{Zn}^{2+}$  in the hopeite structure.  $\text{Ni}^{2+}$  and  $\text{Mn}^{2+}$  each reduce the leaching rate by a factor proportional to their incorporation in the crystals. However,  $\text{Ni}^{2+}$  replaces  $\text{Zn}^{2+}$  in the hopeite crystal structure to a much lesser extent than  $\text{Mn}^{2+}$ , despite their nearly equivalent concentration in the original bath. Therefore, in practical terms, the addition of  $\text{Ni}^{2+}$  to conventional phosphate baths has only a minor influence on the alkaline stability of the phosphate layer. According to previous workers,  $\text{Ni}^{2+}$  will only replace  $\text{Zn}^{2+}$  in the octahedral coordination centres of hopeite, whereas  $\text{Mn}^{2+}$  replaces both tetrahedral and octahedral sites [38]. Also, the  $\text{Ni}^{2+}$  concentration in the phosphate crystals is probably much less than that measured in the analysis of Table 4. It is well known that during phosphating,  $\text{Ni}^{2+}$  deposits on the Zn surface as Ni metal, by cementation (see chapter 2.4.2).

A slight decrease in the phosphate dissolution rate was observed when oxygen is removed from the electrolyte by bubbling with nitrogen. An example is shown in Figure 30, but this effect was observed systematically for the other samples. This would suggest that the corrosion of the underlying metal substrate might contribute to phosphate dissolution, perhaps through a mechanism of anodic undermining.

### ***Open circuit potential***

The variation of the open circuit potential is also an important clue to the phenomena that occur. The final potential of -1.18 to -1.22 V vs. SHE corresponds approximately to the equilibrium value obtained for the  $\text{Zn}/\text{Zn}(\text{OH})_4^{-2}$  couple of -1.285 V vs. SHE [87]. It may be assumed that the abrupt potential drop occurs when the zinc metal is first exposed to the electrolyte and the predominate reaction becomes  $\text{Zn} + 4\text{OH}^- \rightarrow \text{Zn}(\text{OH})_4^{-2} + 2\text{e}^-$ .

For the monocation Zn layer and the bication Zn/Ni layer, the potential drop occurs before complete dissolution of the phosphate layer. This would suggest the residual film forming under these circumstances has little protective effect on the metal substrate. For the bication Zn/Mn layer, the potential drop occurs at times considerable longer than that required for the dissolution of the phosphate film. This suggests that the final steps of the phosphate film dissolution involve a slowly dissolving, protective, residual layer, and indeed, the presence of a Mn rich hydroxide film is clearly observed by acid dissolution.

When Ni is present in the phosphate layer, the potential starts at higher values and the potential drop is observed only after the passage of considerable time, regardless of the rate of phosphate leaching. It is reasonable to assume that the higher potential values are determined by the presence of metallic nickel, which will form a galvanic couple with zinc. In a similar way, there is a large increase in potential during the phosphating of zinc with Ni containing baths (see results of kinetic experiments, chapter 6.2). The Ni seals the phosphate layer, by depositing on the zinc surface exposed at the bottom of the phosphate crystal pores.

### ***Post treatment***

The post treatments gave a slight decrease in the reaction rate of P and Zn in the alkaline solution. The measured leaching profiles for samples with post treatment do not suggest a predominant mechanism of protection. The two proposed mechanism (covering of crystals and covering of bare zinc in the pores) may contribute equally well to **the** slight reduction of the reaction rate of the phosphate layer with an alkaline solution. In the case of **chromating** it has also been observed in literature [32] that the chromate reacted with the phosphate crystals to form a thin, alkaline resistant layer on the outside of the crystals. The open circuit potential gave no indication of an altered electrochemical behaviour of the zinc surface.



## 5.5 RAMAN SPECTROSCOPY

### 5.5.1 GENERAL FEATURES OF THE RAMAN SPECTRA

Figure 36 shows the Raman spectra of the zinc phosphate layer mounted into the flow cell in dry conditions (Figure 36A) and under water flow (Figure 36B) collected with the same parameters (45 s, 50x objective). The intensity under water flow was lowered to less than a half compared to the dry sample rendering some bands hardly detectable anymore. The spectrum of the sample not covered with water (Figure 36A) clearly showed all the features of zinc phosphate (hopeite) in this frequency region [73]. The main band at  $996\text{ cm}^{-1}$  indicates the symmetrical stretching vibration of the phosphate ( $\text{PO}_4^{3-}$ ) anion. It is escorted by three smaller (~one quarter of intensity) peaks at 940, 1056 and  $1149\text{ cm}^{-1}$ , which originate in the P-O stretching vibration of the phosphate anion. For a free  $\text{PO}_4^{3-}$  ion (e.g. in liquid phase) these three vibrational features are degenerated and give rise to only one Raman band as it is observed in phosphoric acid. However, distorted symmetry in the phosphate crystal lattice unties and splits the degeneracy, resulting in the three peaks observed. The deformation vibration of the phosphate tetrahedron gives rise to the band at  $595\text{ cm}^{-1}$  and the low frequency vibration at approximately  $300\text{ cm}^{-1}$  may come from a Zn-O vibration [73].

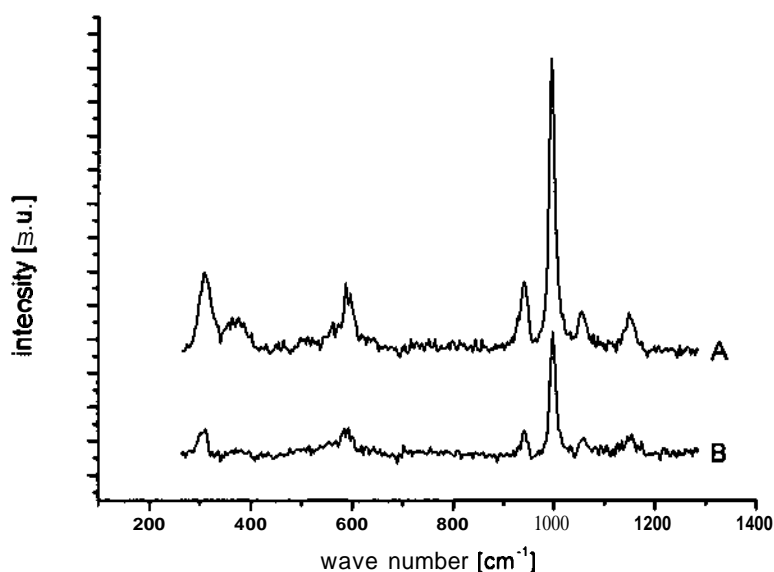


Figure 36: Raman spectra of monocation Zn phosphate layer in dry condition (A) and under water flow in the cell (B)

Switching to water flow through the cell leads to a **defocusing** of the laser beam, which made a new adjustment necessary by moving the cell ~5 mm downwards in **z**-direction. The intensity of the peaks was decreased by the high refractive damping of the laser light [84]. The refraction at the phase boundaries air/glass and glass/electrolyte causes a strong broadening of the depth of focus up to several micrometers. This broadening also distributes the intensity of the laser light over a longer distance decreasing the exciting energy reaching the sample surface. The broadening could be seen when collecting Raman spectra in the water filled flow cell with different z-positions of the table. Differences up to 5  $\mu\text{m}$  up and down from the original focus did not influence the intensity of the peaks. Hence, during the dissolution of the phosphate layer in the cell an influence on the Raman spectra due to defocusing could be excluded.

Figure 37 shows the development of the Raman spectra for the examined phosphate layers during attack of the sodium hydroxide electrolyte. Each graph exhibits only three points in time for clarity of the presentation.

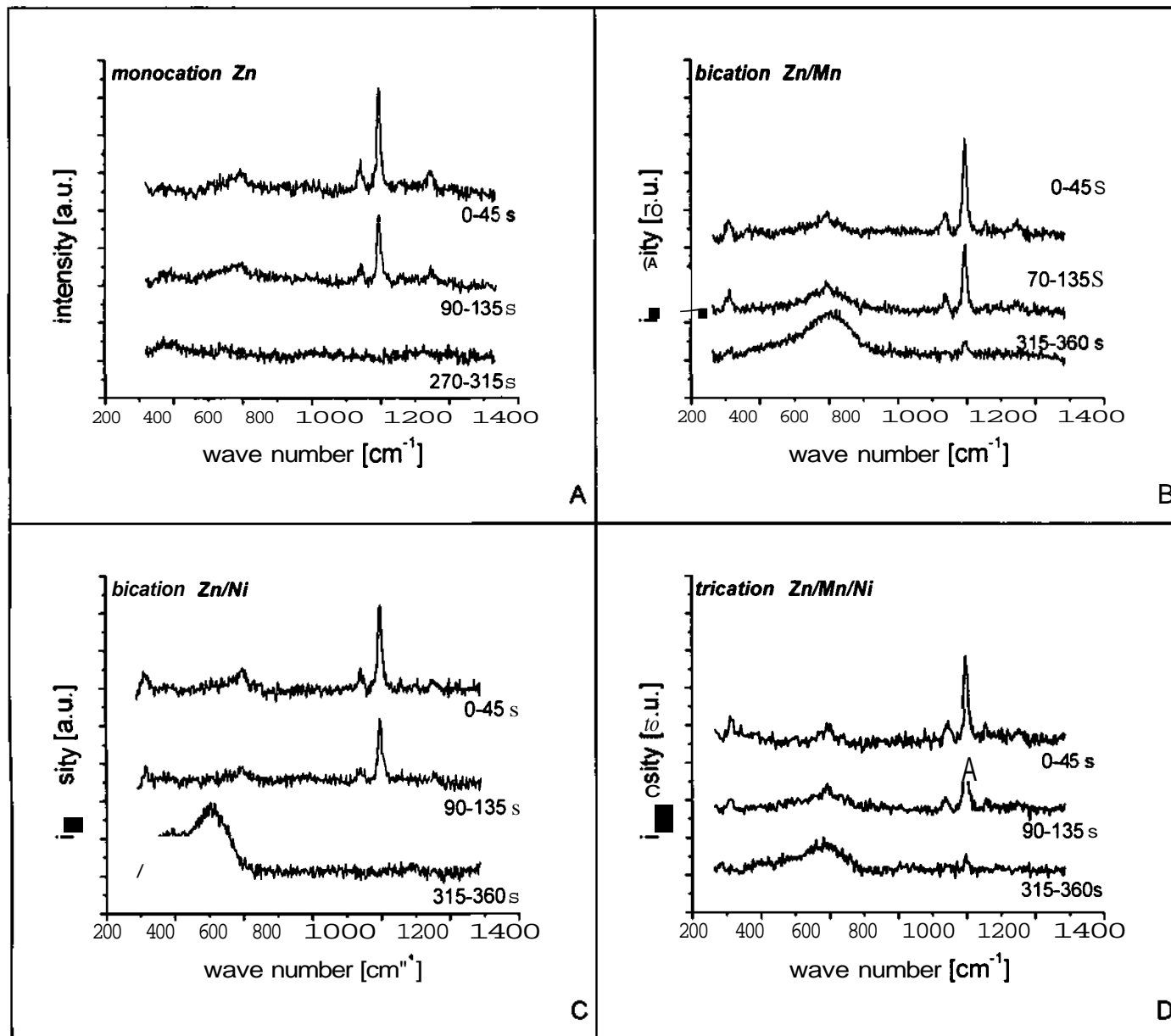


Figure 37: Development of in situ Raman spectra on phosphated samples during reaction with 0.1 M NaOH in the flow cell

## 5.5.2 KINETICS OF ALKALINE LEACHING OF PHOSPHATE COATINGS

### ***Monocation Zinc***

Figure 37A corresponds to the pure **Zn-phosphate** layer. The spectrum after the first 45 s was formed by the sharp peak at  $996\text{ cm}^{-1}$  with the escorting peaks at **1149**, **1056** and **940**  $\text{cm}^{-1}$ , which were hardly detectable even after this short time period. The broad band at  $595\text{ cm}^{-1}$  was also seen in the first **135** s of attack. The progression of the surface reaction with hydroxide is reflected in a decrease in the intensity of the characteristic phosphate features, in particular the main peak at  $996\text{ cm}^{-1}$  faded away quickly until no sign of any features could be detected in the background noise after **315** s of alkaline attack.

### ***Bication Zn/Mn***

For the Zn/Mn phosphate layer Figure 37B the very first spectrum after 45 s again shows the characteristic phosphate peaks. The weakening of the main feature at  $996\text{ cm}^{-1}$  could easily be **followed**, but happened at a distinctly lower rate compared to the pure Zn-phosphate layer, because the peak was still detectable after 360 s of attack. As the phosphate peaks disappeared progressively, a broad band at  $600\text{ cm}^{-1}$  formed and gradually increased with time. In the beginning of the attack this band was formed by the deformation vibration of the phosphate tetrahedron as it was seen on the monocation layer as well. A slight shift of the maximum to approximately  $600\text{ cm}^{-1}$  was observed during the attack. Since only Mn-containing layers exhibited this band, it can be excluded that it results from a vibrational feature in the original phosphate layer.

### ***Bication Zn/Ni***

Spectra on Zn/Ni layers Figure 37C exhibited a similar behaviour like the pure Zn-phosphate layer concerning the decrease of phosphate intensity at  $996\text{ cm}^{-1}$ , indicated by the total absence of this feature after 360 s. Two bands at  $380$  and  $510\text{ cm}^{-1}$  appeared with increasing time of exposure. The growth of the bands proceeded not in the smooth development as was seen for the  $600\text{ cm}^{-1}$  band on Mn-containing layers, but the arise happened abruptly from one measurement to another.

### Trication Zn/Mn/Ni

Spectra obtained on trication Zn/Mn/Ni-phosphate layers Figure 37D were similar to those from Zn/Mn-phosphate layers concerning the formation of the band at  $600\text{ cm}^{-1}$  and the velocity of the decrease of the phosphate peak. Residual intensity of the phosphate vibration could be seen even after 360 s.

### 5.5.3 SOME ASPECTS OF QUANTIFICATION

For a quantification of the phosphate leaching rate, the course of the Raman intensity with time of the phosphate peak at  $996\text{ cm}^{-1}$  was evaluated by a non linear curve fitting method. Due to the high noise of the in-situ measurement a simple graphical integration of the peaks delivered impracticable results with irreproducible behaviour, therefore a curve fitting procedure was chosen, in the course of which a simultaneous smoothing of the peaks was also obtained.

Spectroscopic peaks usually can be fitted by a Gaussian, a Lorentzian or a Voigt function [88], the later being a convoluted form of the first two functions. In this study all three functions were applied to fit the experimental data using the program Microcal Origin 6.0 (Figure 38).

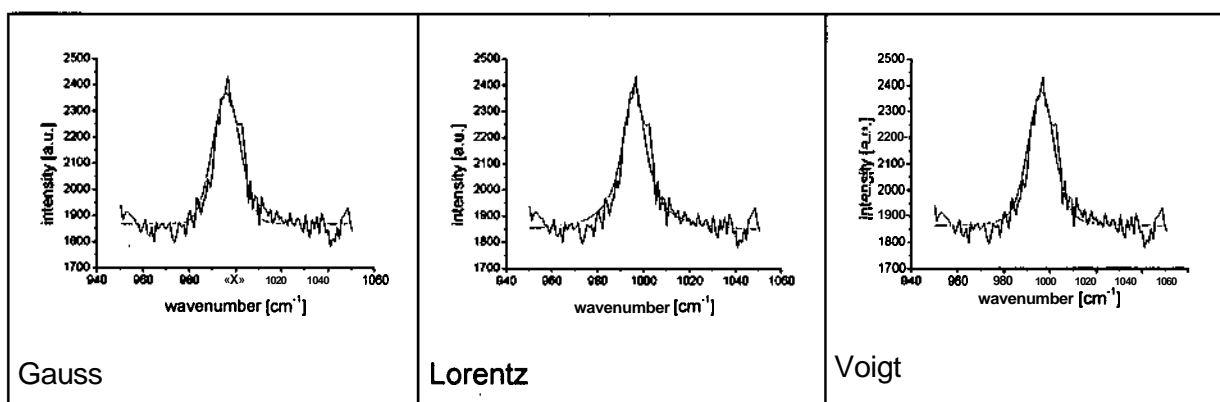


Figure 38: Different curve fits (red) for Raman peaks (black)

The Voigt function gave the best overall fit but showed difficulties with convergence, requiring permanent supervision during calculation to support the fitting procedure by suitable adjustment of the initial parameter values. In the case of the Lorentzian fit it was possible to let the program do all the fits very quickly without observing the fitting procedure. The results of the Lorentzian fit were only slightly worse than those of the Voigt function, and thus, the Lorentzian fit was used for the remainder of

this work. The fixed adjustment of the peak value to  $996\text{ cm}^{-1}$  and the constraint of the allowed half width to values from 9 to  $13\text{ cm}^{-1}$  assured a stable fitting process and avoided unreasonable results for peaks with low signal to noise ratio especially after long reaction times. The area of the peaks was easily expressed by the normalising factor of the Lorentz function.

In case of the product peaks on the layers which formed during reaction with hydroxide, a curve fit was not suitable due to the non-uniform shape of this bands (band at  $600\text{ cm}^{-1}$  on Mn-containing layers, band at  $510\text{ cm}^{-1}$  on Zn/Ni layer). Therefore the area of this peak was simply determined by graphical integration after a smoothing operation.

Figure 39 shows the intensity transients for the phosphate peak at  $996\text{ cm}^{-1}$  obtained with the described fitting procedure for the investigated phosphate layers. For a comparison of different layers in terms of reaction rates the peak area was normalised to the value of the very first Raman spectrum obtained within the first 45 s of attack and linear extrapolated to the zero point in time. Additionally the area of the peaks formed during attack is shown in the diagrams. For the Zn, the Zn/Mn and the trication Zn/Mn/Ni this is the band at  $600\text{ cm}^{-1}$ , for the bication Zn/Ni layer the development of the band at  $510\text{ cm}^{-1}$  is shown.

All layers exhibited a decrease of the phosphate intensity in a near linear manner. The limit of phosphate detection was reached after 250 s in case of the Zn and Zn/Ni-phosphate layers, whereas on Mn-containing layers residual phosphate intensity was still detectable after 360 s. The development of the band at  $600\text{ cm}^{-1}$  was determined by the deformation vibration of the phosphate tetrahedron in the first 135 s of attack. A distinction of the phosphate peak and the band of the reaction product was not possible due to the close distance of the band maxima ( $5\text{ cm}^{-1}$ ). On the monocation Zn-phosphate layer (Figure 39A) this band decreased steadily with time indicating the leaching of the phosphate layer like the peak at  $996\text{ cm}^{-1}$ .

The appearance and slow increase of the band at  $600\text{ cm}^{-1}$  observed in the presence of Mn occurred progressively with phosphate leaching. The product bands of the bication Zn/Ni-layer at  $380\text{ cm}^{-1}$  and  $510\text{ cm}^{-1}$  showed an abrupt appearance after 225 s and then increasing intensity with time. Figure 39C shows the intensity transient for the band at  $510\text{ cm}^{-1}$ .

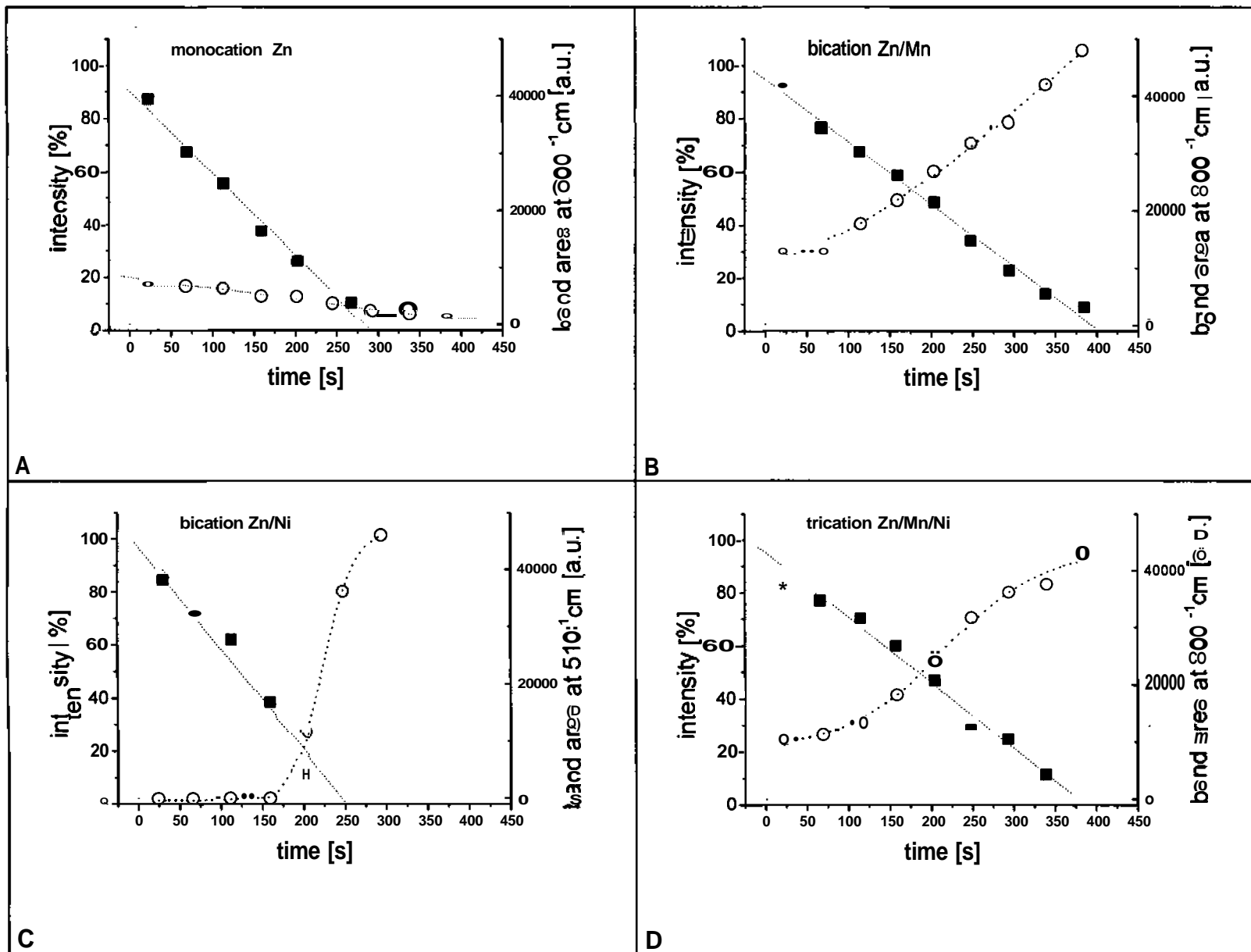


Figure 39: Development of the intensity of the Raman bands during reaction with 0.1 M NaOH.

A - monocation Zn phosphate;  
 B - bication Zn/Mn phosphate;  
 C - bication Zn/Ni phosphate;  
 D - trication Zn/Mn/Ni phosphate.

● - Raman peak at 996cm<sup>-1</sup>,  
 ○ - band at 600cm<sup>-1</sup> for A, B and D, band at 510cm<sup>-1</sup> for C.

#### 5.5.4 IDENTIFICATION OF REACTION PRODUCTS

With the exception of the monocation phosphate layer all phosphating variants showed the development of Raman bands during the alkaline attack, which could not be attributed to vibrations in the original phosphate crystal lattice. On Zn/Mn and Zn/Mn/Ni samples we observed the formation of a broad band at  $600\text{ cm}^{-1}$ . The development of the intensity of this band is shown in Figure 39B & D in comparison with the decreasing of the phosphate intensity. It can be seen that the formation of this band occurred progressively as the phosphate decreased.

The band at  $600\text{ cm}^{-1}$  is assigned to the Mn-O lattice vibration of  $\text{MnO}_2$  in thin films by Gosztoła and Weaver [89] and to a manganese compound in an oxidized state of uncertain stoichiometry by Bernard and co-workers [90]. It is most likely that the primary reaction product of the alkaline attack on Mn-containing phosphate layers is  $\text{Mn(OH)}_2$ , because this compound can be formed simply by ion exchange of the phosphate anion in the crystal lattice with  $\text{OH}^-$  in the electrolyte without any oxidation reaction necessary.  $\text{Mn(OH)}_2$  is unstable when exposed to air and rapidly oxidises to  $\text{MnO}_2$ , whereas under the electrolyte film during the Raman measurements this oxidation may be facilitated by the energy of the laser beam as proposed by Bernard [90] in their in-situ Raman study of  $\text{Mn(OH)}_2$  films during polarization. The instantaneous oxidation of the formed  $\text{Mn(OH)}_2$  to  $\text{MnO}_2$  by the exciting laser could explain why no low frequency Mn-OH vibrational bands were observed in this work. Such bands should usually appear in the region of  $300\text{ cm}^{-1}$  [90].

Oxidation of the residual layers was also observed after removing the samples from the cell. The attacked spot quickly turned brown when exposed to air. Whatever the exact oxidation state of this Mn-phase is, the results clearly showed the formation of a Mn-rich oxide/hydroxide phase on Mn-containing samples, which was accompanied by a distinct decrease in the phosphate leaching rate.

For Zn/Ni layers we observed two bands at  $380\text{ cm}^{-1}$  and  $510\text{ cm}^{-1}$ . Figure 39C shows the development of the band at  $510\text{ cm}^{-1}$  together with the decrease in the phosphate signal. In the case of the Zn/Ni phosphate layer the  $510\text{ cm}^{-1}$  peak appears abruptly, very different from the progressive increase in the  $600\text{ cm}^{-1}$  peak observed for the Mn-containing layers. It is probable that the  $510\text{ cm}^{-1}$  peak is due to NiO. Melendres [91] observed a peak at  $510\text{ cm}^{-1}$  during anodic oxidation of Ni-electrodes, which he



assigned to Ni-O vibration in NiO. The assignment of the  $380\text{ cm}^{-1}$  peak is however, more difficult. Ni-hydroxide films have been extensively examined with Raman spectroscopy [92,93] and yet no evidence has been forthcoming to suggest the  $380\text{ cm}^{-1}$  band originates from a Ni-OH vibration. Therefore, it is reasonable to attribute this band to  $\text{Zn(OH)}_2$ . The beta-modification of  $\text{Zn(OH)}_2$  has its main feature at  $380\text{ cm}^{-1}$  [49], and yet no other peaks were detectable in the in situ Raman spectra for a confirmation of the proposed assignment. Usually the low frequency peaks of metal hydroxides are accompanied by OH-stretching bands in the high frequency region around  $3200\text{ cm}^{-1}$ . With the measurements in the flow cell, the observation of such bands was not possible because of the strong scattering of the electrolyte (NaOH), leading to a non characteristic broad band around  $3300\text{ cm}^{-1}$  observed on all layers during the experiments. The samples still showed no bands in this region after the alkaline attack in the dry state.

The total absence of OH-stretching bands in the Raman spectra can be explained by the generally low intensity of this vibrations and the fact that the highly disordered, amorphous structure of the developing hydroxide films do not have characteristic OH-vibrations. Simple comparison with chemically produced standard substances is often not successful because of structural differences of the in-situ formed hydroxide layers on metal substrates. A clear assignment of the bands forming during the alkaline attack on **Zn/Ni** phosphate layers is not possible.

The trication layers showed the same resulting bands as the Zn/Mn layers. Although Ni is present at roughly the same concentration as in Zn/Ni samples, there was no sign of the  $380\text{ cm}^{-1}$  band similar to what was observed for the **Zn/Ni-layer** caused. The influence of nickel seemed to be suppressed by the contribution of the **Mn-O** vibration dominating the Raman spectra. It can be proposed, that the formed Mn-oxide/hydroxide layer during the alkaline attack protects both phosphate crystals and substrate from further attack and therefore decreases the phosphate leaching rate.

## 5.5.5 DISCUSSION

### *Estimation of Reaction Rates*

The intensity transients of the phosphate peak (Figure 39) show a decrease in intensity in a near linear manner and therefore simple linear regression for roughly estimating the reaction rate for the different phosphate layers was chosen. Values below 10 % of the initial intensity were left out of the regression, because they did not allow a clear distinction between noise and **signal**, although in some cases the phosphate peak was still detectable under these conditions. The slopes obtained with this procedure (Figure 40) show the highest rate and therefore the lowest stability for monocation Zn-phosphate layers and for the **Zn/Ni** phosphate layer. A significant decrease in the rate is only provided in the presence of Mn, as seen for the bication sample Zn/Mn, with a slight improvement in the presence of Mn and Ni on the trication sample Zn/Mn/Ni exhibiting the highest alkaline stability.

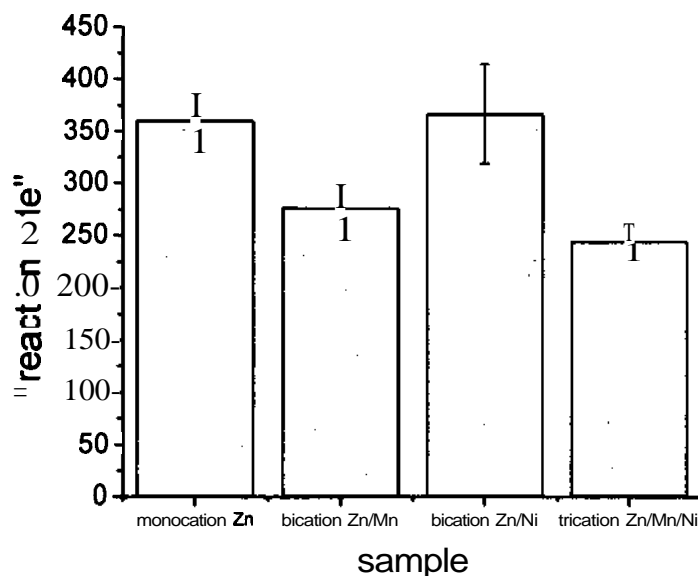


Figure 40: Slopes (= "reaction rate") obtained from linear regression of the intensity transients for Raman band at  $996\text{cm}^{-1}$  for the different phosphate layers. Error bars show confidence interval of five measurements.

The results show the same tendency as the leaching rates obtained with ICP flow analysis (chapter 5.4.2), where in the presence of Mn, the rate of phosphate leaching decreased by a factor of three as compared to pure Zn phosphate layers. Although the reaction rates could be followed with Raman spectroscopy, the differences in stability of

the various layers are much smaller than measured with the ICP. One has to consider that the formation of reaction products may attenuate the Raman response of the underlying phosphate layer. Under these conditions the signal would decrease faster and suggest a higher rate of phosphate removal than really happens.

### **Post treatments**

The alkaline stability of the monocation layer with a post treatment was examined with the same procedure and flow conditions as the above mentioned experiments concerning the influence of the cations. Evaluation and calculations were done in the same way. The slope of the obtained regression curves is shown in Figure 41. The Raman spectra showed only vibrational band that come from the phosphate layer itself. No species from the post treatment could be detected.

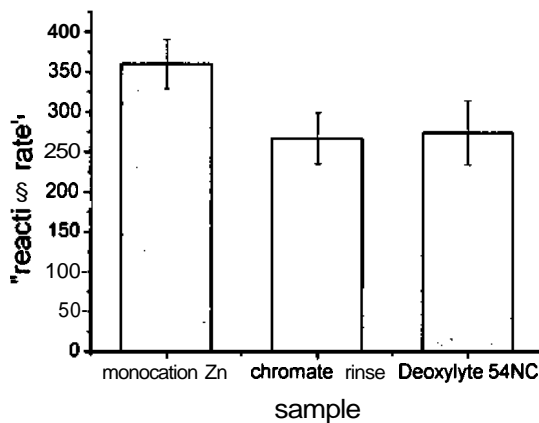


Figure 41: Slope (= "reaction Rate") of alkaline attack on Zn-phosphated samples with various post rinses. (Slope of linear regression of the decrease of Raman signal)

The slope of the pure zinc phosphate layer is shown again for comparison. A clear influence in increasing the alkaline stability with a post treatment of the phosphated samples can be seen as already observed in the ICP experiments (chapter 5.4.5 p. 70). Chromate rinse and Deoxylyte 54NC give similar results. Basically the improvement of the stability can be done by a protective covering of the phosphate crystals itself and/or by covering the bare zinc surface between the crystals and preventing undermining of the layer.

### Open Circuit Potential

The course of the open circuit potential during the alkaline attack is displayed in Figure 42 for all phosphate layers investigated. All curves exhibited a potential step down to appr. -1.2 V vs. SHE after a certain time, which corresponds to the zinc/zincate couple. The starting potential values were in the range from -0.65 to -0.5 V vs. SHE and decreased gradually till approximately -0.8 to -0.9 V when a sudden drop down to -1.15 V vs. SHE occurred.

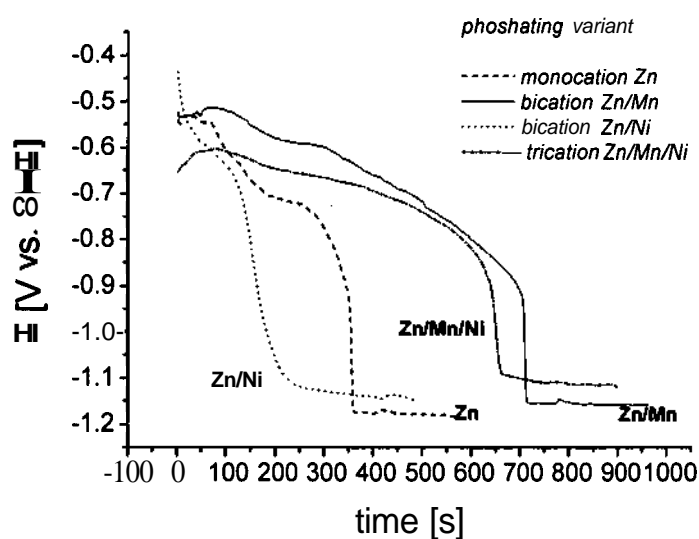


Figure 42: Open circuit potential of phosphated samples during reaction with 0.1 M NaOH in the Raman flow cell.

For the monocation sample this step happened after ~350 s reaching the lowest potential of all samples (-1.17 V vs. SHE). In the presence of Mn the time of the potential step was prolonged to over 700 s with a slightly higher final potential of -1.15 V vs. SHE. Completely different behaviour was seen on Zn/Ni-phosphate layers. This sample showed a smoother adjustment of the final potential of -1.14 V vs. SHE. which occurred already after ~200 s. On the trication layers the highest end potential of -1.11 V vs. SHE was observed, which was reached after ~620 s with a smoother transition compared to Zn and Zn/Mn layers.

The qualitative shape of the open circuit potential curves corresponds well to the results obtained in the ICP flow cell, which were presented in chapter 5.4.2. Despite the different constructions and flow conditions of the cells similar behaviour was observed on all samples. The course of the open circuit potential in the in situ Raman spectroscopy also did not reflect the kinetics of the alkaline attack. However, all samples showed the

potential step down to the zinc/zincate couple, which happened at different times for different samples (earliest step on **Zn/Ni-samples**, longest time to step on Zn/Mn-samples).

In chapter 5.4.6 (discussion of the **ICP-data**) it was suggested, that the primary reaction product of the reaction of monocation phosphate layers with alkaline media is **Zn(OH)<sub>2</sub>**, which is produced by ion exchange of OH<sup>-</sup> with the phosphate and zinc ions and therefore contributes to the anodic potential in the beginning of the reaction. It can be assumed that the initial potential corresponds to the oxidised Zn **surface** with **Zn/Zn(OH)<sub>2</sub>** as potential determining electrode couple. The OH<sup>-</sup>-ion consuming reaction with phosphate ensures a local decrease in **pH-value** near the zinc surface leading to a low enough activity not to form zincate ions by active dissolution of zinc or **Zn(OH)<sub>2</sub>**. If the amount of phosphate falls under a certain value, the reaction may go on by dissolution of zinc and **Zn(OH)<sub>2</sub>**, indicated by a potential jump down to -1.2 V vs. SHE. In that case the direct dissolution of the zinc substrate becomes the predominant reaction.

The prolonged time of the potential step in the presence of **Mn** was also observed in the **ICP** experiments. The proposed protective effect of a stable Mn-hydroxide layer now is confirmed by the in situ Raman spectra, which clearly showed the formation of Mn-oxide/hydroxide.

In the presence of Ni, the final potential is stabilised at higher values and the potential drop is observed much earlier compared to the other samples. The phosphate leaching rate determined by ICP flow analysis and by Raman spectroscopy was rather similar to the rate on pure Zn-phosphate layers with a slightly higher stability. Therefore a decreased alkaline stability of the phosphate crystal by nickel cannot be responsible for the early occurrence of the potential step. As nickel is also present in the metallic state on the substrate, a galvanic coupling action between zinc and the nobler nickel may be responsible for a quicker adjustment of zinc/zincate as active couple. The dissolution of zinc in alkaline media is a mixed potential process with hydrogen evolution as the cathodic reaction [53]. The metallic nickel present on the zinc surface may support this reaction by acting as the cathodic area.

## 5.6 QCM STUDY OF ALKALINE STABILITY (QCM COMBINED WITH ICP)

### 5.6.1 EXPERIMENTAL

After electrodeposition of a 4  $\mu\text{m}$  zinc coating onto the **Pt/quartz** crystal assembly, as described in chapter 4.8, phosphate coatings were then deposited on the surface using bathes with a composition similar to that described in the experimental section (chapter 4.2). However, the phosphating was performed in beakers on the laboratory bench rather than with the phosphating pilot line used for the technical samples. Phosphating was done by dipping in the bath for 25 s.

The dissolution of the phosphate layer on the zinc coated quartzes in 0.1 M **O<sub>2</sub>-free** NaOH was followed using the QCM combined with the ICP flow analysis. The experiments were identical to those undertaken on the technical samples with the addition of the monitoring of the QCM frequency in addition to the ICP dissolution transients. Data for a monocation Zn-phosphate layer and for the two bication Zn/Mn and Zn/Ni layers were obtained. For some reason it was not possible to obtain meaningful **ICP-data** on the trication phosphated quartz. The coating weight might have been too low to receive sufficient intensities in the **ICP-measurement**.

### 5.6.2 RESULTS

Figure 43 - Figure 45 show the leaching rates as measured by the ICP and the OCP during the attack of the 0.1 M NaOH. These data are in good agreement with those obtained for the technical samples reported in 5.4.2, even in the measured values of the maximum leaching rate and not only in the ranking of the samples. As before, the rate of the attack is slowed in presence of Ni and Mn (Figure 44 and Figure 45), and Mn has the strongest effect. This demonstrates that the phosphate layers formed on the **Zn/quartz** system have similar composition and chemical stability as the technical samples.

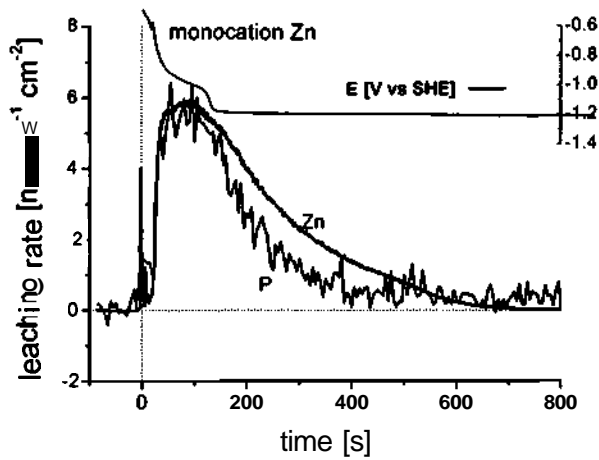


Figure 43: Leaching profile and OCP for a **monocation** phosphate layer on a zinc coated quartz in 0.1 M NaOH at ambient temperature.

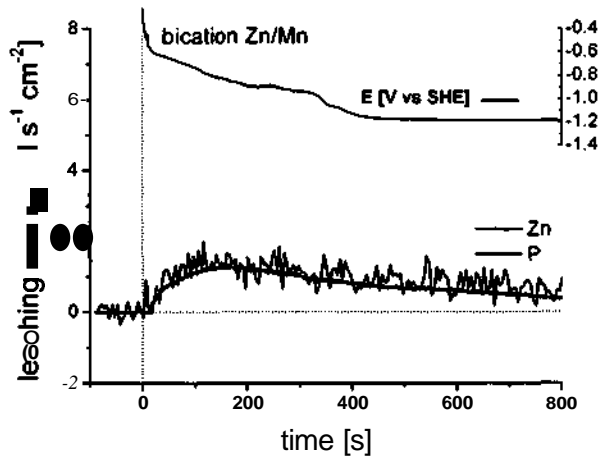


Figure 44: Leaching profile and OCP for a **bication Zn/Mn** phosphate layer on a zinc coated quartz in 0.1 M NaOH at ambient temperature.

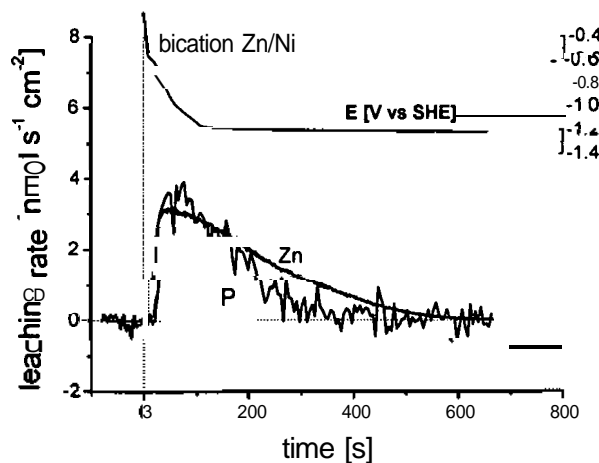
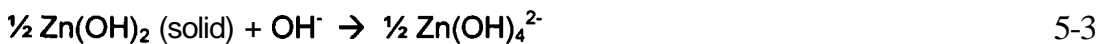
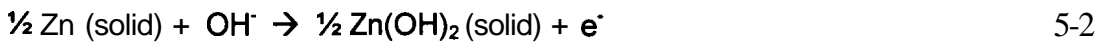
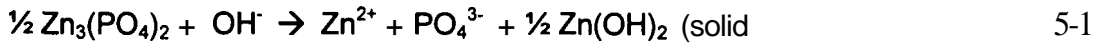


Figure 45: Leaching profile and OCP for a **bication Zn/Ni** phosphate layer on a zinc coated quartz in 0.1 M NaOH at ambient temperature.

### 5.6.3 DISCUSSION - QUANTITATIVE RELATIONSHIPS

To interpret the QCM-ICP data, the following reaction scheme is used, based upon the discussion presented in the ICP-Chapter (5.4.6 p. 71)



In the absence of oxygen, it is reasonable to assume that reaction 5-3 will make only a minor contribution to the total mass change. In presence of Mn, reaction 5-1 leads to a mixed hydroxide consisting of Zn and Mn, where  $\text{Mn}(\text{OH})_2$  is essentially insoluble.

To develop a quantitative relationship, some reasonable assumptions about the nature of the system must be made. First of all, we assume that every molecule of phosphorous dissolved comes from one molecule of hopeite. As long as P and Zn dissolve in an equimolar ratio, the remaining Zn-atom from the hopeite structure will form a hydroxide layer according to reaction 5-1. So in the initial phases of the attack there should be incorporation of OH ions, which are dissolved again as reaction continues. In this way, a relationship between the total mass change (QCM) and the P and Zn dissolution rates (ICP) may be obtained as shown in Table 8.

<p><b>surface mass of hopeite</b></p> $\Delta M_{\text{hop}} = V_P n * \text{MW}(\text{hopeite}) = - V_P / 2 * 458.2$	5-4
<p><b>surface mass of zinc hydroxide</b></p> $\Delta M_{\text{Zn}(\text{OH})_2} = V_P / 2 * \text{MW}(\text{Zn}(\text{OH})_2) - (V_{\text{Zn}} - V_P) * \text{MW}(\text{Zn}(\text{OH})_2)$ $= (3/2 V_P - V_{\text{Zn}}) * 99.4$	5-5
<p><b>total mass change</b></p> $\Delta M_{\text{total}} = - V_P / 2 * 458.2 + (3/2 V_P - V_{\text{Zn}}) * 99.4$	5-6

Table 8: Relationship between mass changes (QCM) and dissolution rates (ICP).  $V_P$ ,  $V_{\text{Zn}}$  = leaching rates of P, Zn respectively.



The calculated total mass change as received from **ICP** data, the calculated surface mass of the hydroxide layer (Eq. 5-5) and the mass transients measured with **QCM** are compared in Figure 46 - Figure 47. The consideration of Mn in the calculation of the hydroxide mass does not change the results very much, because of its low concentration and a similar molar weight as Zn.

In case of the monocation and the bication Zn/Ni layer (Figure 46 and Figure 48) we see that the calculated surface mass for the **Zn(OH)<sub>2</sub>** increases at the beginning until a maximum at 177 s for the monocation layer and till 216 s for the **Zn/Ni-layer**. Then the hydroxide amount decreases again in conformity with the proposed model.

From the **ICP-leaching** rate on the monocation layer (Figure 43) it is observed that Zn and P dissolve in an equimolar ratio until around 180 s. Then Zn dissolution **starts** to exceed the **P-leaching** rate, which coincides with the calculated decrease of the hydroxide surface mass. In presence of Mn (Figure 44 and Figure 47) Zn and P are leached from the surface in an equimolar ratio throughout the experiment. Therefore the incorporation of OH<sup>-</sup> ions (**Zn(OH)<sub>2</sub>** curve in Figure 47) increases steadily. This also is in agreement with the proposed functionality of **Mn<sup>2+</sup>** in forming a stable hydroxide layer protecting the phosphate and the zinc hydroxide from further dissolution. Generally the total mass change as calculated from the **ICP-data** is in agreement with the mass transients received by the QCM-frequency data. However, there are still some discrepancies, which may be due to deviations from the theoretical approach given by the Sauerbrey-equation. The theoretical mass-frequency relationship depends on the rigid adhesion of the formed film on the quartz and on the absence of included liquid in the layer. These requirements may not be fulfilled in the case of amorphous metal hydroxide films formed during the reaction.

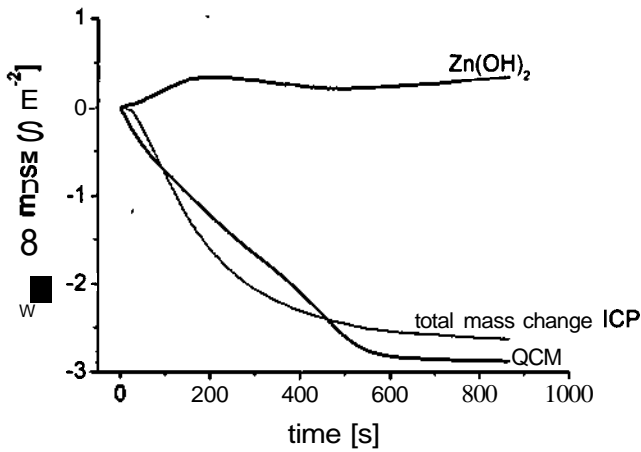


Figure 46: Mass transients for attack of **monocation** phosphate layer on a zinc coated quartz in 0.1 M NaOH. (see also Figure 43)

$\text{Zn(OH)}_2$  - calculated from 5-5, total mass change calculated from Zn dissolution measured with ICP and QCM mass transients are shown.

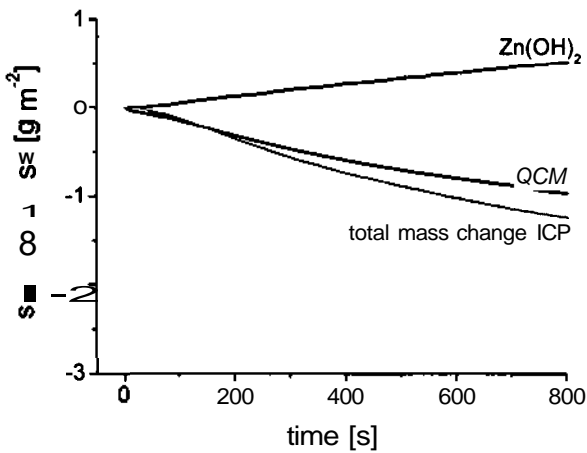


Figure 47: Mass transients for attack of **bication Zn/Mn** phosphate layer on a zinc coated quartz in 0.1 M NaOH. (see also Figure 44)

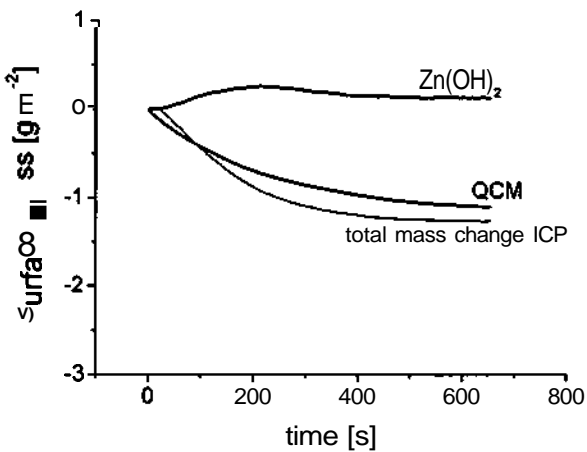


Figure 48: Mass transients for attack of **bication Zn/Ni** phosphate layer on a zinc coated quartz in 0.1 M NaOH. (see also Figure 45)

## 5.7 CONCLUSIONS

In this chapter, it could be demonstrated that the **ICP** method, Raman spectroscopy and the quartz crystal microbalance (QCM) may be used to measure the dissolution rate of conversion coatings. From the results of this **study**, we are now in a better position to assess the value of **Mn** and Ni in the phosphate layer in increasing the chemical resistance of the conversion coating at the metal / polymer interface. Mn enhances the alkaline resistance of the phosphate layer by forming a less soluble, protective Mn hydroxide film when the phosphate layer is exposed to the hydroxide ion. Ni by contrast, has only an indirect influence on the phosphate film. It deposits on the zinc **surface** surrounding the crystals, thereby protecting the crystals from anodic undermining. The two mechanisms taken together present an interesting synergy, and are analogous to the mechanisms proposed for chromate post treatment. Which of these two aspects will be important for determining the corrosion resistance of a specific painted steel product will depend upon the specifics of the corrosive environment. Other things being equal, the alkaline resistance afforded by Mn might be most helpful for a mechanism of cathodic delamination such as is commonly observed on painted steel, while the resistance offered by Ni might be more important in the situation of anodic delamination such as is observed for painted zinc coated steel in a salt spray test.

## 6 KINETICS OF PHOSPHATING

### 6.1 BACKGROUND

The phosphate layer formation reaction involves a dissolution - precipitation mechanism (see chapter 2.3.3.1). The anodic dissolution of the metal substrate is coupled with the reduction of hydrogen ions or other oxidising agents in the electrolyte. The possible reactions of common accelerators were already shown on page 9. In the work of this chapter parameters like temperature and type of accelerator on the phosphating reaction were examined by means of the QCM and the **ICP-AES**. Especially, the anodic dissolution of electrodeposited zinc in presence of various accelerators was investigated by a combination of the two techniques. However, at the beginning potential vs. time transients during phosphating and cyclic **voltammetry** results are presented to give a better understanding of the reaction steps and mechanism.

### 6.2 ELECTROCHEMICAL EXPERIMENTS

The potential vs. time transient experiments were used to examine performance of various accelerators and to study the temperature dependence of the phosphating reaction. In presence of nickel, the potential transients show a characteristic shift to more positive potentials at the end of the phosphating reaction. The time at which this potential jump takes place is often used as an approximate measure of the required phosphating time.

The potential jump is due to the deposition of metallic nickel on the metal surface exposed between the phosphate crystals (see chapter 2.4.2. p. 14). The potential jump occurs when the coverage of the phosphate crystals reaches a certain critical value so that the zinc surface is transformed into a nickel surface all at once. The assumption of this method is that the deposition of nickel is significantly slower than the precipitation of the phosphate film and thus the open circuit potential is determined by zinc dissolution as long as significant layer formation takes place. Although this method is commonplace, the assumptions upon which it is based should be born in mind as they may not hold true

under all conditions. An experimental verification of this method under the conditions of the experiments in this work is shown in Figure 49. Here the variation of potential and coating weight with time for a trication-phosphating bath was measured. It can be seen that the coating weight reaches a constant value at the time of the potential shift (red curve).

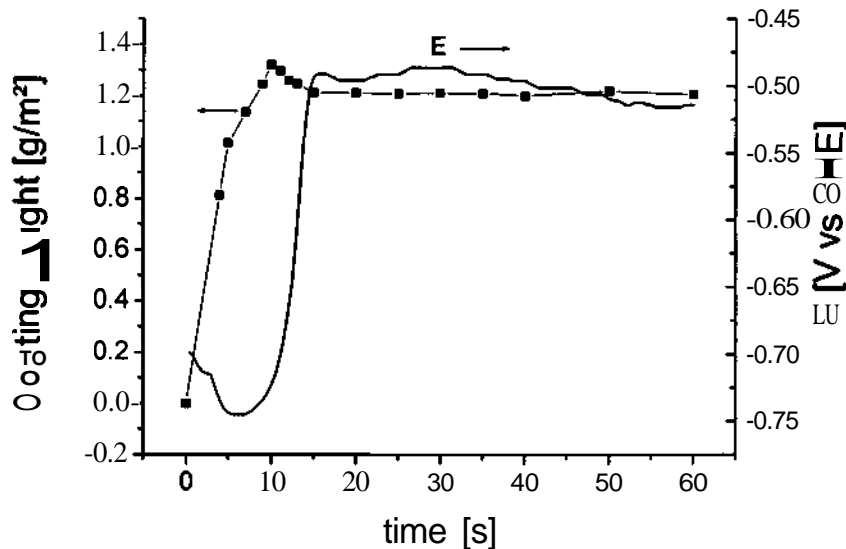


Figure 49: Development of phosphate coating weight with time and open circuit potential during reaction for a trication phosphating bath. Each point in time for the coating weight was measured on a different sample.

Cyclic **voltammetry** was used to follow the decrease of the free zinc area with phosphating time. In this method the phosphate surface is polarised in a borate buffer. The free surface of zinc is considered proportional to the integral of the zinc oxidation peak. Figure 50 shows a cyclic voltammogram obtained on a pure zinc layer on steel and on the same layer after trication phosphating. The decrease of free surface of zinc is clearly seen in the voltammogram.

The trication phosphating was carried out under room temperature without activation to slow down the reaction for a better time resolution. For each point in time a different sample was used, and a minimum of three cyclic voltammograms were measured per sample. Figure 51 shows the potential transient and the trend of the charge density of the oxidation peak with time. At the beginning there is an increase in the oxidation current most probably to dissolution of zinc oxide layer and roughening of the surface due to the pickling attack of the acidic phosphating solution. After about 40 s the peak current begins to increase and reaches a minimum at the same time the potential

step occurs. This again shows that the potential step occurs at, or slightly after the minimum in surface coverage. Further increase in current density is due to redissolution of phosphate crystals on the substrate.

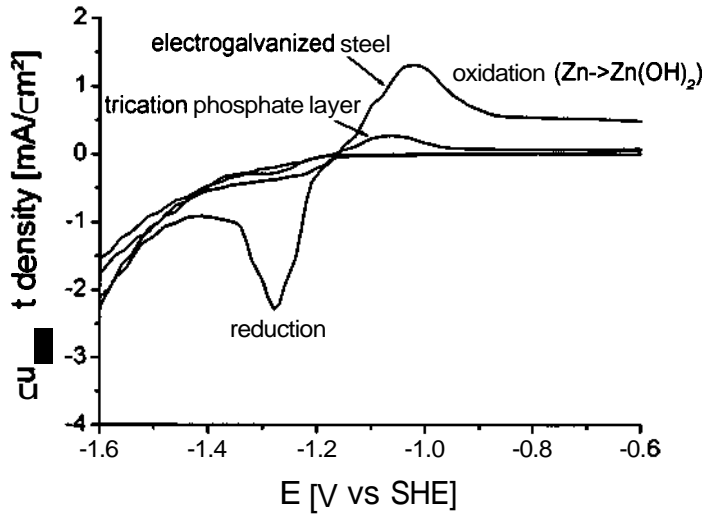


Figure 50: Cyclic voltammograms of zinc coated steel and trication phosphate layer in a 0.3 M boric acid solution (pH = 9).

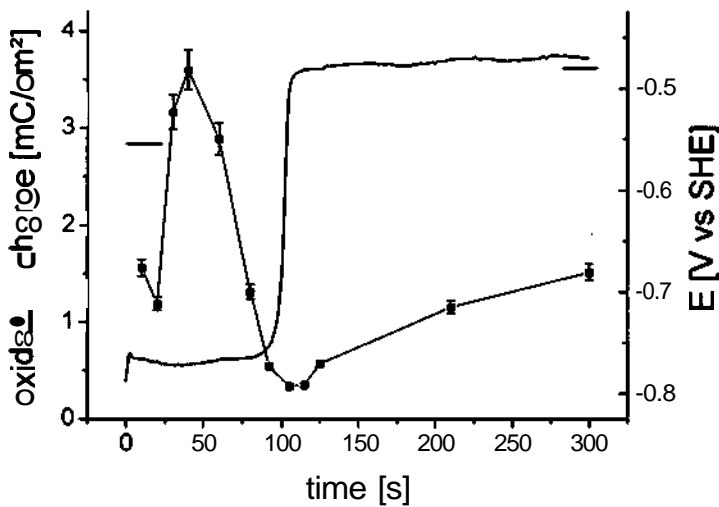


Figure 51: Development of oxidation charge of zinc oxidation in cyclic voltammetry experiments with time of phosphating and according potential transient (trication phosphate bath at room temperature without activation was used to get suitable time resolution for experiments)

Figure 52 shows the potential transients for three different accelerators. It is clearly seen that, under the conditions of these experiments,  $t^{\circ}$  decreases in the following order : No accelerator > hydroxylamine > nitrobenzoic acid > nitrate. The accelerating effect of the different accelerator species is clearly seen. With this type of experiment it can also

be shown that the reaction rate of a hot dip galvanised layer is slightly decreased compared to an electrogalvanised zinc layer (Figure 53). This is explained by the additional required pickling reaction of the aluminium oxide layer, which is present on the surface of hot dip galvanised layers. The hot dip galvanised coating is quite different from the electrogalvanised in that it could contain Al in the range 0.1 - 0.3 %. It should be noted that the galvanised steel surface in this experiment had not undergone the usual skin pass, which is a process treatment in which a certain roughness is "stamped" onto the coated steel product. It is generally accepted that this process increases the quality of phosphate coatings by breaking up oxide islands.

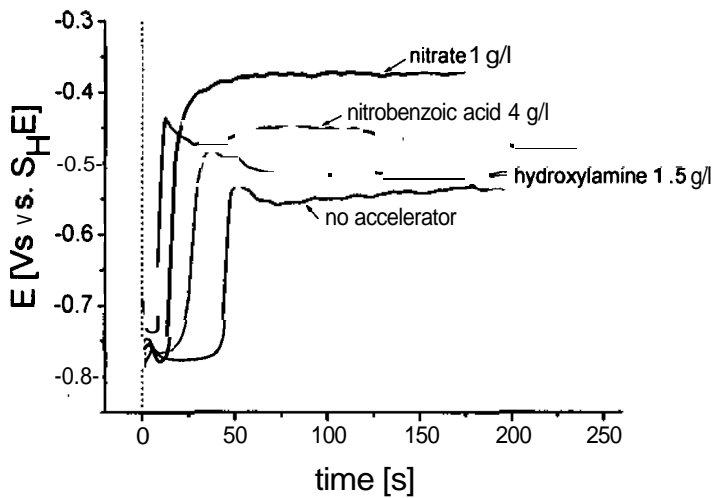


Figure 52: Potential vs. time transients for the phosphating of electrogalvanised steel, measured with different accelerating agents in the phosphating bath (trication).

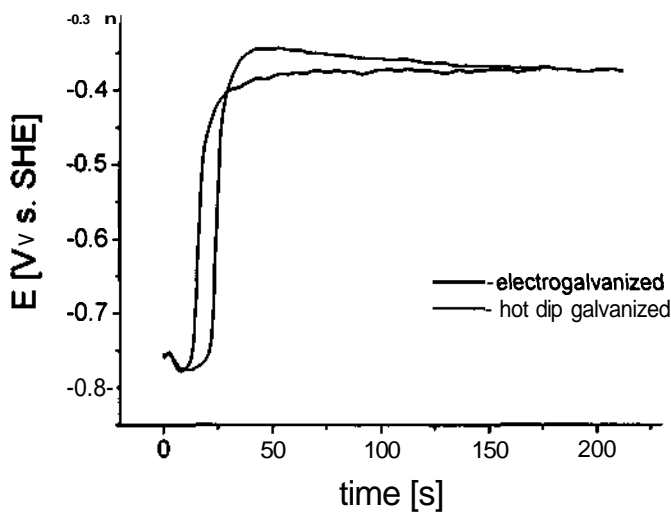


Figure 53: Potential vs. time transients for the phosphating of electrogalvanised and hot dip galvanised steel in a trication bath accelerated with nitrate (1 g/l).

## 6.3 KINETICS OF PHOSPHATING WITH QUARTZ CRYSTAL MICROBALANCE

The idea of these experiments was to follow the phosphating reaction on the zinc surface of the **quartz**. The growth of phosphate film results in significant changes in surface roughness and water trapped between the crystals will contribute to the mass changes (see chapter 3.2.4 p. 27). However, qualitatively, these experiments do yield some interesting information allowing us to observe different kinetic periods.

### 6.3.1 EXPERIMENTAL

The kinetics of phosphating were examined with the **QCM** and simultaneous measurement of the open circuit potential (**OCP**). The **ICP spectroelectrochemistry** system could not be used to independently measure the zinc dissolution rate because of the large concentration of zinc already present in the phosphate bath. The temperature of the solution in the beaker was controlled and the path to the flow cell was kept as short as possible. The temperature of the phosphating bath in contact with the quartz may therefore be slightly lower than the adjusted temperature in the beaker. The composition of the phosphating solutions for these studies is shown in Table 9

Solution		NaNO <sub>3</sub> [g/l]	Mn(NO <sub>3</sub> ) <sub>2</sub> x 4H <sub>2</sub> O [g/l]	Ni(NO <sub>3</sub> ) <sub>2</sub> x 6H <sub>2</sub> O [g/l]	accelerator
A	Monocation sample	-	-	-	-
B	+ NO <sub>3</sub> <sup>-</sup>	12	-	-	-
C	+ NH <sub>2</sub> OH	-	-	-	3 g/l NH <sub>2</sub> OH (50%)
D	+ H <sub>2</sub> O <sub>2</sub>	-	-	-	1 ml/l H <sub>2</sub> O <sub>2</sub> (30%)
E	trication +NO <sub>3</sub> <sup>-</sup>	6	4.6	5	-

Table 9: Composition of phosphating bathes used for QCM-studies added to a base electrolyte of 11 m/l 85% H<sub>3</sub>PO<sub>4</sub> and 1.25 g/l ZnO. Free acid was adjusted to 2. H<sub>2</sub>O<sub>2</sub> was added immediately before the experiment.



### 6.3.2 RESULTS AND DISCUSSION

#### *The Effect of $Mn^{2+}$ and $Ni^{2+}$*

Figure 54 shows the mass transient and the open circuit potential obtained with a nitrate-accelerated monocation bath (solution B) at 55 °C. Note that the OCP is shown vs. the saturated calomel electrode SCE (0.2418 V vs. SHE). These results are very similar to the phosphating reactions observed in previous publications [80, 81].

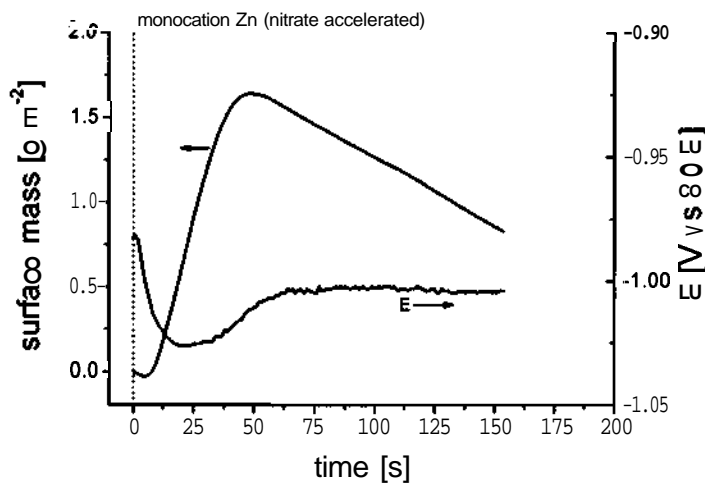
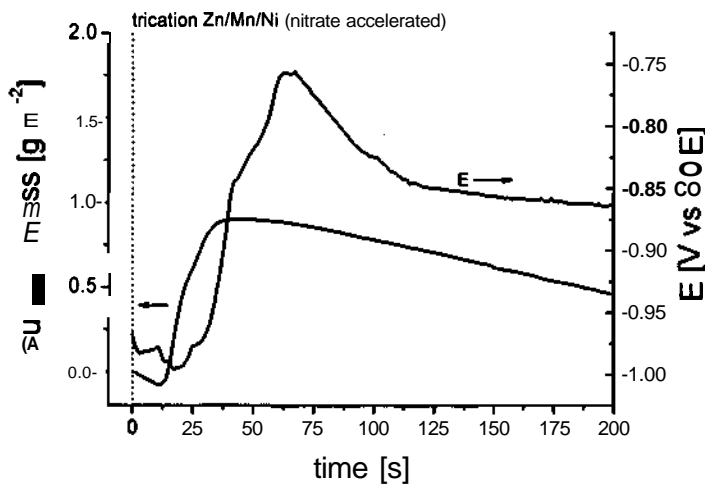


Figure 54: **Effect of  $Mn^{2+}$  and  $Ni^{2+}$**

Mass transient (QCM) and OCP during phosphating of zinc coated quartz with a monocation (A - Solution B) and trication bath (B - Solution E) using nitrate as accelerator) at 55°C.

A



B

The shape of the mass transients may be divided into three periods of time:

- 1 Initial Mass Loss** The mass curve begins with a short period of a very low mass loss (appr.  $0.03 \text{ g/m}^2$ ) in the first 6 s of the reaction. This period is also accompanied with a drop of the open circuit potential starting from  $-0.98 \text{ V}$  (vs. SCE). The reaction taking place may be characterised by the dissolution of an oxide layer on the coating and the pickling of the metal in the acidic solution. Metal dissolution remains the predominating electrochemical reaction, which determines the open circuit potential.
- 2 Rapid Mass Increase** After appr. 25 s the **OCP** rises again from  $-1.025 \text{ V}$  to  $-1 \text{ V}$  vs. SCE. In that period a strong mass gain on the surface takes place undoubtedly due to the precipitation of the phosphate.
- 3 Slow Mass Decrease** After the maximum of mass is reached, there is a **slow** decrease in mass. This is probably due to corrosion of the metal substrate exposed in between the crystals and/or redissolution of the phosphate crystals. The second is likely since the passivation of the surface will result in a slow reacidification of the **interfacial** region.

It is interesting to note that the maximum of the mass at 48 s nearly coincides with the point of inflection of the potential rise. Since the phosphating reaction is a mixed process with anodic metal dissolution and cathodic reduction of hydrogen ions or an accelerating agent, a rise in the potential indicates a change in the current-potential characteristics of the half-reactions. This is the case, when the surface is partially passivated by the phosphate crystals.

Figure 54B shows the result for a trication phosphating bath (Solution E) under the same conditions as shown in Figure 54A. We see that the maximal value mass is approximately  $0.7 \text{ g/m}^2$  ( $0.9 \text{ g/m}^2$  lower compared to the monocation phosphating bath). These is in agreement with the observations on technical samples, where Mn and Ni in the phosphating bath lead to a refinement of the phosphate crystals and to a lower coating weight. Apart from that, the mass transients show a similar form as that of the monocation bath in Figure 54A. There is an increased reaction rate indicated by the reach of the maximum mass at 35 s. (about **15 s** earlier compared to the monocation bath). The period after the stop of phosphate layer formation shows a much lower mass loss rate. This can be attributed to the presence of metallic nickel, which cementates in the free pores of the phosphate layer and protects the zinc underneath.

Nickel cementation is also indicated by the anodic shift of the **OCP**. We used this distinct shift already in chapter 6.2 for following the kinetics of **phosphating** on technical samples. However, the potential transient in the QCM experiment looks different, showing two stages of the shift with different slopes and falling back to **-0.85 V** vs. SCE at 100 s after reaching its maximum of **-0.75 V** at 65 s. The specific flow conditions in the QCM cell as well as the surface condition of the zinc coated quartzes may be responsible for the different behaviour compared to technical samples.

### ***The effect of accelerators***

Figure 55 shows the mass transients during phosphating with a monocation bath containing various accelerators (Figure 54B is shown again for comparison). A bath containing no accelerator (Figure 55A) does not give rise to a noticeable mass increase during the reaction. The predominant reaction is zinc dissolution shown by a steady OCP of around **-1.064 V** vs. SCE. The rate of the mass loss calculated by linear regression is **-0.00175 gm<sup>-2</sup>s<sup>-1</sup>**.

Similar results were obtained for the hydroxylamine accelerated solution (Figure 55C). Again there is no mass gain observed. The rate of mass loss (**-0.00153 g/m<sup>2</sup>s**) is quite similar compared to the bath without any accelerator. The concentration of **1.5 g/l NH<sub>2</sub>OH** may be too low to observe similar transients as in nitrate accelerated bathes. However, deposition of a phosphate layer could have taken place on the quartz, but it was not possible to determine the coating weight.

By adding **H<sub>2</sub>O<sub>2</sub>** to the phosphating solution (Figure 55D) just before the experiment, the reaction proceeds in the usual way as already observed with the nitrate accelerated bath, but with some differences. The initial phase of a noticeable mass loss is missing. The maximum value of mass is reached after appr. 50 s, not earlier than in the nitrate accelerated bath, but the surface mass is only half the value (**0.8 g/m<sup>2</sup>**). Again the point of inflection of the open circuit potential coincides with the maximum of the mass transients.

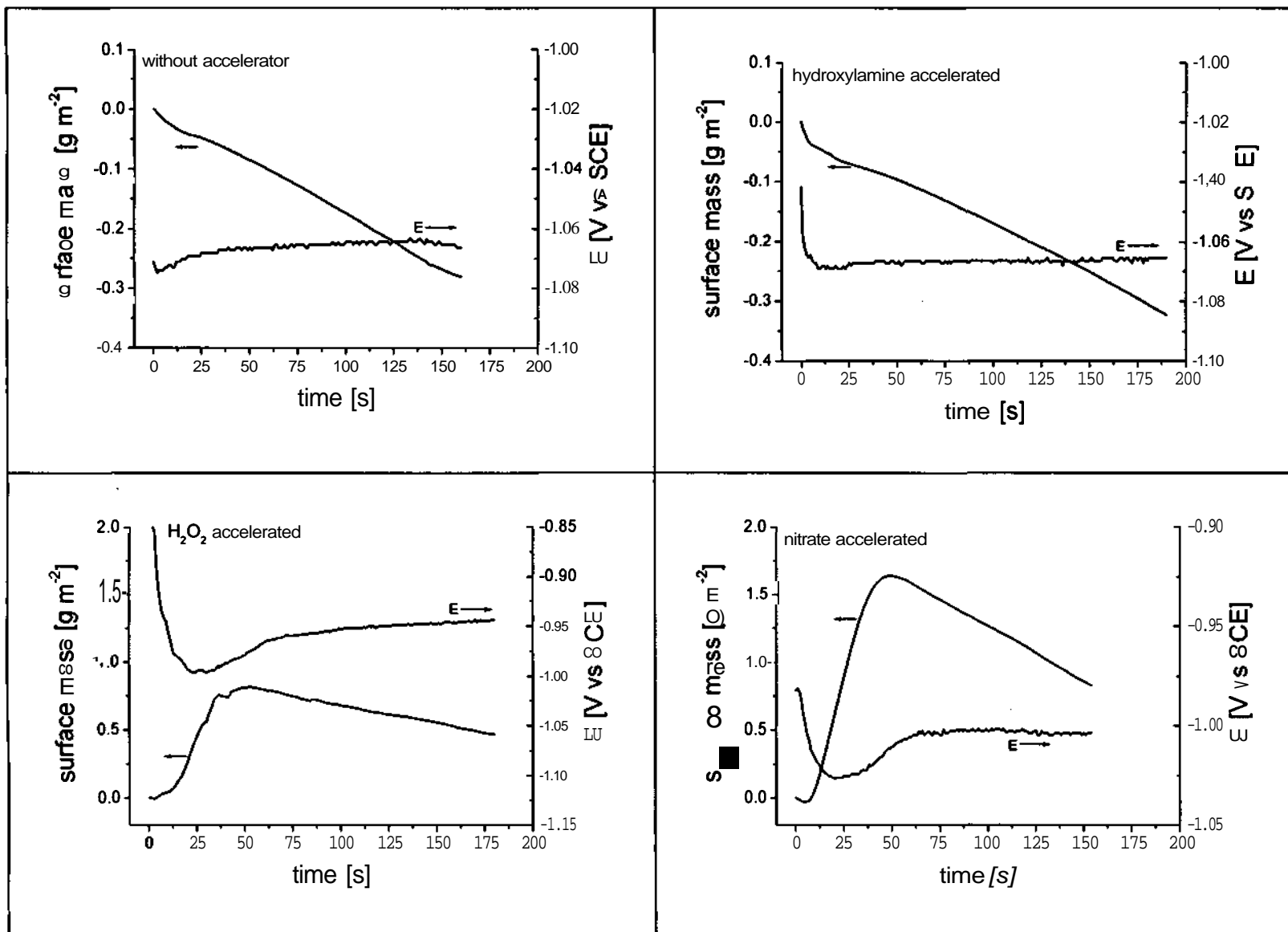


Figure 55: Effect of accelerator-Mass (QCM) and OCP transients during phosphating of zinc coated quartz in a monocation bath at 55°C using different accelerators as indicated.

### **Temperature dependence**

Figure 56 shows mass transients obtained during monocation phosphating ( $\text{NO}_3^-$  as accelerator) at different temperatures. All curves show the characteristic shape of the mass transient and the course of the open circuit potential. There is clear relationship between temperature and time of reaction as indicated by the time at which the maximum mass value is reached as well as the inflection point in the shift of the OPC. The time of the maximum mass goes from 230 s at 25 °C, 105 s at 35 °C, 50 s at 55 °C and 40 s at 70 °C. This is in good agreement with Arrhenius' law. The shape of the potential transients has the same look for all temperatures, but the absolute values of the OCP decrease with increasing temperature (e.g. the minimum potential value at room temperature is -1.008 V and at 70 °C it is -1.045 V vs. SCE). This is in excellent agreement with the calculated temperature dependence for the electrochemical standard potential of the  $\text{Zn}/\text{Zn}^{2+}$  half reaction ( $-0.0008 \text{ V K}^{-1}$ ).

The lowest coating weight (maximum mass value) is obtained at 55 °C. Obviously there is an optimum temperature for getting low phosphate coating weights. It is known, that the solubility of hopeite decreases with increasing temperature. Therefore the overall reaction is quicker at elevated temperatures, but may lead to higher precipitation rate, increasing also the coating weight.

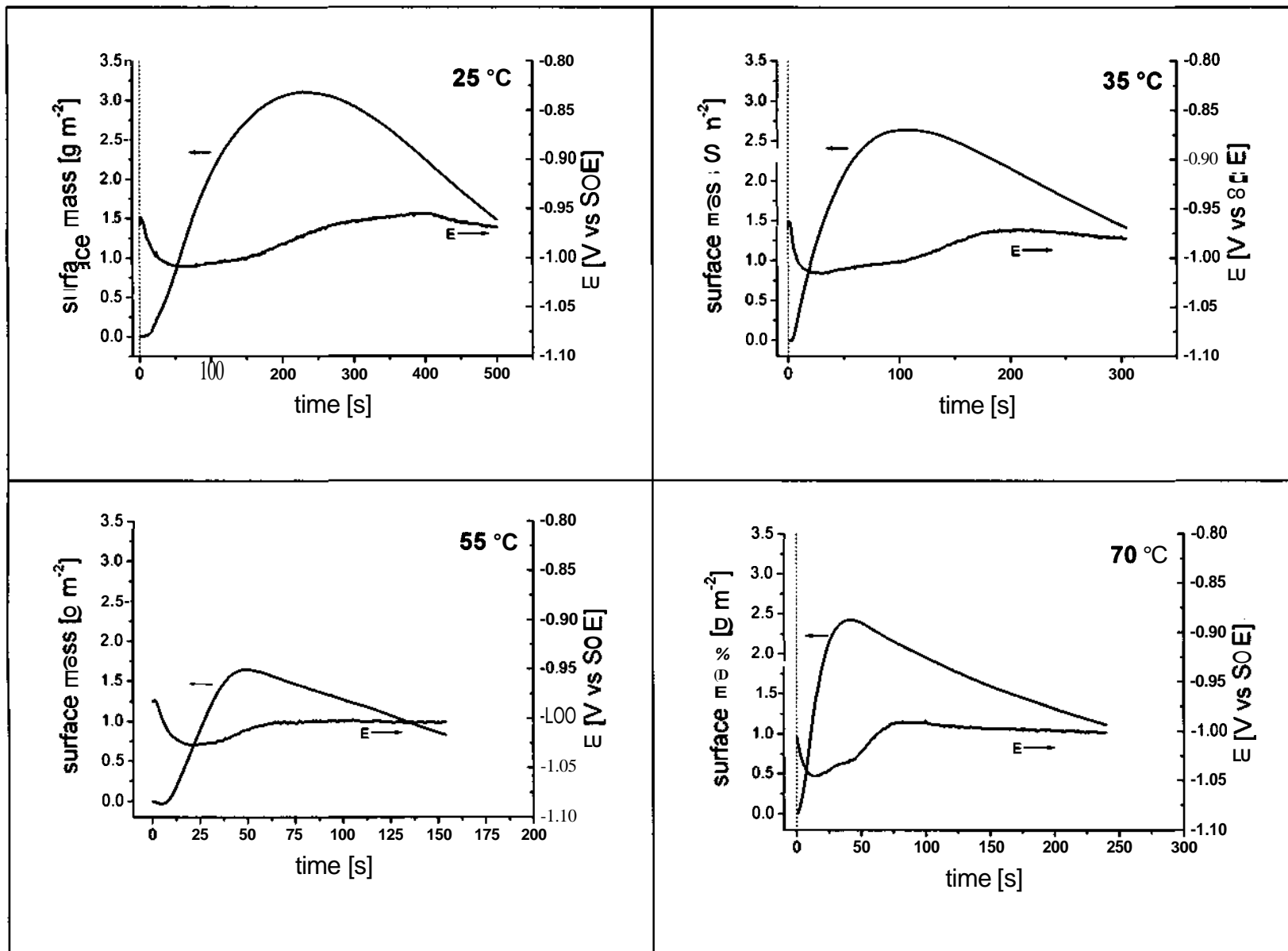


Figure 56: **Effect of temperature** - Mass (QCM) and OCP transients during phosphating of zinc coated quartz in a monocation with nitrate accelerator (Solution B) at various temperatures as indicated.

## 6.4 ANODIC DISSOLUTION OF ZINC IN THE PRESENCE OF ACCELERATORS (QCM-ICP)

The idea of these experiments was to conduct similar experiments as described in chapter 6.2, using synthetic phosphate solutions containing accelerator but no metal ions. The results of this chapter were based upon **OCP** measurements and it was therefore interesting to confirm this result with the **QCM** method. In addition, this permits a use of the combined QCM-ICP technique so that a quantitative comparison of the two methods is possible.

### 6.4.1 EXPERIMENTAL

The anodic dissolution rate of zinc in phosphoric acid solutions containing different accelerators was measured using the combined QCM and **ICP-AES** experiment at room temperature. For this purpose zinc coated quartzes were attacked by solutions similar to a phosphating bath containing no zinc. The base solution is phosphoric acid (11 ml/l  $\text{H}_3\text{PO}_4$  85%). Detailed composition of the applied solutions is shown in Table 10. The free acid was adjusted to 2 for all solutions. Hydrogen peroxide was added just before the start of the experiment.

Solution		addition of
A2	Without accelerator	-
B2	with nitrate	+ 1.37 g/l $\text{NaNO}_3$ (1 g/l nitrate)
C2	with $\text{H}_2\text{O}_2$	+ 1 ml/l 30% solution of $\text{H}_2\text{O}_2$
D2	with hydroxylamine	+ 3 g/l 50% solution of $\text{NH}_2\text{OH}$

Table 10: Composition of phosphoric acid solutions used for accelerator experiments. Base solution was 11 ml/l  $\text{H}_3\text{PO}_4$  85 %.

Figure 57 - Figure 63 show the results of these experiments. The upper graph (A) in each case shows the dissolution transients of Zn as measured with the **ICP-flow** analysis and the open circuit potential (vs. SCE) during the reaction. The lower graph (B) shows the mass transients as received by the QCM (black curve) and calculated from the **ICP-data** by integration of the leaching rate of Zn (red curve). The grey curve shows the difference of QCM and **ICP** mass.

#### 6.4.2 RESULTS AND DISCUSSION

*No ACCELERATOR (SOLUTION A2)* - In the absence of any accelerator (Figure 57A) the dilute phosphoric acid results in an Zn dissolution rate of approximately  $2 \text{ nmol cm}^{-2} \text{ s}^{-1}$  which increases slowly with time, reaching  $5 \text{ nmol cm}^{-2} \text{ s}^{-1}$  after 400 s.

The mass loss on the surface obtained with the QCM (Figure 57B) is in excellent agreement with the calculated data from the ICP leaching rate. The amount of Zn removed after 400s is appr.  $5 \text{ g/m}^2$ . There are no signs of a reaction causing mass gain (e.g. formation of a phosphate layer) taking place in this solution. Additionally the course of the open circuit potential remains constantly on the **Zn-potential** in acidic solution and does not give any indication of passive film formation.



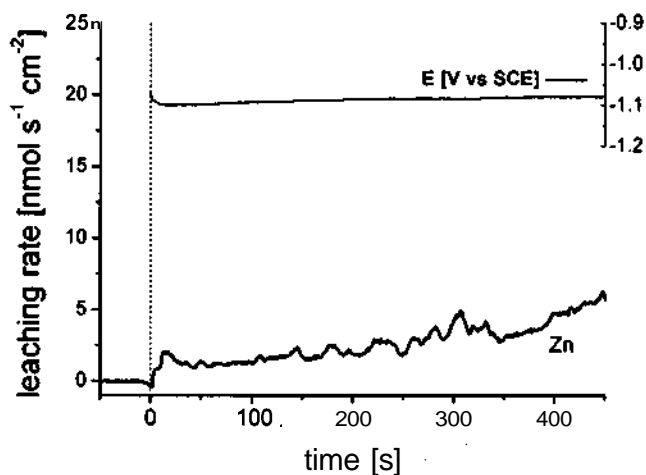
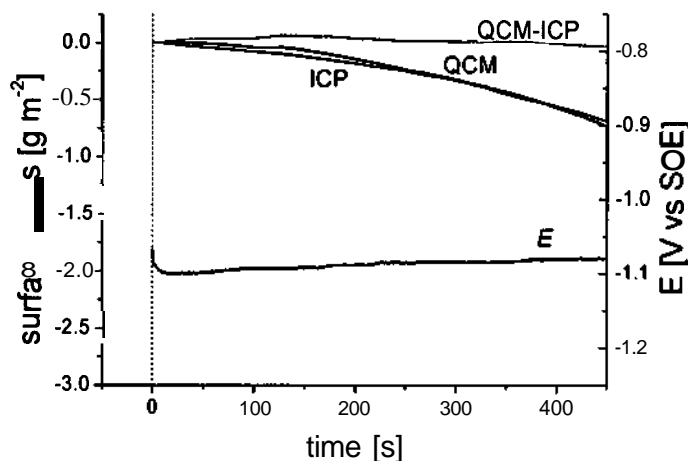


Figure 57:

A: ICP leaching rate and OCP on zinc in a phosphoric acid solution (A2) **without** an accelerating agent.



B: Mass transients as received with the QCM and calculated from the ICP-data. A good correlation is observed between the QCM and the ICP data.

*NITRATE (SOLUTION B2)* - In presence of  $\text{NO}_3^-$  (1 g/l) (Figure 58) without activation, the zinc dissolution rate is significantly increased, obtaining a value of  $15 \text{ nmol cm}^{-2} \text{ s}^{-1}$  after 150 s. QCM data reveals a lower mass loss as the amount of zinc detected with the ICP-AES. Some precipitation of phosphate on the surface may be responsible for that discrepancy although other possibilities might be invoked such as a localised zinc dissolution. The open circuit potential is slightly more anodic (60 mV) in presence of nitrate than in a pure phosphoric acid solution due to its depolarising effect. However, there is no clear anodic shift of the potential during the reaction, which would indicate a partial passivation of the **surface**.

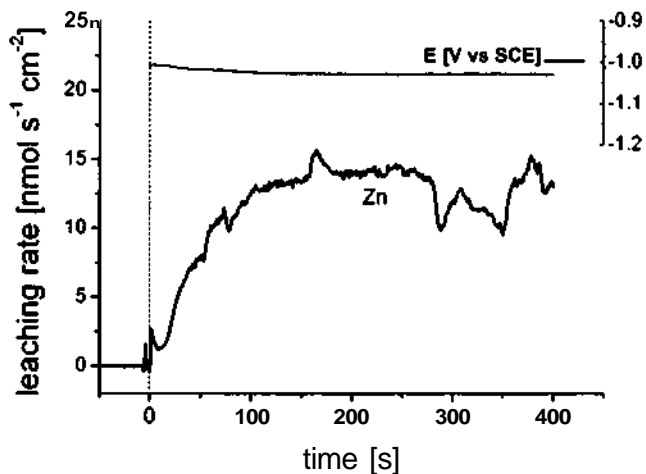
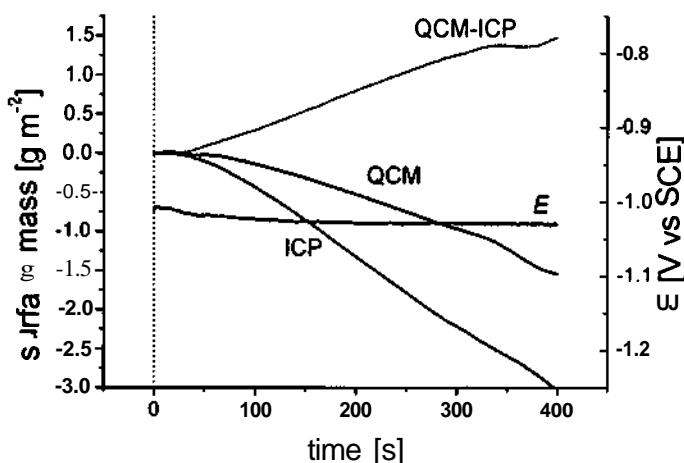


Figure 58:

A: ICP leaching and OCP on zinc in a phosphoric acid solution (B2) with nitrate as accelerator (non-activated surface)



B: Mass transients as received with the QCM and calculated from the ICP-data. The QCM and ICP yield markedly different dissolution rates suggesting the formation of a surface film.

Figure 59 shows the results of an experiment using the same solution as in Figure 58 (nitrate accelerated), but obtained after dipping the zinc coated quartz into an activating solution (5% Fixodine 50CF) before the reaction with phosphoric acid. The zinc leaching rate is approximately  $10 \text{ nmol cm}^{-2} \text{ s}^{-1}$  and starts to decrease at 50 s after an initial quick rise. The rate reaches a minimum around 100 s and then increases again reaching the original value of the initial attack.

The QCM curve of Figure 59B is very similar to the one obtained during phosphating of a zinc coated quartz as shown in chapter 6.3.2, showing definite periods of initial mass loss, a period of rapid mass gain, and a final period of mass loss. Interestingly, the ICP and the QCM are in good agreement during the periods of net mass

loss (first 50 s and after 200 s), demonstrating that this technique is valid. The period of mass gain occurs simultaneously with the decrease in dissolution rate. The open circuit potential clearly shows a partial passivation by increasing steadily after the minimum at 150 s as was observed for the phosphating of zinc in the previous section.

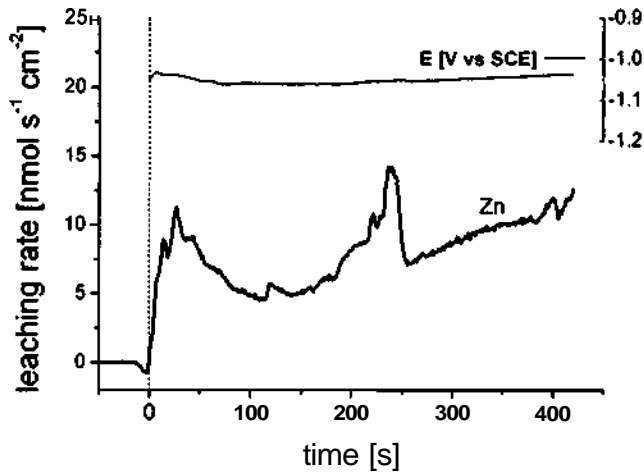
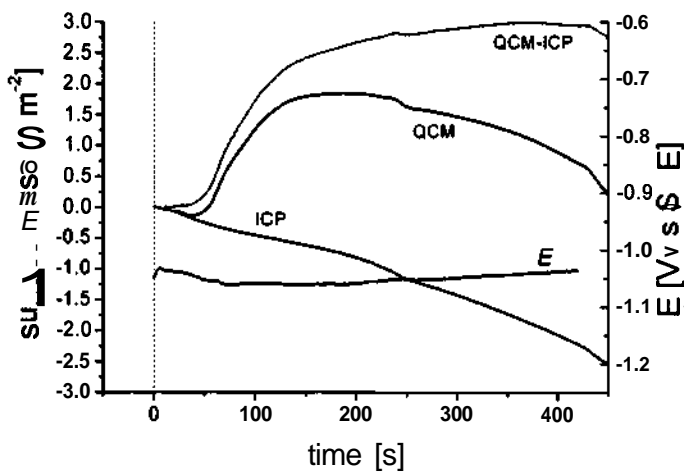


Figure 59:

A: ICP leaching rate and OCP on activated zinc in a phosphoric acid solution (B2) with **nitrate** as accelerator (**activated surface**)



B: Mass transients as received with the QCM and calculated from the **ICP-data**. Film formation is clearly observed by the rapid increase in mass.

Before and after the mass increase, the ICP and QCM give very similar rates of reaction.

**HYDROXYLAMINE (SOLUTION C2)** - The results with hydroxylamine (Figure 60) as accelerators are very similar to those obtained in the absence of accelerator. The zinc leaching rate is slightly lower therefore, no oxidising effect is observed. This is also confirmed by the QCM data. The QCM and the ICP show only a slight difference, and although this difference is consistent with film formation, given the difficulty of calibration, it should not be taken into account. Further, the open circuit potential is consistent with zinc dissolution in acidic environment. Open circuit potential starts at rather low values (-1.1 V vs. SCE). There is no anodic shift in the potential as observed in presence of nitrate. For this solution, activation of the **surface** does not seem to alter the dissolution kinetics in any significant way (Figure 61).

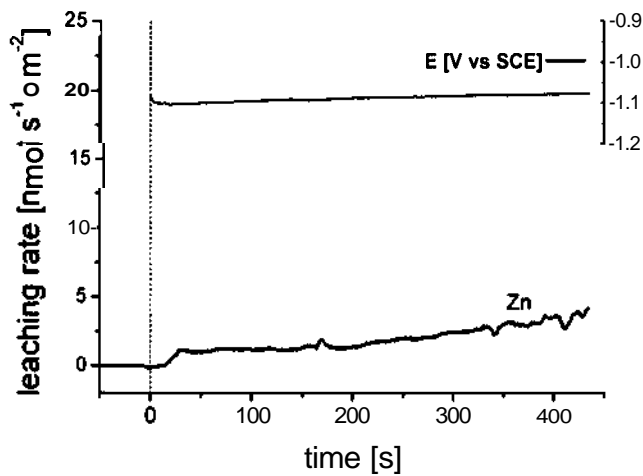
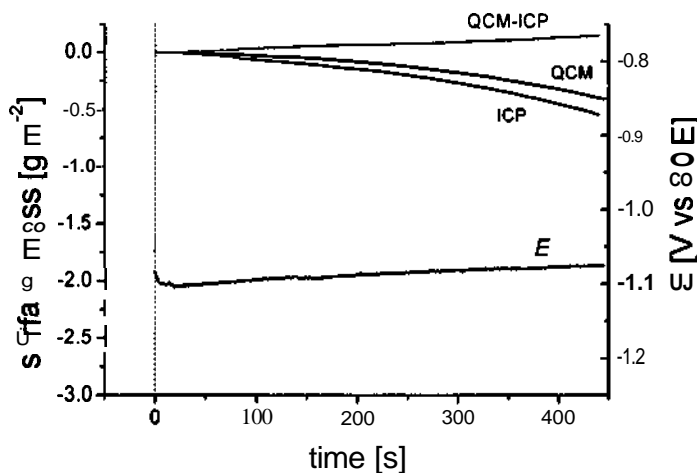


Figure 60:

A: ICP leaching rate and OCP on zinc in a phosphoric acid solution (C2) with **NH<sub>2</sub>OH** as accelerator (**non activated surface**).



B: Mass transients as received with the QCM and calculated from the ICP-data. Similar ICP and QCM results are obtained.

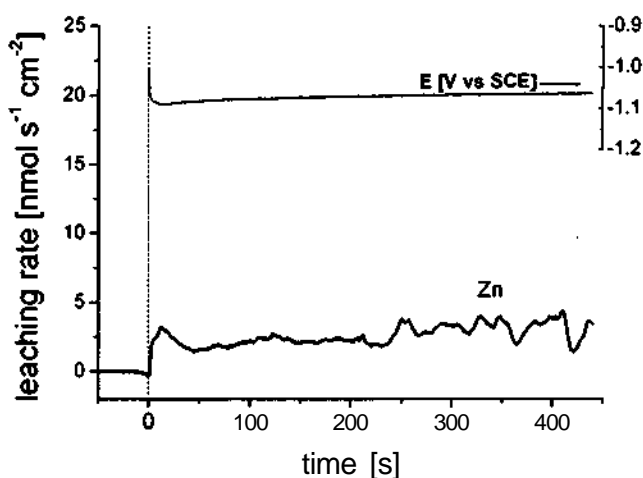
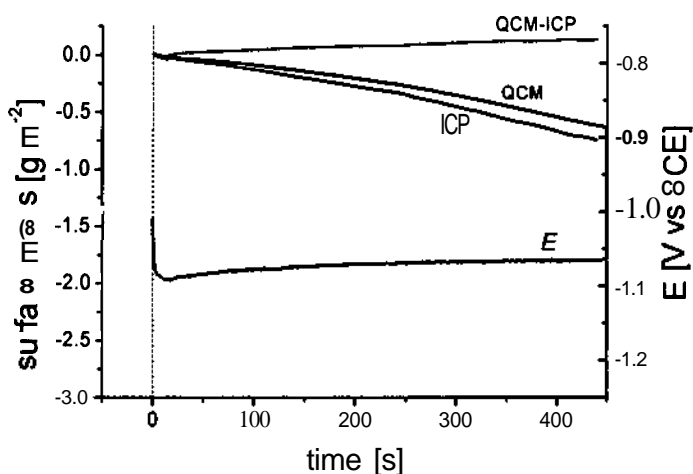


Figure 61:

A: ICP leaching rate and OCP on activated zinc in a phosphoric acid solution (C2) with  $\text{NH}_2\text{OH}$  as accelerator (activated Surface)



B: Mass transients as received with the QCM and calculated from the ICP-data.

*HYDROGEN PEROXIDE (SOLUTION D2)* - By adding hydrogen peroxide to the dilute phosphoric acid (Figure 62) layer formation takes place on the surface even without activating. This is clearly indicated by the mass transients obtained with QCM and the course of the open circuit potential. The dissolution rate is rather constant at  $12.5 \text{ nmol cm}^{-2} \text{ s}^{-1}$  after an initial phase of approximately 30 s. The mass on the surface reaches a maximum at 120 s, which coincides with the point of inflection in the open circuit potential, as already observed in the experiments on the phosphating kinetics using QCM only. However, the dissolution rate of Zn is not affected by the layer formation and remains nearly constant as time of reaction goes on. The mass decreases after the maximum may be due to redissolution of the layer or more likely due to Zn dissolution.

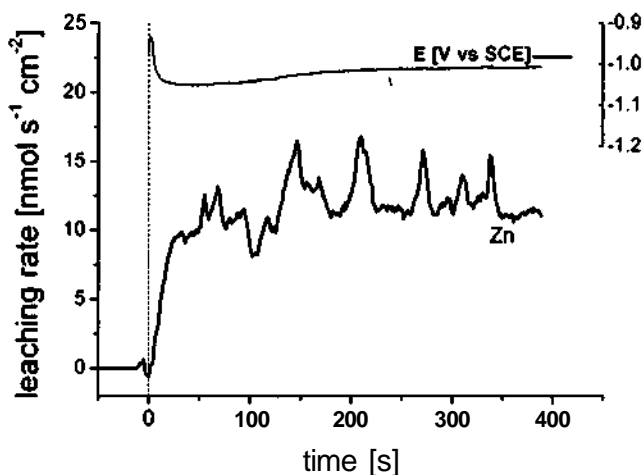
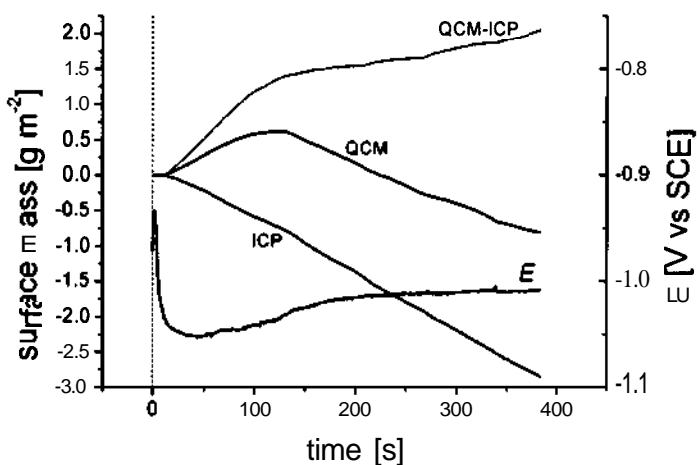


Figure 62:

A: ICP leaching rate and OCP on zinc in a phosphoric acid solution (D2) with  $\text{H}_2\text{O}_2$  as accelerator (non activated surface).



B: Mass transients as received with the QCM and calculated from the ICP-data.

Figure 63 shows the results in an  $\text{H}_2\text{O}_2$ -accelerated solution after activating the zinc surface of the quartz. The picture is not changed very much compared to the results without activating (Figure 62). As observed with  $\text{NH}_2\text{OH}$ , the Zn dissolution is increased slightly on an activated surface. (average values of around  $17.7 \text{ nmol cm}^{-2} \text{ s}^{-1}$ ). QCM transients and open circuit potential again indicate the formation of a layer, which does not affect the overall Zn dissolution rate. These results confirm that surface film formation takes place when  $\text{H}_2\text{O}_2$  is present.

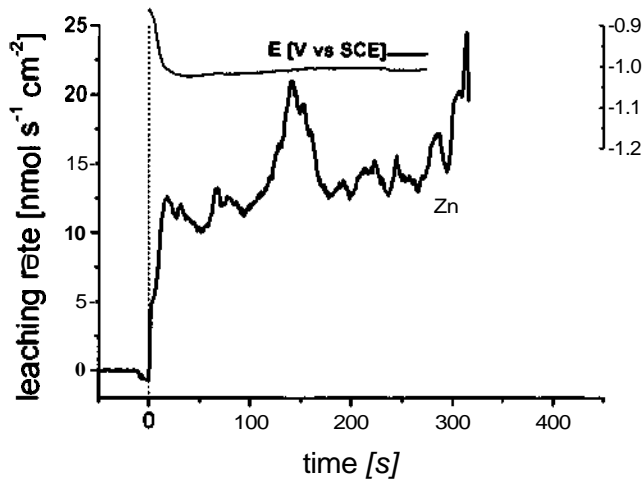
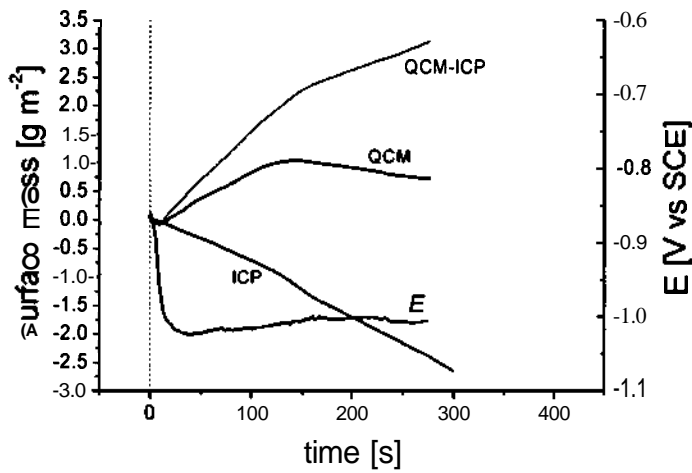


Figure 63:

A: ICP leaching rate and OCP on zinc in a phosphoric acid solution (D2) with  $\text{H}_2\text{O}_2$  as accelerator (activated surface).



B: Mass transients as received with the QCM and calculated from the ICP-data.

## 6.5 CONCLUSION

The dissolution-precipitation mechanism of the phosphating reaction (see chapter 2.3.3.1) could be easily investigated with the QCM technique and with electrochemical techniques like the cyclic voltammetry. The influence of added cations and accelerating substances could be determined qualitatively and to some extent quantitatively.

The combination of **ICP** and the QCM provides a powerful technique for the investigation of the kinetics of zinc dissolution in presence of various oxidising substances. Especially, the formation of a layer as indicated by a mass gain in the QCM experiment could be confirmed, which would not be possible by measuring the Zn dissolution with the ICP only. In this context classic oxidising agents like nitrate and hydrogen peroxide were found to be promoters of zinc dissolution and also lead to precipitation of a layer even in the synthetic phosphate solutions containing no metal cations, which are usually required for film formation.



## 7 SUMMARY

A combination of three major techniques (Raman spectroscopy, ICP-AES and QCM) was applied to the investigation of the phosphating reaction on zinc coated steel. The chemical stability of such layers as well as the kinetics of the surface treatment itself were of particular interest.

### 7.1 ALKALINE STABILITY

The reaction of phosphate layers on metal surfaces (zinc coated steel and cold rolled steel) with 0.1 M NaOH solution was investigated with Raman spectroscopy, ICP-AES and QCM (coupled with the ICP technique). All three techniques worked well and were suitable for this type of experiments. With the different methods, it was possible to obtain complementary information about the detailed mechanism. Moreover a model of the reactions occurring during the attack could be easily developed and confirmed.

According to this model, the phosphate layer is dissolved by an  $\text{OH}/\text{PO}_4^{3-}$  ion exchange in the initial phase of the attack. A zinc hydroxide layer remains, which is dissolved with increasing time of reaction. In the final state of the reaction pure substrate dissolution (in the case of Zn) is the prevailing reaction, which is indicated by the OC potential. The rate of Zn dissolution in an oxygen free solution is nearly zero, whereas in presence of air this rate is distinctly increased and hence suggests an increase of the phosphate leaching by a mechanism of anodic undermining.

Metal cations like Mn and Ni were found to reduce the reaction of the phosphate layer with the alkaline solution. In particular, Mn shows a pronounced tendency in increasing the alkaline stability due to its high concentration (~5%) in the crystals. The effect of Ni was less pronounced and this can be attributed to its lower concentration in the crystals (~1.5%). However, the cementation reaction of Ni in the free pores of the phosphate layer proved to be an **important** factor for the anodic protection of the zinc during corrosive attack.

During the alkaline attack Mn and Ni remain on the **surface** and form a stabilised mixed hydroxide layer, which is assumed to protect the phosphate from further dissolution

and thus reduces the overall leaching rate. The formation of a Mn-hydroxide layer was particularly confirmed by Raman spectroscopy data. The Raman technique specifically is limited by generally low intensities in case of in situ experiments. Phosphate layers, however produced sufficient intensity for this type of experiments. For the examination of alternative treatments some modification in order to further increasing of the intensity may be necessary.

The behaviour of the open circuit potential during the reaction could not be related to the stability of the layer, but revealed information about the activity of the bare metal surface under and between the phosphate crystal and therefore provided a valuable contribution to the elucidation of the reaction mechanism.

The likewise conducted scab corrosion tests showed the best corrosion resistance for phosphate layers containing both Mn and Ni. However, although Mn was found to increase the alkaline stability of the layer by a factor of 3 (concerning maximum dissolution rate in the **ICP**) its influence on the corrosion resistance was much lower than that of Ni. This leads to the conclusion, that during scab corrosion of painted and zinc coated steel the anodic zinc dissolution mechanism is predominating and therefore renders the alkaline stability of the phosphate layer less important. The detailed corrosion mechanism of zinc coated steel is not fully understood and still is a topic for further studies.

Generally the results of these experiments allow to assess the influence of the added cations in modern phosphating bathes and enables further progress in developing of surface treatments, as it showed important parameters, which may play a major role for a good performance of a conversion layer.

## 7.2 KINETICS OF PHOSPHATING REACTION

The kinetics of the phosphating reaction on zinc coated steel, particularly the influence of oxidising agents added to the bathes, were examined by means of electrochemical experiments, **ICP-AES** and QCM (coupled to the ICP).

Potential vs. time transients were useful experiments to determine the time of the phosphating reaction. In presence of Ni these transients exhibit a distinct potential jump, which happens at the same time as the coating weight reaches constant values. With

these technique various accelerators were tested and it was found the reaction rate was highest in solutions containing nitrobenzoic acid, followed by nitrate and hydroxylamine.

Cyclic **voltammetry** was used to determine the free active zinc area between the phosphate crystals. The experiments showed a maximum coverage of the metal surface by phosphate crystals happening at the same time as the potential change occurred. This is again a proof for the usefulness of OC transients in measuring the time required for phosphate layer formation.

The surface mass on the zinc during **phosphating** was determined by **QCM** experiments. In general, the mass transients showed three distinct periods, indicated by an initial mass loss followed by a rapid mass gain until the mass decreases again after reaching a maximum value. Also for this case the efficiency of the accelerator was tested and similar results as with the simple OC transients were obtained. The rate of the phosphating reaction as indicated by the mass transients and the OCP increased with temperature according to thermodynamics, whereas the maximum value in coating weight (by QCM) showed a minimum at 55 °C.

The anodic dissolution of zinc in synthetic phosphating solutions containing no metal cations was investigated with the coupled **ICP-QCM** technique. With this method the rate of zinc dissolution could be measured as well as the mass transients during the reaction. Solutions containing nitrate and  $\text{H}_2\text{O}_2$  as oxidising agents lead to a layer formation on the surface indicated by a mass gain in the QCM data even without zinc in the bath. In addition to that, the rate of zinc dissolution is also increased in presence of these substances. Hydroxylamine was found to exert no strong influence on the rate of zinc dissolution.

In general, the results of the various techniques were in good agreement and enabled improved understanding on the mechanism of the phosphating reaction.

### 7.3 OUTLOOK

The results of the experiments in this work helped to elucidate important factors for the surface treatment of metals. The applied techniques, which are new in the area of **phosphating**, proved to be very suitable in this type of studies and certainly will be valuable tools in the investigation of other, recently developed surface treatments as well. In particular, the driving forces in developing new phosphating processes aim to eliminate environmentally critical substances like Ni-cations or nitrite. On basis of the results obtained in this work a contribution to a better understanding of the mechanism of added cations and oxidising agents could be achieved. The findings and conclusions of this work can serve as basis for further development and application of other additives to phosphating and alternative surface treatments as well.

## 8 LITERATURE

- 1 W. Rausch "The phosphating of metals", Finishing publications, LTD. 1990, Teddington, England
- 2 K. Ogle, R. Bucheit "Conversion Coatings" in *Encyclopedia of the Electrochemistry*, Vol 5 Ed. A. J. Bard, M. Stratmann, , 2003, p460, Wiley-VCH, Weinheim
- 3 K. Ogle, M. Wolpers, Phosphate Conversion Coatings in *ASM-Handbook* Vol. 13A: Principles of Metallic Corrosion, Corrosion Protection and Control in press.
- 4 W. Machu, *Werkstoffe und Korrosion*, 4 (1963) 273-279
- 5 M. Bastian, P. Kuhm, G. Meyer, *Metalloberfläche* 53 (1) (1999) 10-15, 53 (2) (1999) 10-14, 53 (3) (1999) 10-14
- 6 U. Honig, *Metalloberfläche* 43 (1989) 8, 361
- 7 G.W. Jernstedt, *Trans. Electrochem. Soc.* 83 (1943) 361
- 8 K. Wittel, *Industrie und Lacke*, 51 (1983) 5, 169-171
- 9 H. Gehmecker, *Metalloberfläche* 44 (1990) 10
- 10 W. Wimmer, J. Gottschlich, E. Busch, H. Gehmecker, *Metal Finishing* (1998) 16-19
- 11 T.S.N.S. Narayanan, *Product Finishing*, 50 (1997) 4, 18
- 12 E. Lutter, *Die Entfettung*, Eugen G. Leuze Verlag, 1990
- 13 K. Wittel, *Metalloberfläche* 42 (1988) 263-267
- 14 J. Riesop, W.-A. Roland, M. Pimminger, S. Kolnberger, *Galvatech-Proceedings* (1992), Amsterdam, 236-240
- 15 P.-E. Tegehall, N.-G. Vannerberg, *Corrosion Science* 32 (1991) 635-652
- 16 D. Meyer, W.-D. Schulz, J. Sommer, *Metalloberfläche* 49 (1995) 12, 920-925
- 17 P.-E. Tegehall, *Acta Chemica Scandinavica*, 43 (1989) 322-330
- 18 P.-E. Tegehall, *Colloids and Surfaces* 42 (1989) 155-164
- 19 P.-E. Tegehall, *Colloids and Surfaces* 49 (1990) 373
- 20 M. Wolpers, J. Angeli, *Applied Surface Science* 179 (2001) 281-291
- 21 S. Maeda, *Prog. Org. Coat.* 11 (1983) 1
- 22 I. Van Roy, H. Terryn, G. Goemine, *Colloids and Surfaces* 136 (1998) 89

- 23 G. Lagaly, Colloids in *Ullmann's Encyclopedia of Industrial Chemistry*, Vol. A7, VCH, Weinheim, New York, 1986
- 24 W. Machu, *Korrosion Metallschutz*, 17 (1941) 157
- 25 W. Machu, *Archiv für Metallkunde* 6 (1949) 203-208
- 26 J.O. Nriagu, *Geochimica et Cosmochimica Acta* 37 (1973) 2357
- 27 M. Binnewies, *Chemische Gleichgewichte. Grundlagen. Berechnungen. Tabellen*, Wiley-VCH, 1996
- 28 P.-E. Augustsson, I. Olefjord, I. Y. Olefjord, Y., *Werkstoffe und Korrosion* 34 (1983)
- 29 E. Klusmann, Zeit- und ortsauflösende Untersuchungen zur Phosphatierung, Dissertation (1998)
- 30 W.-A. Roland, K.-H. Gottwald, *Metalloberfläche* 48 (1994) 11, 790-796
- 31 T.S.N.S. Narayanan, *Corrosion Reviews* 12 (1994) 201-238
- 32 W. J. Van Ooij, *Surface and Interface Analysis* 9 (1986) 367-370
- 33 W. J. Van Ooij, T. H. Visser, *Spectrochimica Acta* 39 (1983) 12, 1541-1545
- 34 S. Maeda, M. Yamamoto, *Progress in Organic Coatings* 33 (1998) 83-89
- 35 A. Losch, E. Klusmann E., J. W. Schultze, *Electrochimica Acta* 39 (8) (1994) 1183-1187
- 36 R.J. Hill, J. B. Jones, *American Mineralogist* 61 (1976) 987-995
- 37 S.J. Kang, T.C. Ozawa, Balls and Sticks, Software from [www.toycrate.org](http://www.toycrate.org)
- 38 M. Friedrich, Dissertation, Universität Köln (1992)
- 39 Y. Arnaud, Y., E. Sahakian; M. Romand, *Applied Surface Science* 32 (1988) 281-294, ibid 296-308
- 40 N. Satoh, *Surface and Coatings Technology* 30 (1987) 171-181
- 41 W.-A. Roland, K.-H. Gottwald, *Metalloberfläche* 42 (1988) 6, 301-305
- 42 R.W. Miller, M. Petschel, R.G. Hart, *Metal Finishing* 7 (1994) 13-16
- 43 E. Klusmann, U. König, J.W. Schultze, *Materials and Corrosion* 46 (1995) 83-
- 44 J. P. Servais, B. Schmitz, V. Leroy, *Materials Performance* (1988) 56-61
- 45 W.J. Van Ooij, A. Sabata, *Journal of Coatings Technology* 61 (1989) 51-65
- 46 W.J. Van Ooij, A. Sabata, *Surface and Coatings Technology* 39/40 (1989) 667-674

- 47 C.R. Shastry, H.E. Townsend, *Corrosion Science* 45 (1989) 103-119
- 48 W.J. Van Ooij, A. Sabata, *Corrosion* 46 (2) (1990) 162-171
- 49 M.C. Bernard, A. Hugot-Le Goff, A., D. Massinon, D.; N. Phillips, *Corrosion Science* 35 (1993) 1339-1349
- 50 M. Stratmann H. Streckel, *Materials and Corrosion* 43 (1992) 316
- 51 M. Rohwerder, M. Stratmann, A. de Boeck, K. Ogle et al., Galvatech, 5<sup>th</sup> International Conference on zinc and zinc alloy coated steel sheet, 2001, Brussels, Proceedings, p585.
- 52 D. Thierry, F. Zou, *Galvatech Proceedings* (1998), 378
- 53 X.G. Zhang, *Corrosion and Electrochemistry of Zinc*, Plenum Press, New York, 1996
- 54 W. Fürbeth, M. Stratmann, *Corrosion Science* 43 (2001) 207-227, 229-41, 243-254
- 55 M. Stratmann, M. Wolpers, H. Streckel, R. Feser, *Ber. Bunsenges. Phys. Chem.* 95 (1991) 1366
- 56 A. Leng, H. Streckel, K. Hofmann, M. Stratmann, *Corrosion Science* 41 (1999) 547; *Ibid* 41 (1999) 579; *Ibid* 41 (1999) 599
- 57 J. V. Ritter, *J. Coat. Tech.* 54(1982)51.
- 58 J.J. Ritter, J. Kruger, *J. Surf. Sci.* 96(1980)364.
- 59 R. E. Armstrong, B. W. Johnson, J. D. Wright, *Electrochimica Acta* 36(1991)1915.
- 60 M.C. Bernard, A. Hugot-Le Goff, N. Phillips, *J. Electrochem. Soc.* 142 (7) (1995) 2162-2166, *ibid* 2167-2170
- 61 W.J. Van Ooij, A. Sabata, G. Strom, *Progress in Organic Coatings* 18 (1990) 147-172
- 62 B. Schrader, *Infrared and Raman Spectroscopy General Reference*
- 63 N.B. Colthup, L.H. Daly, S.E. Wiberley, "Introduction to Infrared and Raman spectroscopy", Academic Press, San Diego (1990)
- 64 W. Schrof, J. Klingler, W. Heckmann, D. Horn, *Colloid & Polymer Science* 276 (1998) 577-588
- 65 A.F. Holleman, E. Wiberg, "Lehrbuch der anorganischen Chemie" 101. Auflage, Walter de Gruyter, Berlin (1995)
- 66 D.A. Buttry, "The Quartz Crystal Microbalance as an in situ tool in electrochemistry" in *Electrochemical Interface*, Ed. H.D. Abruna, 2000, p529, Verlag

- 67 **M.R. Deakin**, D.A. **Buttry**, *Anal. Chem.* 61 (1989) 1147A
- 68 G. Sauerbrey, *Zeitschrift für Physik* 155 (1959) 206
- 69 K.K. Kanazawa, J.G. Gordon, *Anal. Chim.* 57 (1985) 170
- 70 R. Schumacher, *Angewandte Chemie*, 102 (1990)4, 347-360
- 71 R. Schumacher, G. Borges, K. Kanazawa, *Surface Science* 163 (1985) L621
- 72 R.K. Singh Raman, B. Gleeson, D.J. Young, *Materials Science and Technology* 14 (1998) 373.
- 73 A. Sommer, Leidheiser, *Microbeam Analysis* (1984) 111
- 74 N. Sato, K. Watanabe, T. Minami, *J. Materials Science* 26 (1991) 1383
- 75 A.J. Sommer, H. Leidheiser, *Corrosion* 43 (1987) 661
- 76 K. Ogle, S. Weber, *J. Electrochem. Soc.*, 147 (2000)1770
- 77 P. Schmutz, D. Landolt, *Electrochimica Acta* 45 (1999) 899-911
- 78 M. Seo, M., K. Ysohida, K., K. Noda, *Materials Science and Engineering* 198 (1995) 197-203
- 79 J. Telegdi, A. **Shaban**, E. Kaiman, *Electrochimica Acta* 45 (2000) 3639-3647
- 80 K. Ogle, C. Gabrielli, H. Perrot, M. **Keddam**, *J. Electrochem. Soc.*, 141(1994)2655.
- 81 K. H. Stellnberger, M. **Wolpers**, T. Fili, C. **Reinartz**, T. Paul, M. Stratmann *Faraday Discuss.* 107 (1997)307
- 82 D. **Hamm**, K. Ogle, C.O.A. Olsson, S. Weber, D. Landolt, *Corrosion Science* 44(2002)1443.
- 83 K. Ogle, S. Weber, Conference Abstract, Electrochemical Society Meeting, San Diego 1998
- 84 **N.J. Everall**, *Applied Spectroscopy* 54 (2000) 773
- 85 P. Lodi, K. Ogle, A. Storhaye, Pat. 92-03782, France (1992)
- 86 D.A. Skoog, J.J. **Leary**, "Instrumentelle Analytik", Springer Berlin-Heidelberg (1996)
- 87 A. J. Bard, L. **Falkner**, "Electrochemical Methods", Appendix C, 1980 John Wiley and sons
- 88 W. Maddams, *Applied Spectroscopy* 34 (1980) 245
- 89 D. Gosztola, **M.J. Weaver**, *J. Electroanal. Chem.* 271 (1989) 141



90 M.-C. Bernard, A. Hugot-Le Goff, N. Toan, *SPIE* Vol. 2531 117

91 C. Melendres, New Techniques for Characterizing Corrosion and Stress Corrosion, Symposium Proceedings, Cleveland (1996)

92 R. Kostecki, F. McLarnon, *J. Electrochem. Soc.* 144 (2) (1997)485

93 J. Desilvestro, D.A. Corrigan, M.J. Weaver, *J. Phys. Chem* 90 (1986) 6408

## DANKSAGUNG

Die Arbeit wurde in der voestalpine AG Division Stahl in **Linz** im Zeitraum von Oktober 2000 bis Oktober 2002 in Zusammenarbeit mit der Technischen Universität Wien, Institut für Chemische Technologien und Analytik, Abteilung Elektrochemie durchgeführt.

Univ. Prof. Dr. Christoph Fabjan danke ich für die bereitwillige Betreuung und die hilfreichen Diskussionen während meiner Doktorarbeit.

Für die Betreuung im Unternehmen danke ich besonders Herrn Dr. Michael **Wolpers**, der mich auch noch nach seinem Wechsel zur Henkel KGaA in vielen Fragen, Anregungen und interessanten Diskussionen begleitete.

Den Mitarbeitern der Abteilung Organische Beschichtung, namentlich Dr. Karl-Heinz Stellnberger und Dr. Franz Androsch möchte ich für ihr Interesse und ihre Mithilfe während meiner Arbeit danken.

Meinen Doktorandenkollegen **Dipl.-Ing.** Martin Fleischanderl und **Dipl.-Ing.** Peter Konrath sei für Rat und Tat während der gesamten Arbeit gedankt.

Den Mitarbeitern der Abteilung Oberflächenanalytik, besonders Dipl.-Ing. Reinhold Aichinger und Josef Schickermüller möchte ich für die Unterstützung bei der **Raman-Spektroskopie** danken.

Meinem langjährigen Freund Dipl.-Ing. Martin Rosner danke ich besonders für die Hilfe bei der Literatursuche.

Dr. Kevin Ogle, Dr. **Norma Falcy** und Nadia Meddahi danke ich für die freundliche Aufnahme und Betreuung während meines Aufenthaltes in Frankreich.

Nicht zuletzt möchte ich meiner Lebensgefährtin Roswitha für die Geduld und die moralische Unterstützung vor allem während des **Verfassens** der Arbeit und meinen Eltern danken, deren Vertrauen und finanzielle Unterstützung meine Ausbildung erst ermöglichte.

## LEBENS LAUF

Name: Alexander Tomandl  
Geburtsdatum: 4. Mai 1973  
Geburtsort: Steyr/ OÖ  
Familienstand: ledig

### Schul Ausbildung:

1983-1991: Humanistisches Gymnasium Stift Seitenstetten

### Studium:

1991-1998: Studium der Technischen Chemie an der Technischen  
Universität Wien

07/1997-02/1998: Diplomarbeit; durchgeführt in der Voestalpine AG, Linz  
Thema: „Elektrochemische Untersuchungen zum Korrosions- und  
Passivierungsverhalten von Stählen im neutralen und alkalischen  
Milieu“

03/1998: 2. Diplomprüfung

seit 10/2000: Doktoratsstudium

Dissertation: „Electrochemical and spectroscopic in situ techniques for  
the investigation of the phosphating of zinc coated steel“  
(Durchführung in der Voestalpine AG, Linz)

### Wehrdienst:

07/1998-03/1999: Wehrdienst bei der 2. Betriebsversorgungsstelle NÖ/Zwölfaxing

### Berufliche Tätigkeiten:

03/1998-06/1998: Tätigkeit als freier Mitarbeiter

03/1999-12/1999: in der Voestalpine AG, Linz

01/2000-09/2000: Tätigkeit bei Fa. Neusiedler/Hausmening als  
technischer Produktmanager